

Banner appropriate to article type will appear here in typeset article

Modelling and analysis of an endothermic reacting counter-current flow

Ellen K. Luckins¹†, James M. Oliver¹, Colin P. Please¹, Benjamin M. Sloman², and Robert A. Van Gorder³

¹Mathematical Institute, University of Oxford, Andrew Wiles Building, Radcliffe Observatory Quarter, Woodstock Road, Oxford OX2 6GG, UK

²Elkem ASA, Technology, Fiskaaveien 100, Kristiansand 4621, Norway,

³Department of Mathematics and Statistics, University of Otago, P.O. Box 56, Dunedin 9054, New Zealand

(Received xx; revised xx; accepted xx)

We study the endothermic reaction and flow of a granular solid reactant, where energy for the reaction is provided by a counter-current flow of hot gases through the porous reactant bed. Research into reacting flows typically focusses on exothermic combustion processes. However, endothermic processes are common in the metallurgy industry, including the production of cement, silicon, and rutile titanium dioxide. Several common features are observed in experimental and numerical studies of these processes, including critical temperatures of the reactant at which the chemical reaction begins, and regions of the reactor with uniform reactant temperature. Motivated specifically by the processes in a silicon furnace, we analyse a model of endothermic, reacting counter-current flow using the method of matched asymptotic expansions. Assuming the Péclet number in the solid is large, we explore the full range of values for the dimensionless inter-phase heat-transfer rate, finding six distinguished limits. In all limits, we find a diffusive boundary layer in which there is a fast chemical reaction rate due to the high temperatures, analogous to exothermic flame fronts. Outside this region, the counter-current flow is crucial to the chemical processes. For intermediate values of the heat-transfer rate, we find the same qualitative properties as those observed across the metallurgy industry, and we quantify the dependence of these properties on the flow rate and heat-transfer rate. In the limit of large heat-transfer coefficient, we derive the single-temperature limit, in which the solution structure is dependent on the direction of net heat flux through the domain.

Key words: Authors should not enter keywords on the manuscript

1. Introduction

Counter-current flows are systems in which two materials flow in opposite directions, meanwhile exchanging either heat or mass. Mass-exchanging counter-current flows are found in biological systems such as the production of urine in the kidneys (Winters & Davies 1961),

† Email address for correspondence: luckins@maths.ox.ac.uk

occur in oil extraction (Abd *et al.* 2019), and are ubiquitous in chromatography and the separation of chemicals (Brunner 2009; Ignatova *et al.* 2011; Skalicka-Woźniak & Garrard 2014; Sutherland 2007). Heat-exchanging counter-current flows are also found in biology, including blood flow through the body (Mitchell & Myers 1968) and in the respiratory system (Schmidt-Nielsen *et al.* 1970), and are used for efficient coolant systems, for instance in the nuclear industry (Deendarlianto *et al.* 2012).

We are interested in systems of heat-exchanging, counter-current flow, in which the heat transferred between the phases is necessary for an endothermic chemical reaction in the cooler phase, with temperature dependent reaction rate. A classical counter-current heat-exchange system, modelling blood flow in the veins and arteries, is studied by Mitchell & Myers (1968), with the decay or growth of the temperatures in the two opposing flows found analytically as functions of distance. The key parameters are shown to be i) the ratio of the heat transfer rate between the veins and arteries to the flow rate of the blood, and ii) the ratio of the heat transfer rate with the external environment to the flow rate of the blood. Similar counter-current models are studied by Fitt *et al.* (1985), Hagan & Ockendon (1991), and Nunge & Gill (1965), although unlike Mitchell & Myers (1968), these take into account the diffusion processes at the interface between the fluids, rather than prescribing a bulk heat transfer coefficient. These studies highlight one particular difficulty of analysing counter-current flows: since the models are forward/backward (or two-way) diffusion equations (Beals 1981), care must be taken to ensure well-posedness. Eigenfunction methods on the half-range of the domain have been developed (Hagan & Ockendon 1991), and used to explore the efficiency of the counter-current system.

Although it is possible to find examples of reactive flows which are also counter-current flows, the literature in general neglects counter-current flows in the presence of chemical reactions. The interaction of fluid flow and heat transfer with chemical reactions is often studied in relation to combustion and flames (Tieszen 2001). For non-pre-mixed combustion, a diffusive flame front is found at the interface between the two gaseous reactants (Bilger 1989). The effect of mixing at the flame front has been analysed in detail both for laminar (Sirignano 2021) and turbulent (Bilger 1989) mixing layers. Flame fronts are also analysed in an applied counterflow (Ravikrishna & Sahu 2018), which allows for steady-state flame structures. Single-temperature combustion models are studied by Merzhanov & Khaikin (1988), with the domain divided into reaction zones, and travelling flame fronts are found. Single-temperature models of counterflow filtration combustion are studied by Booty & Matkowsky (1991), Chapiro & de Souza (2016), Chapiro & Senos (2018), and Schult *et al.* (1998). The existence and uniqueness of solutions to such systems is shown by Chapiro & Senos (2018), while Booty & Matkowsky (1991), Chapiro & de Souza (2016), and Schult *et al.* (1998) find travelling wave solutions asymptotically. Schult *et al.* (1998) further characterise several types of instabilities of the travelling wave solutions to the single-temperature model. In situations where not all chemicals are at the same temperature, the inter-phase heat transfer must be taken into account. For instance, the combustion of porous solids is also studied using two-temperature models, with applications to catalytic converters and filtration combustion (Byrne & Norbury 1994, 1997; Norbury & Stuart 1988), smouldering cigarettes (Egerton *et al.* 1963), and the combustion of rocket fuels (Koopmans *et al.* 2013). Similarly to the single-temperature case, the reaction is found to take place in a hot reaction zone, which is shown to move as a travelling-wave flame front through the domain (Byrne & Norbury 1997; Norbury & Stuart 1988). The motion of flame fronts is studied by Please *et al.* (2003) for a system with a two-stage chemical reaction, the second of which may be endothermic. Under certain conditions on this endothermic reaction, travelling combustion waves with a similar structure to purely-exothermic flame fronts are still found.

By contrast, in many metallurgical applications the chemical reactions of interest are

endothermic, and heat-exchanging counter-current flows are used to provide energy for endothermic chemical reactions. For instance, the production of rutile titanium dioxide in a rotary kiln (Agrawal & Ghoshdastidar 2017), the pyrolysis of aluminium (Marias *et al.* 2005), the production of cement (Spang III 1972), and the production of silicon in a submerged arc furnace (Schei *et al.* 1998) all involve endothermic chemical processes in which heat required for the reaction is provided by a counter-current flow. In these endothermic processes, heat is removed from the system by the reactions. Furthermore, the endothermic reactions have temperature-dependent reaction rates, meaning that the heat lost from the system depends on the local temperature, further affecting the counter-current heat transfer. These effects fundamentally change the behaviour from the classical counter-current exchange studied by Mitchell & Myers (1968). For instance, it is observed by Agrawal & Ghoshdastidar (2017) that once the reactant reaches a critical temperature in the rotary kiln, the energy transferred to it by the counter-current flow is used for the chemical reaction, and the reactant remains at or close to this critical temperature. Similar behaviour is seen in cement production (Mujumdar & Ranade 2006; Spang III 1972; Stadler *et al.* 2011), with distinct regions of the domain in which different chemical and heat transfer processes are seen to dominate, and there are critical temperatures at which certain reactions become important. Many reacting counter-current flow systems may also be viewed as free boundary problems, as there is often a finite region within which the reaction takes place, and this region moves both as material is fed in and reacted away. It is of practical importance to understand the required length of the reactor such that the reaction is completed by the end of the reactor, as the process will fail if the material is fed in too fast, for the necessary reactions to take place within the lengthscale of the reactor. For instance, when designing a kiln for the production of rutile titanium dioxide, the “kiln length” must be determined so that the chemical reactions have completed by the time the reactant material reaches the end of the kiln (Agrawal & Ghoshdastidar 2017), else the process will fail. There is a similar free boundary at the edge of the reacting material bed within a silicon furnace, where the material collapses or drips into the craters which form beneath the electrodes in the furnace (Andresen 1995; Sloman *et al.* 2020).

Research into these endothermic, reacting, counter-current flows in the literature is limited to numerical simulations of specific models for specific applications (Agrawal & Ghoshdastidar 2017; Mujumdar & Ranade 2006; Spang III 1972; Stadler *et al.* 2011). We have highlighted above similar features of these flows that are observed across the different applications, specifically the distinct regions of the reactor in which the reaction occurs or not, the free-boundary nature of these problems, and the regions in which the reactant remains at a uniform, critical temperature while the endothermic reaction is taking place. It is not clear from these numerical studies, however, how the sizes of these distinct regions, the value of the critical temperatures, or the position of the free boundaries depend on the flow rates, the heat transfer rate between the phases, and the chemical reaction rates.

In this paper, we formulate a mathematical model for a generic endothermic, reacting, counter-current flow moving in one dimension, and then carry out a detailed asymptotic analysis to detect all distinguished limits as well as the size of all important lengthscales for each limit. Specifically, we consider the flow of a hot gas through a granular porous structure which is flowing slowly in the opposite direction. As the solid material is heated, it reacts to form the gas. The reaction is endothermic, with a temperature-dependent reaction rate. One direct application motivating our model is the production of silicon within a submerged arc furnace. In this application there are two sources of heat for the chemical reactions: the hot gases flowing through the material bed, and the heat radiation onto the free surface at the edge of the material bed. An asymptotic analysis of the endothermic reactions within a silicon furnace is provided by Sloman *et al.* (2018), but under the restrictive assumption

that all chemical species have the same temperature locally, which precludes many of the counter-current flow effects.

Using the method of matched asymptotic expansions, we explore several distinguished limits corresponding to different heat transfer rates between the two phases, spanning the whole range of this parameter. In many of these distinguished limits we find the same features observed in the other endothermic metallurgical systems, including the critical temperatures at which the reaction begins, and regions of uniform solid temperature. We show that these features arise at small or intermediate heat transfer rates. We additionally characterise how these features depend on the flow rates, heat transfer rates, and the temperature-dependence of the chemical reaction rate. By studying distinguished limits for large heat transfer rates, we can also understand those parameter regimes for which our model reduces to a single-temperature model, providing a region of validity for single-temperature models such as that of Sloman *et al.* (2018). The endothermic nature of the chemical reactions makes this system quite different to exothermic combustion processes, but there are also some similarities. Specifically, we find that the majority of the chemical reaction occurs within a hot reaction zone, analogous to the flame front in combustion processes, where the reaction rate is greatest. However, since the reaction is endothermic, this region is not self-sustaining, and is instead reliant on radiation at the boundary which provides heat that diffuses through the reaction zone. In this way, radiation at the boundary is rate limiting for the endothermic reaction.

The remainder of the paper is structured as follows. In Section 2 we present our model for the coupled counter-current flow, heat transfer, and endothermic chemical reaction system. In Section 3 we give an overview of the asymptotic analysis, which is given in detail in Sections 4–9. We study asymptotic structures in a one-dimensional geometry, in the limit of large Péclet number in the solid material. In Sections 4–9, we identify the various distinguished limits for different sizes of the dimensionless convective heat transfer coefficient (relative to the inverse Péclet number), ranging from it being negligible in Section 4 to large in Section 9. Numerical solutions of the reduced models are computed in Section 10, and our composite asymptotic solutions are compared with numerical solutions of the full model in Section 11. In Section 12, we discuss our results and provide concluding remarks.

2. Model development

We model the counter-current process within the material bed of a silicon furnace using the framework of multiphase flow (see, for example, Brennen 2005). Our model is similar to that used by Luckins *et al.* (2021), although we now include the heat transfer between the phases which is important on the longer domain lengthscale now considered.

As well as the silicon furnace, many of the other metallurgical applications of interest consist of essentially one-dimensional flows, and we will restrict to a one-dimensional geometry in this paper. Specifically, we consider the one-dimensional domain $x \in [s(t), x_0]$, where x_0 is prescribed and $s(t) \in (0, x_0)$ is a free boundary, as illustrated in figure 1. We consider a two-phase flow within this domain, consisting of a granular solid material s saturated with a connected gas phase g . We assume that solid material flows into the domain through the boundary $x = x_0$, and has velocity $\mathbf{u}_s = -u_s \mathbf{e}_x$. The gas phase flows in the opposite (positive- x) direction, with velocity $u_g \mathbf{e}_x$.

The solid material reacts to form the gas at rate \tilde{Q} so that the conservation of mass of each phase is given by

$$\frac{\partial \rho_g}{\partial t} + \frac{\partial}{\partial x}(\rho_g u_g) = \tilde{Q}, \quad \frac{\partial \rho_s}{\partial t} + \frac{\partial}{\partial x}(-\rho_s u_s) = -\tilde{Q}, \quad (2.1)$$

where ρ_N is the overall density within the mixture of phase $N = g, s$.

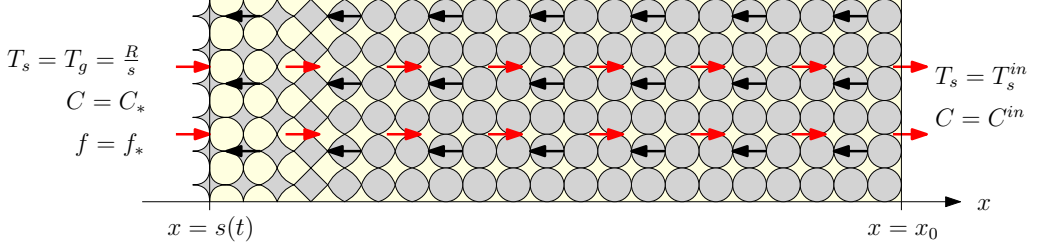


Figure 1: Schematic of the dimensional model domain $x \in [s, x_0]$, with granular solid (grey) moving right-to-left as shown by the black arrows, surrounded by gas (pale yellow) flowing left-to-right as shown by the red arrows. The solid particles become smaller nearer to the free boundary $x = s(t)$, as solid mass is reacted away. The boundary conditions are shown at $x = s(t)$ and $x = x_0$.

We assume that the reaction rate \tilde{Q} is an increasing function of the solid reactant temperature, T_s , as well as of the local density of solid material. We model this via an Arrhenius law of the form

$$\tilde{Q} = k_Q \rho_s \exp\left(-\frac{a_Q}{T_s}\right), \quad (2.2)$$

where $k_Q [\text{s}^{-1}]$ is the rate constant and $a_Q [\text{K}]$ encodes the activation energy of the reaction. We do not assume a high-activation limit as is commonly done in the literature (Buckmaster & Ludford 1983), but instead retain the form (2.2) in general.

As well as having temperature-dependent reaction rate, the chemical reaction is assumed to be endothermic. Since it is the solid phase which is reacting, and since it is expected to have the higher thermal conductivity of the two phases, we assume that the heat energy $\Delta H \tilde{Q}$ for the reaction is taken entirely from the solid phase. The equations of conservation of energy for both the gas and the solid phases are

$$\frac{\partial}{\partial t} (\rho_g c_{p,g} T_g) + \frac{\partial}{\partial x} (\rho_g c_{p,g} T_g u_g) = -\lambda (T_g - T_s) + m, \quad (2.3a)$$

$$\frac{\partial}{\partial t} (\rho_s c_{p,s} T_s) + \frac{\partial}{\partial x} (-\rho_s c_{p,s} T_s u_s) = \frac{\partial}{\partial x} \left(k_s \frac{\partial T_s}{\partial x} \right) - \Delta H \tilde{Q} + \lambda (T_g - T_s) - m, \quad (2.3b)$$

where T_N is the temperature of phase N , and we assume for simplicity that the specific heat capacities $c_{p,N}$ of both the gas and solid phases are constant. Here, m is the net heat gained by phase g from phase s due to the transfer of mass (by chemical reactions) between the two phases. We neglect heat diffusion in the gas phase, which is expected to be negligible in comparison with the advection of heat in this phase, but assume the granular solid material has constant, non-zero effective thermal conductivity k_s . We note that in the silicon furnace, some of this solid material is quartz rock. This quartz rock softens at high temperatures, becoming a very high viscosity liquid (Luckins *et al.* 2021; Schei *et al.* 1998). As such, the contact points between the solid particles will actually have non-negligible surface area and so it is reasonable to expect heat conduction through the solid structure. The convective heat transfer between the phases is modelled to be linear in the temperature difference between the phases, with coefficient $\lambda [\text{W m}^{-3} \text{K}^{-1}]$. For two phase flow, the convective heat transfer coefficient λ generally depends on the porosity, the porous structure, the relative velocity of the phases, and the associated Reynolds number and Prandtl number of the flow (Brennen 2005; Kaviany 2012). Estimates for λ vary for different flow regimes and porous structures. The net heat transfer, m , due to the inter-phase transfer of mass depends on the temperature of both phases, the chemical reaction rate, and the stoichiometry of the reaction — a discussion

of these processes is given by Ni & Beckermann (1991), where m is shown to depend on the interfacial temperature (at the interface between the two phases on the microscale). For simplicity, we assume that the heat content $c_{p,s}T_s$ of phase s is carried with the material as it changes phase due to the chemical reaction, with rate equal to the rate of the reaction \tilde{Q} . This results in the form $m = c_{p,s}T_s\tilde{Q}$ which is also used by Baer & Nunziato (1986).

To close the model, we in general require the phase velocities u_s and u_g . In one dimension, the solid velocity may be fixed simply by a compaction law or a description of the compressibility of the solid matrix, without needing to study conservation of momentum directly. For simplicity, we assume that the solid matrix is incompressible. The resulting uni-directional solid velocity u_s is thus constant. Since the density of the gas is so much less than the density of the solid, the velocity of the gas produced by the reaction must be many orders of magnitude larger than the solid velocity. Thus the gas phase may be assumed to be quasi-steady on the slow timescale of variation in the solid phase (see Luckins *et al.* (2021) for a detailed dimensional analysis). In our one-dimensional geometry, the quasi-steady gas flow is fully described by the mass flux

$$f = \frac{\rho_g u_g}{M_g}, \quad (2.4)$$

and we need not deal directly with the gas velocity. We also change variables in order to consider the problem in terms of the solid concentration

$$C = \frac{\rho_s}{M_s}, \quad (2.5)$$

rather than the density. Since the solid is reacting to form the gas, in a reaction which we assume has stoichiometry 1, we note that the molar masses $M := M_s = M_g$ are equal.

The equations (2.1) and (2.3) thus become a system for C , f , T_s , and T_g , in $x \in [s(t), x_0]$, namely

$$\frac{\partial C}{\partial t} - u_s \frac{\partial C}{\partial x} = -Q, \quad (2.6a)$$

$$\frac{\partial f}{\partial x} = Q, \quad (2.6b)$$

$$M c_{p,s} C \left(\frac{\partial T_s}{\partial t} - u_s \frac{\partial T_s}{\partial x} \right) = k_s \frac{\partial^2 T_s}{\partial x^2} + \lambda (T_g - T_s) - \Delta H M Q, \quad (2.6c)$$

$$M c_{p,g} \frac{\partial}{\partial x} (f T_g) = M c_{p,s} T_s Q - \lambda (T_g - T_s), \quad (2.6d)$$

where the term m in the solid heat equation has been absorbed into the advection term on the left, using the equation of conservation of mass in the solid material. Here we use the notation

$$Q = k_Q C \exp \left(-\frac{a_Q}{T_s} \right), \quad (2.7)$$

for the chemical reaction rate in terms of the solid concentration.

2.1. Boundary and initial conditions

The equations of conservation of mass in the solid and gas phases (2.6a)–(2.6b) are both hyperbolic. We impose the inflowing concentration of solid at $x = x_0$, and a flux of gas f_* through the free boundary, so that

$$C = C^{\text{in}} \quad \text{at } x = x_0, \quad f = f_* \quad \text{at } x = s(t). \quad (2.8a)$$

251 We prescribe a cold temperature of the inflowing solid material

$$252 \quad T_s = T_s^{\text{in}} \quad \text{at } x = x_0. \quad (2.8b)$$

253 At the free boundary, we impose

$$254 \quad T_g = T_s = \frac{R}{s} \quad \text{at } x = s(t), \quad (2.8c)$$

255 which is a crude model for a point radiative heat source at $x = 0$, with constant intensity
 256 R , incident on this boundary. This boundary condition is motivated by the electric arc
 257 which forms in the (roughly cylindrical) crater region within the material bed of a silicon
 258 submerged arc furnace (Schei *et al.* 1998). For other applications, different forms for the
 259 boundary condition (2.8c) may be more appropriate.

260 The position of the free boundary $x = s(t)$ is determined by the Stefan-like condition on
 261 the concentration of solid material

$$262 \quad C = C_* \quad \text{at } x = s(t), \quad (2.8d)$$

263 where $C_* < C^{\text{in}}$. Thus the free boundary of the domain is the position where sufficient solid
 264 material has been reacted away. For silicon furnaces, this condition describes the position
 265 of the edge of the gas-filled crater that forms deep within the furnace: C_* is the critical
 266 concentration at which the solid structure loses structural integrity, and any remaining solid
 267 material collapses into the crater.

268 Finally, we require an initial configuration for the system as initial conditions on C , f , T_s ,
 269 T_g , and the position s of the free boundary. These initial conditions must be consistent with
 270 the boundary conditions described above.

271 2.2. Nondimensionalisation

272 We nondimensionalise the model (2.6) and (2.8) by scaling $x = x_0 x'$, $s = x_0 s'$, $t = x_0 t' / u_s$,
 273 $C = C^{\text{in}} C'$, $f = [f] f'$, $T_s = [T_s] T'_s$, and $T_g = [T_g] T'_g$, where the prime notation denotes
 274 dimensionless variables. The temperature scalings are given by the boundary condition at
 275 $x = s(t)$, since this is the major source of heat to the system, and so we fix $[T_s] = [T_g] =$
 276 $R/[s]$, where $[s]$, to be determined, is the expected size of s . We define δ to be the inverse
 277 Péclet number

$$278 \quad \delta = Pe^{-1} = \frac{k_s}{x_0 u_s M c_{p,s} C^{\text{in}}}. \quad (2.9)$$

279 Throughout this paper we assume that δ is small, so that the effective thermal conductivity of
 280 the porous solid structure is small over the relatively large lengthscale of the domain. Thus
 281 the heat provided to the solid material at the boundary $x = s(t)$ cannot penetrate far into the
 282 domain: we anticipate a conductive boundary layer at this boundary, of width $O(\delta)$.

283 Assuming that the majority of the chemical reaction occurs in this hot $O(\delta)$ boundary
 284 layer at $x = s(t)$, the lengthscale $[s]$ is given by a balance in the solid mass equation (2.6a),

$$285 \quad \frac{u_s}{\delta x_0} = k_Q \exp\left(\frac{-a_Q [s]}{R}\right), \quad (2.10)$$

286 which, along with the definition of δ , gives $[s] = (R/a_Q) \log(k_Q k_s / (M c_{p,s} u_s^2 C^{\text{in}}))$. The
 287 temperature scalings are therefore $[T_s] = [T_g] = a_Q / \log(k_Q k_s / (M c_{p,s} u_s^2 C^{\text{in}}))$. We note
 288 that for these temperature scalings to be positive, the velocity u_s of the solid material must

289 be sufficiently small. Specifically, we require

$$290 \quad u_s < \sqrt{\frac{k_Q k_s}{M c_{p,s} C^{\text{in}}}}. \quad (2.11)$$

291 For larger u_s than this, the (bounded) Arrhenius chemical reaction rate cannot match the rate
 292 at which material flows in, and the model ceases to be valid. Finally, balancing the gas mass
 293 equation (2.6b) requires $[f] = u_s C^{\text{in}}$.

294 With these scalings, and dropping the prime notation, the equations become

$$295 \quad \delta \left(\frac{\partial C}{\partial t} - \frac{\partial C}{\partial x} \right) = -Q, \quad (2.12a)$$

$$296 \quad \delta \frac{\partial f}{\partial x} = Q, \quad (2.12b)$$

$$297 \quad C \left(\frac{\partial T_s}{\partial t} - \frac{\partial T_s}{\partial x} \right) = \delta \frac{\partial^2 T_s}{\partial x^2} + \mu (T_g - T_s) - \frac{\gamma}{\delta} Q, \quad (2.12c)$$

$$298 \quad K \frac{\partial}{\partial x} (f T_g) = \frac{1}{\delta} T_s Q - \mu (T_g - T_s), \quad (2.12d)$$

300 on the domain $x \in (s(t), 1)$, where the dimensionless chemical reaction rate is

$$301 \quad Q(C, T_s) = C \exp \left(A \left(1 - \frac{1}{T_s} \right) \right), \quad (2.12e)$$

302 and with boundary conditions

$$303 \quad C = C_*, \quad f = f_*, \quad T_s = T_g = \frac{\rho}{s} \quad \text{at } x = s(t), \quad (2.12f)$$

$$304 \quad C = 1, \quad T_s = T^{\text{in}} \quad \text{at } x = 1, \quad (2.12g)$$

306 with f_* , C_* and T^{in} appropriately rescaled.

307 Here we have introduced the dimensionless parameters

$$308 \quad A = \frac{a_Q [s]}{R}, \quad \mu = \frac{\lambda x_0}{u_s M c_{p,s} C^{\text{in}}}, \quad K = \frac{c_{p,g}}{c_{p,s}}, \quad \gamma = \frac{[s] \Delta H}{M c_{p,s} R}, \quad \rho = \frac{[s]}{x_0}. \quad (2.13)$$

309 In addition to (2.12), we require initial conditions for C , f , T_g , T_s and s . The system (2.12) is
 310 a 5th order differential system of equations in space, with an additional degree of freedom in
 311 the position s of the free boundary. We therefore expect the model to be correctly specified
 312 since we impose six boundary conditions.

313 Throughout, we assume that the dimensionless parameters K , γ , A , ρ , C_* , and f_* in the
 314 model (2.12) are of order unity (see Luckins *et al.* (2021) for justification in the case of a
 315 silicon furnace). The inverse Péclet number, δ , is expected to be on the order of $10^{-3} - 10^{-2}$
 316 (Luckins *et al.* 2021), and is the smallest parameter in the system. The asymptotic analysis
 317 in this paper is in the limit of $\delta \rightarrow 0$. We also assume that the input temperature of the solid,
 318 T^{in} , is small. Specifically, we require

$$319 \quad \delta T^{\text{in}} \gg \exp \left(A \left(1 - \frac{1}{T^{\text{in}}} \right) \right), \quad (2.14)$$

320 so that the rate of reaction at this temperature is much less than the rate at which material
 321 moves through the whole domain by advection. Thus if there were no heating, we would
 322 expect the solid material not to appreciably react away over the time it spends moving through
 323 the domain. We further assume that $\delta \ll T^{\text{in}}$, meaning that although T^{in} is small in the sense

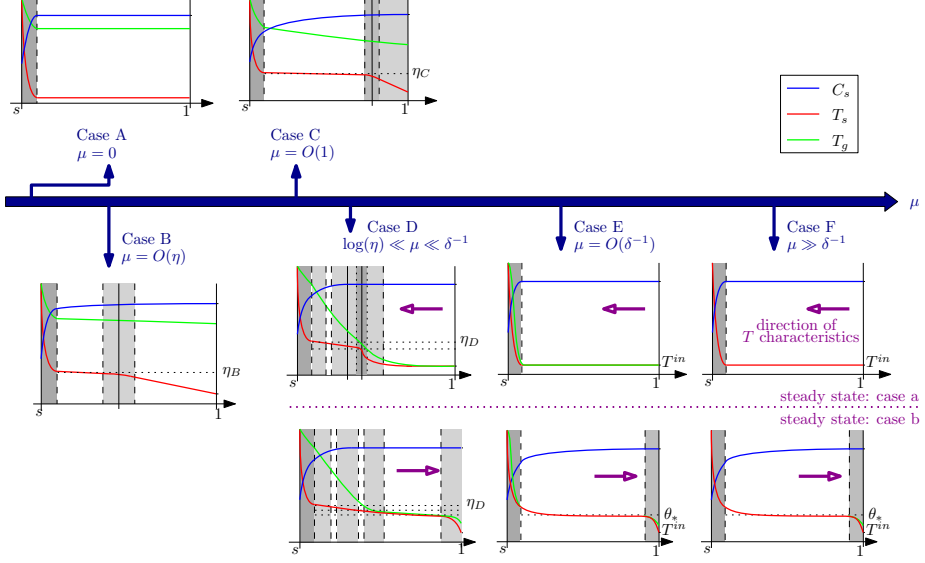


Figure 2: Schematics of the different asymptotic solution structures (in steady state for cases D–F) for increasing μ . In each case, the solutions, T_s red, T_g green, and C blue are illustrated in the domain $x \in [s(t), 1]$, with boundary layers and transition layers shown by the grey regions.

of (2.14), it is not as small as δ . This further assumption that $\delta \ll T^{\text{in}}$ does not impact the dominant behaviour of the system, and is only needed when analysing the correction terms to the leading order behaviour in certain parameter regimes. The final dimensionless parameter is μ , which encodes the rate of convective heat transfer between the phases. We will explore various distinguished limits relating μ to δ .

3. Overview of asymptotic analysis

In Sections 4–9, we will consider a range of different distinguished limits corresponding to different values of the convective heat transfer coefficient μ , in terms of functions of δ . We refer to these distinguished limits as cases A–F, studied in Sections 4–9, respectively, in order of increasing μ , with case A being the small- μ limit, $\mu \rightarrow 0$, (which we show is valid for $\mu \ll 1/\log(1/\delta)$), and case F the large- μ limit (corresponding to $\mu \gg \delta^{-1}$). A schematic of the solution structures in each of the cases A–F is shown in figure 2. Detailed schematics are given for each case in Sections 4–9.

The asymptotic results that we present in this paper are mostly determined by the various dominant balances in the equation of conservation of energy in the solid, (2.12c). We label the terms in this equation as follows

$$\underbrace{C \left(\frac{\partial T_s}{\partial t} - \frac{\partial T_s}{\partial x} \right)}_1 = \underbrace{\delta \frac{\partial^2 T_s}{\partial x^2}}_2 + \underbrace{\mu (T_g - T_s)}_3 - \underbrace{\frac{\gamma}{\delta} C \exp \left(A \left(1 - \frac{1}{T_s} \right) \right)}_4, \quad (3.1)$$

for explicit reference in our analysis. Terms 1 and 2 describe the advection and conduction, respectively, of heat within the solid material. Terms 3 and 4 describe the heat transferred to the solid by the gas, and are labelled separately since T_s and T_g may have different sizes in

different regions of the domain. Term 5 is the heat absorbed by the endothermic chemical reaction.

Since $\delta \ll 1$, heat conduction in the solid material (term 2 in (3.1)), has negligible effect through most of the domain. However, for all sizes of the convective heat transfer coefficient μ , we will find a boundary layer of width $O(\delta)$ at $x = s(t)$, in which heat conduction (term 2) is important. It is only in this thin layer that the heating of the solid material from the radiation incident onto the boundary as in (2.12f) is felt. This boundary layer is the region of largest T_s in the domain: in all other regions we will find $T_s \ll 1$. Since the chemical reaction rate is temperature-dependent, the most intense material consumption also therefore occurs in this $O(\delta)$ boundary layer at $x = s(t)$. Region I is therefore interpreted as the fast reaction region, with the heat of reaction provided by the radiation at the boundary. In all cases A–F, the reduced model in this boundary layer determines the position $s(t)$ of the free boundary. For some moderate values of μ the behaviour in the outer regions is coupled to the boundary-layer problem at leading order, and so also affects the position s .

Outside of this boundary layer there can be several types of behaviour depending on the size of the convective heat transfer coefficient μ . For small μ (case A), very little happens outside the boundary layer, with the solid temperature simply equal to its input value $T_s = T^{\text{in}}$ at leading order. For moderate μ (cases B–D), there is a balance between the transfer of heat from the gas to the solid (term 3 in (3.1)), and the energy consumed by the chemical reaction (term 5). In these cases, this balance determines the natural solid temperature scaling

$$\eta := \frac{A}{\log\left(\frac{1}{\delta\mu}\right)}, \quad (3.2)$$

and we find that $T_s \approx \eta$ is uniform throughout such regions of the domain. Since η depends on μ , for the different sizes of μ in cases B–D the value of η is different. The ratio η/A is plotted as a function of $\delta\mu$ in figure 3. We note that η is monotone increasing in $\delta\mu$, with $\eta \rightarrow 0$ as $\delta\mu \rightarrow 0$, and that η blows up as $\delta\mu \rightarrow 1$. In all cases B–D we have $\delta\mu \ll 1$, so that $\eta \ll 1$ is small, although due to the logarithmic form of η , we have $\delta \ll \eta$.

For large μ (cases D–F), we find that the heat transfer between phases, terms 3 and 4, dominate at leading order over an $O(1)$ lengthscale, so that we obtain a single-temperature model in the outer region of the domain. By combining the equations of conservation of energy for the gas and solid phases, we derive a single equation for the common, leading-order temperature $T_s = T_g = T$ in the $O(1)$ -lengthscale regions of the domain. We observe interesting counter-current behaviour in these cases D–F: since the gas and solid material flow in opposite directions, the net direction of advection for the common temperature T may be in either direction, and the dominant behaviour is different in either case. In particular, if the net heat flow is left-to-right (with the gas flow) then the natural temperature scaling of the steady-state case is determined by a balance of advection, term 1, and heat consumed by the chemical reaction, term 5, giving the temperature scaling θ_* , the solution of

$$\delta\theta_*^2 = \exp\left(-\frac{A}{\theta_*}\right). \quad (3.3)$$

Conversely, if the net heat flow is right-to-left with the solid, the temperature remains approximately uniform at the solid input temperature T^{in} . These are referred to as the subcases b and a respectively.

The asymptotic structures that we derive in cases B and C, characterised by the balance of heat transfer between the phases and material consumption over an $O(1)$ lengthscale, are quite different to the single-temperature behaviour of cases E and F. The analysis in case D

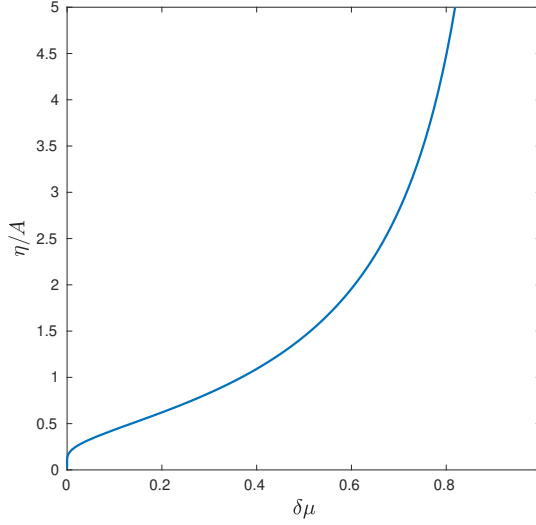


Figure 3: The variation of η/A with $\delta\mu$, according to (3.2). The curve approaches the origin as $\delta\mu \rightarrow 0$, and becomes unbounded as $\delta\mu \rightarrow 1$.

includes aspects of both these types of behaviour, and so demonstrates how the system varies from case C to E as the convective heat transfer coefficient is increased.

In each of the cases considered in Sections 4–9 below, we find explicit steady-state solutions at leading order, in every region of the domain except the boundary layer at $x = s(t)$. We construct composite, leading-order solutions in each case (restricting to steady state in cases D–F for simplicity).

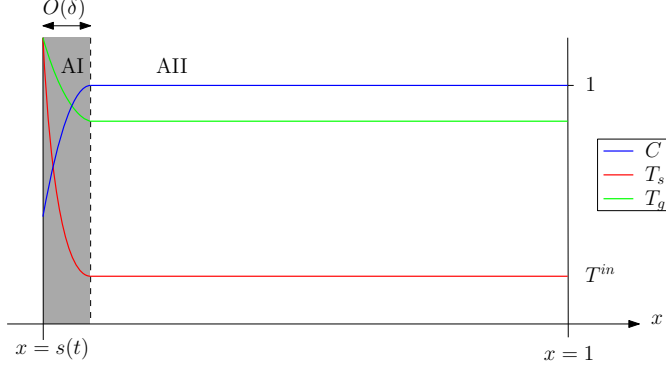
4. Case A: $\mu = 0$, no heat transfer

Firstly, we suppose that the heat transfer between the gas and solid phases is negligible over the lengthscale of the entire domain, so that $\mu \rightarrow 0$. The diagram in figure 4 is a schematic of the asymptotic structure in this case, and the changes of variable that we will make in each region of the domain are summarised in table 1. As in figure 4, throughout this paper we number the regions of the domain with roman numerals I, II etc., from left-to-right within the domain.

Since the convective heat transfer coefficient is zero, the gas problem decouples from the solid problem, and we may study the reduced problem for the solid variables only. This is, for $x \in (s(t), 1)$, (2.12a) and (2.12c) (with $\mu = 0$) and the boundary conditions for C and T_s as in (2.12g)–(2.12f). We may then integrate (2.12b) and (2.12d), using the boundary conditions for f and T_g at $x = s(t)$ given by (2.12f). This gives the gas variables f and T_g in terms of the solution s , C , and T_s of the solid problem:

$$f = f_* + \delta^{-1} \int_{x=s}^1 C \exp\left(A \left(1 - \frac{1}{T_s}\right)\right) dx, \quad (4.1a)$$

$$T_g = \frac{f_* T_s|_{x=s} + (\delta K)^{-1} \int_{x=s}^1 T_s C \exp\left(A \left(1 - \frac{1}{T_s}\right)\right) dx}{f_* + \delta^{-1} \int_{x=s}^1 C \exp\left(A \left(1 - \frac{1}{T_s}\right)\right) dx}. \quad (4.1b)$$

Figure 4: Schematic of the solution structure in case A: $\mu = 0$.

Region	Spatial Variable	Size of Q	Dominant terms in (3.1)	Dependent Variables
AI	$x = s(t) + \delta X$	$Q = O(1)$	1, 2, 5	C, f, T_s, T_g
AII	x	$Q \ll \delta T^{\text{in}}$	1	$C = \hat{C}, f = \hat{f},$ $T_s = T^{\text{in}} \hat{T}_s, T_g = \hat{T}_g$

Table 1: Summary of the asymptotic regions of the domain, and the changes of variable in these regions, for case A: $\mu = 0$.

We will see in the following analysis that the integral terms in (4.1) are $O(\delta)$, and so f and T_g are regular as $\delta \rightarrow 0$.

4.1. Region AII

We begin by considering the behaviour over an $O(1)$ lengthscale, which we denote region AII in figure 4. We recall that $T^{\text{in}} \ll 1$ is small, in the specific sense (2.14). At the boundary $x = 1$ we have $T_s = T^{\text{in}}$, and we therefore look for a solution expansion of the form

$$T_s = T^{\text{in}} \left(\hat{T}_s^0 + o\left(T^{\text{in}}\right) \right), \quad C = \hat{C}^0 + o\left(T^{\text{in}}\right), \quad (4.2)$$

and also expand the gas variables in region AII by

$$T_g = \hat{T}_g^0 + o\left(T^{\text{in}}\right), \quad f = \hat{f}^0 + o\left(T^{\text{in}}\right). \quad (4.3)$$

(Here we use hat notation to differentiate from the variables used in region AI below.) Since by (2.14) we have that $Q(T^{\text{in}}) \ll \delta T^{\text{in}}$, at leading order in (2.12a) and (2.12c) we obtain

$$\frac{\partial \hat{C}^0}{\partial t} - \frac{\partial \hat{C}^0}{\partial x} = 0, \quad \hat{C}^0 \left(\frac{\partial \hat{T}_s^0}{\partial t} - \frac{\partial \hat{T}_s^0}{\partial x} \right) = 0. \quad (4.4)$$

Solving, using the boundary conditions at $x = 1$, we must have, for all x :

$$\hat{T}_s^0 = 1, \quad \hat{C}^0 = 1. \quad (4.5)$$

Since \hat{T}_s and \hat{C} are constant to leading order, the gas variables in this region, given by (4.1), are also uniform. The error in these leading-order solutions is $O(\delta^{-1} Q(T^{\text{in}})) = o(T^{\text{in}})$, since $Q \ll \delta T^{\text{in}}$.

4.2. Region AI

We note that we cannot impose the boundary conditions at the free boundary $x = s(t)$ on the constant solution found in the previous section. We therefore look for a boundary layer at $x = s(t)$, denoted region AI, where $T_s = O(1) \gg T^{\text{in}}$. Since $\delta \ll 1$, we change variables, setting $x = s(t) + \delta X$. Since $T^{\text{in}} \gg \delta$, we look for an expansion in powers of T^{in} in region AI, setting

$$T_s = T_s^0(X, t) + O(T^{\text{in}}), \quad C = C^0(X, t) + O(T^{\text{in}}), \quad s = s^0(t) + O(T^{\text{in}}). \quad (4.6)$$

We also expand the gas variables in powers of T^{in} , taking

$$T_g = T_g^0(X, t) + O(T^{\text{in}}), \quad f = f^0(X, t) + O(T^{\text{in}}). \quad (4.7)$$

Substituting the expansions (4.6) into (2.12a) and (2.12c), at leading order we obtain

$$-(\dot{s}_0 + 1) \frac{\partial C^0}{\partial X} = -C^0 \exp\left(A \left(1 - \frac{1}{T_s^0}\right)\right), \quad (4.8a)$$

$$-(\dot{s}_0 + 1) C^0 \frac{\partial T_s^0}{\partial X} = \frac{\partial^2 T_s^0}{\partial X^2} - \gamma C^0 \exp\left(A \left(1 - \frac{1}{T_s^0}\right)\right), \quad (4.8b)$$

where the dot notation denotes a time derivative, $\dot{s}_0 = ds_0/dt$. From (2.12f), we have the boundary conditions

$$C^0 = C_*, \quad T_s^0 = \frac{\rho}{s_0}, \quad \text{at } X = 0. \quad (4.8c)$$

As $X \rightarrow \infty$ we match with the outer region AII, and so require

$$C^0 \rightarrow 1, \quad T_s^0 \rightarrow 0 \quad \text{as } X \rightarrow \infty. \quad (4.8d)$$

The far-field temperature must approach zero in (4.8d) so that the chemical reaction rate Q approaches zero in this limit. This is necessary for the problem to be correctly specified. Region AI is the reaction region, with the energy for the reaction provided by the heat radiation on the boundary $x = s(t)$. This reduced system (4.8) in region AI determines T_s^0 , C^0 , and also gives a relation between \dot{s}_0 and s_0 . We solve (4.8) numerically in Section 10 below. We note that the leading-order system (4.8) is quasi-steady, in that the only time-derivatives are \dot{s}_0 , with no time-derivatives of T_s or C_s at leading order. Since the region-AII problem has a constant, time-independent solution, we see that the entire system is quasi-steady in case A. The relation between \dot{s}_0 and s_0 found numerically as part of the solution of (4.8) in Section 10 therefore describes fully the quasi-steady time-dependent behaviour of the system. In particular we may find steady state(s) of the system for which $\dot{s} = 0$.

In fact, we obtain a quasi-steady boundary layer problem, similar to (4.8), in each of the non-zero μ cases explored below. In cases with larger μ , however, we will find fully time-dependent behaviour outside of region I, so that, even though the region-I behaviour is still quasi-steady, the overall system is not quasi-steady. In the analysis of many of these cases we find and discuss the time-dependent solutions, but when computing solutions numerically in Sections 10–11 we will restrict to the steady state case, for simplicity.

Given the solution of this solid problem (4.8), from (4.1) with the change of variables

469 $x = s(t) + \delta X$, we see that the leading-order gas variables in region AI are

$$470 \quad f^0(X, t) = f_* + (1 + \dot{s}_0)(C^0 - C_*), \quad (4.9a)$$

$$471 \quad T_g^0(X, t) = \frac{\frac{f_* \rho}{s_0} + K^{-1} \int_{\bar{X}=0}^X T_s^0 C^0 \exp\left(A\left(1 - \frac{1}{T_s^0}\right)\right) d\bar{X}}{f_* + (1 + \dot{s}_0)(C^0 - C_*)}. \quad (4.9b)$$

473 In region AII both \hat{T}_g^0 and \hat{f}^0 are uniform. By matching with region AI at $x = s_0$, we find

$$474 \quad \hat{f}^0(t) = F_s(t) := f_* + (1 + \dot{s}_0)(1 - C_*), \quad (4.10a)$$

$$475 \quad \hat{T}_g^0(t) = G_s(t) := \frac{\frac{f_* \rho}{s_0} + K^{-1} \int_{\bar{X}=0}^{\infty} T_s^0 C^0 \exp\left(A\left(1 - \frac{1}{T_s^0}\right)\right) d\bar{X}}{f_* + (1 + \dot{s}_0)(1 - C_*)}. \quad (4.10b)$$

477 4.3. Composite solution

478 We construct composite leading-order solutions for case A as follows. Since C , f , and T_g
479 are $O(1)$ in all regions of the domain, and uniform to leading order in region AII, the
480 leading-order composite solutions in case A (which we denote by superscript A) are simply

$$481 \quad C^A = C^0\left(\frac{x - s_0(t)}{\delta}, t\right), \quad f^A = f^0\left(\frac{x - s_0(t)}{\delta}, t\right), \quad T_g^A = T_g^0\left(\frac{x - s_0(t)}{\delta}, t\right). \quad (4.11)$$

483 However, T_s is $O(1)$ in region AI, but $O(T^{\text{in}})$ in region AII. We note that this small temperature
484 in region AII must induce a $O(T^{\text{in}})$ switchback correction (Hinch 1991) to the leading-order
485 solution in the boundary layer AI. We therefore have some freedom in how to choose the
486 leading-order composite expansion (Hinch 1991). For simplicity we choose to set the $O(T^{\text{in}})$
487 correction in region AI to be uniform, and equal to T^{in} . Thus we form the composite expansion

$$488 \quad T_s^A = T_s^0\left(\frac{x - s_0(t)}{\delta}\right) + T^{\text{in}}, \quad (4.12)$$

489 which has $O(T^{\text{in}})$ error in region AI, and $O(\delta^{-1}Q(T^{\text{in}}))$ error in region AII.

490 In case A, we have seen that all the material consumption (chemical reaction) occurs within
491 the boundary layer AI at $x = s(t)$, and that all variables have constant, uniform profiles in
492 the outer region AII. We also observed that the leading-order behaviour is quasi-steady
493 throughout the domain, with the time-derivatives of s in region AI the only time-derivatives
494 in the reduced problem.

495 5. Case B: $\mu = O(\eta)$, small heat transfer

496 We now let $\mu > 0$, and study the distinguished limit $\mu = O(\eta)$, with η defined in (3.2). We
497 will see that for this rate of heat transfer between phases, the solid temperature in the outer
498 region of the domain becomes high enough for the chemical reaction to be non-negligible.
499 In this section, we write $\mu = M\eta_B \ll 1$, where $M = O(1)$ and $\eta_B = \eta_B(\delta, A)$ is the smaller
500 non-trivial solution of

$$501 \quad \eta_B = \frac{A}{\log\left(\frac{1}{\delta\eta_B}\right)}, \quad (5.1)$$

502 namely

$$503 \quad \eta_B = \frac{1}{\delta} \exp(W_{-1}(-A\delta)) = \frac{A}{-\log(A\delta)} \left(1 + O\left(\frac{\log(-\log(A\delta))}{-\log(A\delta)}\right)\right) \quad (5.2)$$

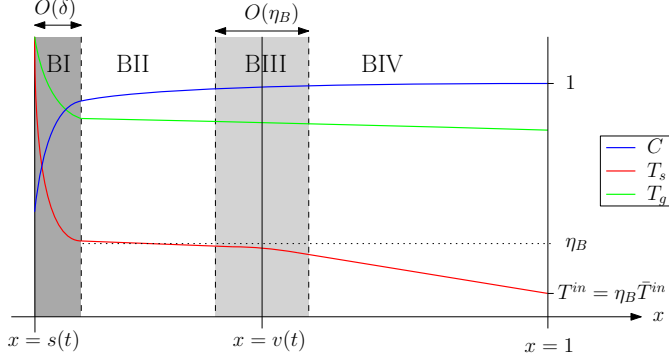


Figure 5: Schematic of the solution structure in case B: $\mu = O(\eta_B)$.

Region	Spatial Variable	Size of Q	Dominant terms in (3.1)	Dependent Variables
BI	$x = s(t) + \delta X$	$Q = O(1)$	1, 2, 5	C, f, T_s, T_g
BII	x	$Q = O(\delta\eta_B)$	3, 5	$C = \hat{C}, f = \hat{f},$ $T_s = \eta_B(1 + \eta_B \hat{T}_s), T_g = \hat{T}_g$
BIII	$x = v(t) + \eta_B y$	$Q = O(\delta\eta_B)$	1, 3, 5	$C = \bar{C}, f = \bar{f},$ $T_s = \eta_B(1 + \eta_B \bar{T}_s), T_g = \bar{T}_g$
BIV	x	$Q \ll \delta\eta_B$	1, 3	$C = \bar{C}, f = \bar{f},$ $T_s = \eta_B \bar{T}_s, T_g = \bar{T}_g$

Table 2: Summary of the asymptotic regions of the domain, and the changes of variable in these regions, for case B: $\mu = O(\eta_B)$.

where W_{-1} is the lower real branch of the Lambert W function. We note that $\eta_B \rightarrow 0$ as $\delta \rightarrow 0$. In this section, we will expand our dependent variables in powers of η_B (rather than in powers of T^{in} as in case A), but to leading order this is equivalent to expanding in powers of $1/(-\log(A\delta))$. We choose to retain the η_B notation as it makes for easy comparison with subsequent cases. A schematic of the asymptotic structure in case B is shown in figure 5, and the changes of variable are summarised table 2.

5.1. Region BI

As in case A, we look for a reaction region at the free boundary $x = s(t)$. This is an $O(\delta)$ boundary layer at $x = s(t)$, denoted region BI in figure 5. We look for an expansion solution in powers of η_B in region BI, namely

$$T_s = T_s^0(X, t) + \eta_B T_s^1(X, t) + O(\eta_B^2), \quad C = C^0(X, t) + \eta_B C^1(X, t) + O(\eta_B^2), \quad (5.3a)$$

$$T_g = T_g^0(X, t) + \eta_B T_g^1(X, t) + O(\eta_B^2), \quad f = f^0(X, t) + \eta_B f^1(X, t) + O(\eta_B^2), \quad (5.3b)$$

$$s = s_0(t) + \eta_B s_1(t) + O(\eta_B^2). \quad (5.3c)$$

Substituting into (2.12), the equations (2.12b) and (2.12d) for the gas variables decouple on this lengthscale, and so we obtain exactly the same system at leading order for just the solid variables T_s^0 , C^0 , and s_0 as in case A, namely (4.8). We will find below that $C = 1 + O(\eta_B)$

everywhere outside of region BI, and so the matching conditions as $X \rightarrow \infty$ are also identical to case A, given by (4.8d).

5.2. Region BII

Since the convective heat transfer rate is non-zero, unlike case A, the equations for the gas variables do not decouple in (2.12) in the entire domain. Instead, outside the boundary layer BI, we must have heat transfer between the solid and gas phases, and expect the solid temperature scaling $T_s \approx \eta_B$. We therefore make the rescaling

$$T_s = \eta_B (1 + \eta_B \hat{T}_s), \quad (5.4)$$

in the $O(1)$ -lengthscale outer region, denoted region BII, and for clarity of notation we also write $C = \hat{C}$, $f = \hat{f}$, and $T_g = \hat{T}_g$. The chemical reaction rate here is therefore

$$\hat{Q}(\hat{C}, \hat{T}_s) = \hat{C} \exp \left(A \left(1 - \frac{1}{T_s} \right) \right) = \hat{C} e^A \delta \eta_B \left(e^{A \hat{T}_s} + O(\eta_B) \right), \quad (5.5)$$

and thus the heat consumed by the chemical reaction at this temperature η_B is the same order ($\delta \eta_B$) as the heat transferred from the gas to the solid. We expand all dependent variables in powers of $\eta_B \ll 1$, setting

$$\begin{aligned} \hat{T}_s &= \hat{T}_s^0(x, t) + O(\eta_B), & \hat{C} &= \hat{C}^0(x, t) + O(\eta_B), \\ \hat{T}_g &= \hat{T}_g^0(x, t) + O(\eta_B), & \hat{f} &= \hat{f}^0(x, t) + O(\eta_B), \end{aligned} \quad (5.6)$$

Since the reaction rate is small, at leading order we find that \hat{f}^0 and \hat{T}_g^0 are uniform in x . Matching at $x = s(t)$ with region BI, using the same notation as in (4.10), we find

$$\hat{f}^0 = F_s, \quad \hat{T}_g^0 = G_s. \quad (5.7)$$

From (2.12a) we find that \hat{C}^0 is conserved along characteristics travelling right-to-left through region BII. As we will see below, C is uniform to leading order over all regions to the right of this, and so by using the boundary condition at $x = 1$, and matching, we will find that $\hat{C}^0 = 1$ is constant throughout region BII. The solid heat equation (2.12c), at leading order (order η_B), reduces to

$$M \hat{T}_g^0 = \gamma \hat{C}^0 \exp \left(A(1 + \hat{T}_s^0) \right), \quad (5.8)$$

so that \hat{T}_s^0 is also uniform, and given by

$$\hat{T}_s^0 = \frac{1}{A} \log \left(\frac{M G_s}{\gamma} \right) - 1. \quad (5.9)$$

This completes the leading-order analysis in region BII. Physically, in this region all the heat transferred from the gas to the solid is used for the chemical reaction, so that the solid temperature remains uniform. Region BII is a reaction region (like region BI), although here the heat for the chemical reaction is provided by the heat transfer between phases, rather than the radiation onto the free boundary.

5.3. Region BIV

For this size of the convective heat transfer coefficient $\mu = O(\eta_B)$, there is also a second possible dominant balance on an $O(1)$ lengthscale, namely the balance of advection (term 1 in (3.1)) with the heat transfer from the gas (term 3 in (3.1)), when the chemical reaction rate is small $Q \ll \delta \eta_B$. We see that this balance occurs at the right-hand side of the domain (denoted region BIV) since, near the boundary $x = 1$, $T_s \approx T^{\text{in}}$, and we note that $\eta_B > T^{\text{in}}$, by

the assumption (2.14). In region BIV, the solid material is therefore heated up to the critical reacting temperature η_B by the heat transfer from the gas. To study region BIV we make the change of variables

$$T_s = \eta_B \bar{T}_s, \quad (5.10)$$

for $\bar{T}_s < 1$, and we write the boundary value $T^{\text{in}} = \eta_B \bar{T}^{\text{in}}$, where by (2.14) $\bar{T}^{\text{in}} < 1$. For clarity of notation we also write $C = \bar{C}$, $f = \bar{f}$, and $T_g = \bar{T}_g$ in this region BIV. Then the chemical reaction rate in BIV is

$$Q = \bar{C} \exp \left(A \left(1 - \frac{1}{\eta_B \bar{T}_s} \right) \right) = \bar{C} e^A (\delta \eta_B)^{1/\bar{T}_s} \ll \delta \eta_B. \quad (5.11)$$

Again we expand in powers of η_B , setting

$$\begin{aligned} \bar{T}_s &= \bar{T}_s^0(x, t) + O(\eta_B), & \bar{C} &= \bar{C}^0(x, t) + O(\eta_B), \\ \bar{T}_g &= \bar{T}_g^0(x, t) + O(\eta_B), & \bar{f} &= \bar{f}^0(x, t) + O(\eta_B). \end{aligned} \quad (5.12)$$

At leading order in (2.12a), (2.12b) and (2.12d), we see that \bar{C}^0 , \bar{f}^0 , and \bar{T}_g^0 are all uniform through region BIV. From (2.12c) we find that \bar{T}_s^0 satisfies

$$\bar{C}^0 \left(\frac{\partial \bar{T}_s^0}{\partial t} - \frac{\partial \bar{T}_s^0}{\partial x} \right) = M \bar{T}_g^0. \quad (5.13)$$

By the method of characteristics, applying the boundary conditions at $x = 1$, we find

$$\bar{T}_s^0 = \bar{T}^{\text{in}} + \int_{\xi=0}^{1-x} \frac{M \bar{T}_g^0(t + x - 1 + \xi)}{\bar{C}^0(t + x - 1 + \xi)} d\xi. \quad (5.14)$$

The integrand in (5.14) is positive, and so for any fixed t , \bar{T}_s^0 increases monotonically as x decreases from 1 into the domain. Thus in region BIV no chemical reaction occurs since the solid material is below the critical temperature η_B , and the transfer of heat from the gas to the solid has the effect of heating up the solid material.

5.4. Region BIII

The solution in region BIV is only valid so long as $\bar{T}_s^0 < 1$. As \bar{T}_s^0 approaches 1 (so that T_s approaches the critical temperature η_B), there must be a transition region, denoted region BIII, over which the chemical reaction rate (term 5 in (3.1)) enters the dominant balance. Physically, region BIII is the transition region where the heat transferred from gas to solid ceases to be used for the chemical reaction, and is instead used to heat the solid up from its input temperature T^{in} . To analyse this region we use the change of variables

$$T_s = \eta_B (1 + \eta_B \tilde{T}_s). \quad (5.15)$$

The other variables are denoted $C = \tilde{C}$, $f = \tilde{f}$, and $T_g = \tilde{T}_g$ in region BIII for clarity. Since we require all of the heat loss to the chemical reaction (term 5 in (3.1)), heat transfer from gas to solid (term 3), and advection of heat within the solid (term 1) to balance, we require an $O(\eta_B)$ lengthscale, and so make the change of variables $x = v(t) + \eta_B y$, where $y = O(1)$, and $v(t)$, to be determined, is the position of the transition layer BIII. As in regions BII and BIV, we see from (2.12a), (2.12b) and (2.12d) that to leading order in η_B all of \tilde{C} , \tilde{f} , and \tilde{T}_g are uniform through region BIII. Matching to both left (region BII) and right (region BIV), we see that throughout regions BII–BIV

$$\hat{C}^0 = \bar{C}^0 = 1, \quad \hat{f}^0 = \bar{f}^0 = F_s(t), \quad \hat{T}_g^0 = \bar{T}_g^0 = G_s(t). \quad (5.16)$$

598 With these changes of variable, and expanding in powers of η_B , at leading order in (2.12c)
 599 we obtain the ODE

$$600 \quad -(\dot{v} + 1) \frac{\partial \tilde{T}_s^0}{\partial y} = M G_s - \gamma \exp(A(1 + \tilde{T}_s)), \quad (5.17)$$

601 for \tilde{T}_s^0 , which has solution

$$602 \quad \tilde{T}_s^0 = -1 - \frac{1}{A} \log \left(\frac{\gamma}{M G_s} \left[1 + B \exp \left(\frac{A M G_s}{\dot{v} + 1} y \right) \right] \right). \quad (5.18)$$

603 The position, $v(t)$, of the transition layer, and the constant of integration, $B(t)$, must be
 604 determined by matching with the neighbouring regions. We note that v is fixed by the leading
 605 order matching

$$606 \quad 1 = \tilde{T}_s^0 \Big|_{x=v} = \bar{T}^{\text{in}} + M \int_{\xi=0}^{1-v} G_s(t + v - 1 + \xi) d\xi. \quad (5.19)$$

607 Since the integrand $G_s > 0$ is positive, the integral is decreasing with v , and there is therefore
 608 a unique solution, $v(t) < 1$, of (5.19), for every t . The value of B in (5.18) may be fixed by
 609 matching at higher order, which requires the $O(\eta_B)$ correction in all regions of the domain
 610 BI–BIV.

611 We note that the position $v(t)$ given by (5.19) requires no knowledge of the form \tilde{T}_s^0 of
 612 the solution in region BIII. The function of region BIII is therefore to simply smooth the
 613 transition from uniform T_s in region BII, to \tilde{T}_s^0 given by (5.14) in region BIV.

614 We also notice that the position, $v(t)$, of the transition layer lies within the domain so long
 615 as $v(t) > s_0(t)$. From the equation (5.19) for $v(t)$, we see that if any of M , G_s , or $1 - s_0$
 616 are too small, then $v(t) < s_0(t)$. In this case there is no region BII or BIII: region BIV
 617 fills the entire domain $[s_0(t), 1]$, except for the boundary layer at $x = s_0$. We see that our
 618 solution approaches the solution for case A in Section 4 as M becomes small, since in this
 619 case $v(t) < s_0(t)$, and so everywhere in $[s_0(t), 1]$ we must have

$$620 \quad C \sim 1, \quad f \sim F_s, \quad T_g \sim G_s, \quad T_s = \eta_B \bar{T}_s^0 = \eta_B (\bar{T}^{\text{in}} + O(M)) \sim T^{\text{in}}. \quad (5.20)$$

622 5.5. Composite solution

623 Since C , f , and T_g are uniform at leading order outside region BI, the leading-order composite
 624 solutions are simply

$$625 \quad C^{\text{B}} = C^0 \left(\frac{x - s_0(t)}{\delta} \right), \quad f^{\text{B}} = f^0 \left(\frac{x - s_0(t)}{\delta} \right), \quad T_g^{\text{B}} = T_g^0 \left(\frac{x - s_0(t)}{\delta} \right). \quad (5.21)$$

627 As in case A, we note that $T_s = O(1)$ in region BI, but is $O(\eta_B)$ in all other regions. We
 628 construct a leading-order composite solution by assuming that the $O(\eta_B)$ correction in region
 629 BI is simply uniform, and equal to η_B , so that the composite T_s solution is accurate with
 630 $O(\eta_B)$ error in region BI, and with $O(\eta_B^2)$ error in regions BII–BIV. The solution is defined
 631 piecewise on either side of the transition layer BIII, centred at the point $x = v(t)$, where the
 632 solution is continuous by construction. We therefore use the composite solution

$$633 \quad T_s^{\text{B}} = \begin{cases} T_s^0 \left(\frac{x - s_0(t)}{\delta} \right) + \eta_B, & \text{if } x < v(t), \\ \eta_B \bar{T}_s^0(x, t), & \text{if } x \geq v(t), \end{cases} \quad (5.22)$$

634 where \bar{T}_s^0 is given by (5.14).

635 Thus in case B, while $\mu = O(\eta_B)$ is non-zero and so there is some heat transfer between

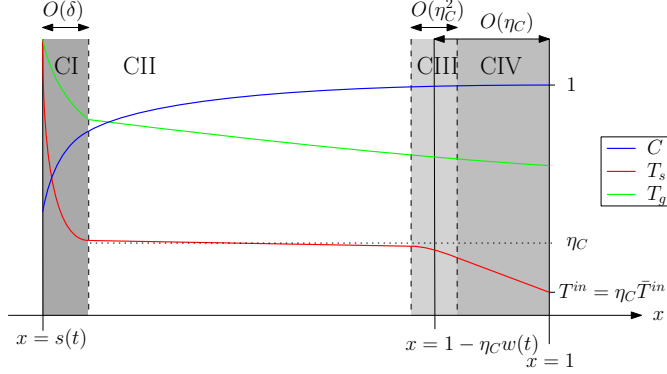


Figure 6: Schematic of the solution structure in case C: $\mu = O(1)$.

phases, only an $O(\eta_B)$ amount of chemical reaction occurs outside region BI, and this only if $v(t) > s_0(t)$. The primary role of the heat transferred from the gas to the solid is to heat up the solid material. While this does not affect the leading-order problem in region BI, which is the same as that in AI in case A, it reduces its accuracy: there is now an $O(\eta_B)$ “switchback” correction term in region BI, greater than the $O(T^{\text{in}})$ correction in case A.

6. Case C: $\mu = O(1)$, moderate heat transfer

In this section we suppose $\mu = O(1)$, so that heat transfer from the gas to the solid is significant over the domain $[s(t), 1]$. As in case B, over an $O(1)$ domain we have a balance between the heat transferred gas to solid (term 3) and the heat consumed by the chemical reaction (term 5) in (3.1). Since now $\mu = O(1)$, both these terms must be $O(1)$, and the temperature scaling η , given by (3.2), is

$$\eta_C = \frac{A}{\log\left(\frac{1}{\delta}\right)}. \quad (6.1)$$

We note that $\delta \ll \eta_B < \eta_C \ll 1$. With $T_s \sim \eta_C$, the chemical reaction rate has $O(1)$ effect in the equations of mass conservation (2.12a)–(2.12b). Thus, unlike in cases A and B, we expect $O(1)$ material consumption in both the boundary layer, region CI, at $x = s(t)$, and also in an $O(1)$ region of the domain. In fact, as we will show in Section 7 below, the analysis for case C holds so long as $\mu \ll O(\log(\log(1/\delta)))$. A schematic of the asymptotic structure in this case is given in figure 6, and the changes of variable in each region is summarised in table 3.

6.1. Region CI

As in the previous cases, we find an $O(\delta)$ reaction region (region CI) at $x = s(t)$, where the heat for the reaction is provided by the radiation onto the free boundary. As before, we make the change of variables $x = s(t) + \delta X$, and expand the dependent variables in powers of η_C , by

$$T_s = T_s^0(X, t) + \eta_C T_s^1(X, t) + O(\eta_C^2), \quad C = C^0(X, t) + \eta_C C^1(X, t) + O(\eta_C^2), \quad (6.2a)$$

$$T_g = T_g^0(X, t) + \eta_C T_g^1(X, t) + O(\eta_C^2), \quad f = f^0(X, t) + \eta_C f^1(X, t) + O(\eta_C^2), \quad (6.2b)$$

$$s = s_0(t) + \eta_C s_1(t) + O(\eta_C^2). \quad (6.2c)$$

Region	Spatial Variable	Size of Q	Dominant terms in (3.1)	Dependent Variables
CI	$x = s(t) + \delta X$	$Q = O(1)$	1, 2, 5	C, f, T_s, T_g
CII	x	$Q = O(\delta)$	3, 5	$C = \hat{C}, f = \hat{f},$ $T_s = \eta(1 + \eta\hat{T}_s), T_g = \hat{T}_g$
CIII	$x = 1 - \eta w(t) - \eta^2 y$	$Q = O(\delta)$	1, 3, 5	$C = \tilde{C}, f = \tilde{f},$ $T_s = \eta(1 + \eta\tilde{T}_s), T_g = \tilde{T}_g$
CIV	$x = 1 - \eta Y$	$Q \ll \delta$	1, 3	$C = \bar{C}, f = \bar{f},$ $T_s = \eta\bar{T}_s, T_g = \bar{T}_g$

Table 3: Summary of the asymptotic regions of the domain, and the changes of variable in these regions, for case C: $\mu = O(1)$.

We obtain the same leading-order system of equations (4.8a)–(4.8c) in region CI as in cases A and B. As $X \rightarrow \infty$, we still require $T_s^0 \rightarrow 0$ in order for the problem to be correctly specified. However, since the chemical reaction rate is $O(1)$ in the outer region, we will no longer have uniform concentration at leading order in the outer region. We must therefore impose the far-field conditions

$$T_s^0 \rightarrow 0, \quad C^0 \rightarrow C^\infty(t) \quad \text{as } X \rightarrow \infty, \quad (6.3)$$

where $C^\infty(t)$ is yet to be determined by matching with the outer region. Thus we can no longer solve the region CI problem independently of the rest of the domain: it is now intrinsically coupled with the outer problem, since C varies at leading order over the outer region. The leading-order gas variables within region CI are given by (4.9), but the far-field values as $X \rightarrow \infty$ are now

$$f^0 \rightarrow F_s(t) := f_* + (1 + \dot{s}_0)(C^\infty - C_*), \quad (6.4a)$$

$$T_g^0 \rightarrow G_s(t) := \frac{\frac{f_* \rho}{s_0} + K^{-1} \int_{\bar{X}=0}^{\infty} T_s^0 C^0 \exp\left(A\left(1 - \frac{1}{T_s^0}\right)\right) d\bar{X}}{f_* + (1 + \dot{s}_0)(C^\infty - C_*)}. \quad (6.4b)$$

6.2. Region CII

Outside region CI, over an $O(1)$ lengthscale, the heat transferred from the gas to the solid is sufficient that the chemical reaction is a dominant effect, and the solid temperature remains close to uniform. We refer to this region as region CII. Like region BII in case B, region CII is a reaction region within which the energy for the reaction is provided by the heat transferred between phases. Unlike region BII, however, the heat transfer is now fast enough that the gas temperature decreases through this region, rather than remaining uniform. In region CII, we make the rescaling

$$T_s = \eta_C (1 + \eta_C \hat{T}_s), \quad (6.5)$$

and we also use the notation $C = \hat{C}$, $f = \hat{f}$, and $T_g = \hat{T}_g$ for clarity. We expand the dependent variables in powers of η_C , setting

$$\begin{aligned} \hat{T}_s &= \hat{T}_s^0(x, t) + O(\eta_C), & \hat{C} &= \hat{C}^0(x, t) + O(\eta_C), \\ \hat{T}_g &= \hat{T}_g^0(x, t) + O(\eta_C), & \hat{f} &= \hat{f}^0(x, t) + O(\eta_C). \end{aligned} \quad (6.6)$$

At leading order, the system (2.12a)–(2.12d) becomes

$$\frac{\partial \hat{C}^0}{\partial t} - \frac{\partial \hat{C}^0}{\partial x} = -\hat{C}^0 \exp \left(A \left(1 + \hat{T}_s^0 \right) \right), \quad (6.7a)$$

$$\frac{\partial \hat{f}^0}{\partial x} = \hat{C}^0 \exp \left(A \left(1 + \hat{T}_s^0 \right) \right), \quad (6.7b)$$

$$\mu \hat{T}_g^0 = \gamma \hat{C}^0 \exp \left(A \left(1 + \hat{T}_s^0 \right) \right), \quad (6.7c)$$

$$K \frac{\partial}{\partial x} \left(\hat{f}^0 \hat{T}_g^0 \right) = -\mu \hat{T}_g^0. \quad (6.7d)$$

Combining (6.7b)–(6.7d) we obtain the reduced system

$$\frac{\partial \hat{f}^0}{\partial x} = \frac{\mu}{\gamma} \hat{T}_g^0, \quad K \frac{\partial}{\partial x} \left(\hat{f}^0 \hat{T}_g^0 \right) = -\mu \hat{T}_g^0, \quad (6.8)$$

for \hat{f}^0 and \hat{T}_g^0 . Matching with region CI, we must have $\hat{f}^0 = F_s(t)$ and $\hat{T}_g^0 = G_s(t)$ at $x = s_0$. Combining (6.8), and using the boundary conditions at $x = s_0$ we find the first integral

$$\hat{f}^0 \left(\gamma + K \hat{T}_g^0 \right) = F_s(\gamma + K G_s). \quad (6.9)$$

Using (6.9) to eliminate \hat{f}^0 from the first equation (6.8), we obtain a separable equation for \hat{T}_g^0 , namely

$$\frac{1}{\hat{T}_g^0 (\gamma + K \hat{T}_g^0)^2} \frac{\partial \hat{T}_g^0}{\partial x} = -\frac{\mu}{\gamma K F_s (\gamma + K G_s)}, \quad (6.10)$$

with solution

$$\hat{T}_g^0(x, t) = -\frac{\gamma W(a_C)}{K(1 + W(a_C))}, \quad (6.11a)$$

where W is the principle branch of the Lambert W function, and $a_C = a_C(x, t)$ is given by

$$a_C(x, t) = -\frac{K G_s}{\gamma + K G_s} \exp \left(-\frac{1}{\gamma + K G_s} \left(\frac{\gamma \mu}{K F_s} (x - s_0) + K G_s \right) \right). \quad (6.11b)$$

From (6.9), we therefore find

$$\hat{f}^0 = \frac{F_s(\gamma + K G_s)}{\gamma + K \hat{T}_g^0}. \quad (6.11c)$$

Given \hat{T}_g^0 from (6.11), the leading-order concentration \hat{C}^0 satisfies (6.7a), or

$$\frac{\partial \hat{C}^0}{\partial t} - \frac{\partial \hat{C}^0}{\partial x} = -\frac{\mu}{\gamma} \hat{T}_g^0. \quad (6.12)$$

Matching with region CI at $x = s_0(t)$, we require $\hat{C}^0 = C^\infty(t)$ at $x = s_0(t)$, and we will see below that the correct matching condition for \hat{C}^0 at the right side of region CII is $\hat{C}^0 = 1$ at $x = 1$. By the method of characteristics, (6.12) with the boundary condition at $x = 1$ has solution

$$\hat{C}^0(x, t) = 1 - \frac{\mu}{\gamma} \int_{\xi=0}^{1-x} \hat{T}_g^0(1 - \xi, \xi + t + x - 1) d\xi, \quad (6.13)$$

for $\hat{T}_g^0(x, t)$ given by (6.11a). Evaluating at $x = s_0(t)$, the matching condition for \hat{C}^0 gives

$$C^\infty(t) = 1 - \frac{\mu}{\gamma} \int_{\xi=0}^{1-s_0(t)} \hat{T}_g^0(1-\xi, \xi+t+s_0(t)-1) d\xi. \quad (6.14)$$

Since \hat{T}_g^0 depends on s_0 , F_s , and G_s , we see that C^∞ depends on these as well. Physically, the heat and flux of gas leaving region CI determine the rate of solid material consumption in region CII, which affects the position of the free boundary s_0 (found as part of the solution of the region CI problem), and therefore the gas temperature. The processes in regions CI and CII are thus fully coupled. However, since we have solved the region CII problem to find $C^\infty(t)$, at leading order we are left with the region CI problem (4.8a)–(4.8c) with far-field condition (6.3), with $C^\infty(t)$ given by (6.14).

Concluding the analysis in region CII, we find from (6.7c) that

$$\hat{T}_s^0 = \frac{1}{A} \log \left(\frac{\mu \hat{T}_g^0}{\gamma \hat{C}^0} \right) - 1. \quad (6.15)$$

given the forms (6.11a) of \hat{T}_g^0 and (6.13) of \hat{C}^0 .

6.3. Region CIV

In region CII, we have $T_s = \eta_C + O(\eta_C^2)$, and so we cannot impose the boundary condition $T_s = T^{\text{in}}$ at $x = 1$ (as discussed for case B, the condition (2.14) ensures $T^{\text{in}} < \eta_C$). There must therefore be a second boundary layer at $x = 1$, within which the solid temperature is heated from its input temperature T^{in} up to the critical temperature η_C . This heating region is analogous to region BIV in case B, and we denote it region CIV. In region CIV we change variables, setting

$$T_s = \eta_C \bar{T}_s, \quad (6.16)$$

with $\bar{T}_s < 1$, so that

$$\bar{Q} := Q(C, \eta_C \bar{T}_s) = O\left(\delta^{1/\bar{T}_s}\right) \ll \delta, \quad (6.17)$$

and thus we cannot expect a dominant balance in the solid heat equation (2.12c) between the heating from the gas and heat lost to chemical reaction. Instead, we find a balance between the heating from the gas and the advection term, which fixes the lengthscale of region CIV to be $O(\eta_C)$. Within region CIV we therefore make the change of variables $x = 1 - \eta_C Y$, where $Y = O(1)$ is positive. For clarity of notation, we set $C = \bar{C}$, $f = \bar{f}$, and $T_g = \bar{T}_g$ in region CIV, and we also rewrite the input temperature $T^{\text{in}} = \eta_C \bar{T}^{\text{in}}$, so that the boundary condition becomes

$$\bar{T}_s = \bar{T}^{\text{in}} \quad \text{at } Y = 0. \quad (6.18)$$

Again, we expand in powers of η_C , setting

$$\begin{aligned} \bar{T}_s &= \bar{T}_s^0(Y, t) + O(\eta_C), & \bar{C} &= \bar{C}^0(Y, t) + O(\eta_C), \\ \bar{T}_g &= \bar{T}_g^0(Y, t) + O(\eta_C), & \bar{f} &= \bar{f}^0(Y, t) + O(\eta_C). \end{aligned} \quad (6.19)$$

Due to the short lengthscale, at leading order in (2.12a), (2.12b), and (2.12d), we see that all of \bar{C}^0 , \bar{f}^0 , and \bar{T}_g^0 are uniform across region CIV. The boundary condition at $Y = 0$ (or $x = 1$) fixes $\bar{C}^0 = 1$, while \bar{f}^0 and \bar{T}_g^0 must be fixed by matching to the left. At leading order

in (2.12c), we find that the solid temperature \bar{T}_s^0 satisfies

$$\frac{\partial \bar{T}_s^0}{\partial Y} = \mu \bar{T}_g^0, \quad (6.20)$$

and thus, using the boundary condition (6.18), we find that \bar{T}_s^0 is linear in Y :

$$\bar{T}_s^0 = \bar{T}^{\text{in}} + \mu \bar{T}_g^0 Y. \quad (6.21)$$

6.4. Region CIII

Exactly as in case B, the solution (6.21) in region CIV is valid only while $\bar{T}_s^0 < 1$, and we cannot directly match the linear profile (6.21) with the constant $T_s \sim \eta_C$ in region CII. Thus, as in case B, we must introduce a transition layer, region CIII, between regions CII and CIV, in which the heat transferred from the gas is no longer used in the chemical reaction, but is instead used to heat the solid material from its input temperature T^{in} . In this transition layer, we must have $T_s \approx \eta_C$, and we expect a balance between all three of the heat advection (term 1), heat transfer from the gas (term 3), and heat loss to the chemical reaction (term 5) in (3.1). The lengthscale of such a region must therefore be $O(\eta_C^2)$. We may show, as in case B, that all of f , T_g and C are uniform across region CIII, so that matching across CII–CIV, we find

$$\hat{C}^0|_{x=1} = \bar{C}^0 = 1, \quad F_1(t) := \hat{f}^0|_{x=1} = \bar{f}^0, \quad G_1(t) := \hat{T}_g^0|_{x=1} = \bar{T}_g^0. \quad (6.22)$$

(This fixes the boundary condition at $x = 1$ for \hat{C}^0 , in region CII.) As in case B, we find that the ODE for the solid temperature variation simply smooths the transition from region CII to region CIV. The changes of variable for this analysis are summarised in table 3. The position $w(t)$ of the transition layer is found by matching T_s across regions CIII–CIV, which, at leading order, requires $1 = \bar{T}^{\text{in}} + \mu G_1 w$, so that

$$w(t) = \frac{1}{\mu G_1(t)} (1 - \bar{T}^{\text{in}}). \quad (6.23)$$

6.5. Composite solution

As in previous cases, we may construct a leading-order composite solution. Since C , f , and T_g are $O(1)$ in all regions, and uniform in regions CIII and CIV, the composite solutions are

$$C^C = C^0 \left(\frac{x - s_0(t)}{\delta} \right) + \hat{C}^0(x, t) - C^\infty(t), \quad (6.24)$$

$$f^C = f^0 \left(\frac{x - s_0(t)}{\delta} \right) + \hat{f}^0(x, t) - F_s(t), \quad (6.25)$$

$$T_g^C = T_g^0 \left(\frac{x - s_0(t)}{\delta} \right) + \hat{T}_g^0(x, t) - G_s(t). \quad (6.26)$$

The solid temperature is $O(1)$ in region CI but $O(\eta_C)$ elsewhere. We therefore construct a composite solution by setting the $O(\eta_C)$ correction in region CI to be simply η_C , so that the composite solution is accurate at leading order in all regions. As in case B, the composite solution for T_s is defined piecewise about the centre, $1 - \eta_C w(t)$, of the transition layer CIII. Thus we use the composite solution

$$T_s^C = \begin{cases} T_s^0 \left(\frac{x - s_0(t)}{\delta} \right) + \eta_C, & \text{if } x < 1 - \eta_C w(t), \\ \eta_C \bar{T}_s^0 \left(\frac{1-x}{\eta_C} \right), & \text{if } x \geq 1 - \eta_C w(t). \end{cases} \quad (6.27)$$

We have seen that case C is very similar to case B. In each, the solid is heated up from its input temperature T^{in} by heat transferred from the gas in region IV. Once it has reached the critical temperature η the chemical reaction then starts to take place, and the heat transferred from the gas to the solid in this region (II) is used primarily for this reaction, with no change in the solid temperature at leading order until it reaches the hot boundary layer (I) at $x = s$. The differences in case C are that, since the convective heat transfer from the gas is now greater, the solid material heats up much faster (over the $O(\eta_C)$ lengthscale of region CIV, rather than the $O(1)$ lengthscale of BIV), and that the reaction rate in region CII is now high enough to affect all of the solid concentration C , gas mass flux f , and gas temperature T_g at leading order. As we increase μ still further, the gas temperature must lose so much heat to the solid that it ceases to be $O(1)$. This is the situation considered in case D below.

7. Case D: $-\log(\eta) \ll \mu \ll \delta^{-1}e^{-A}$, large heat transfer

We notice that the analysis in case C above, with $\mu = O(1)$, holds so long as T_g remains $O(1)$ over the entirety of the domain. From the form (6.11) of \hat{T}_g in region CII, we see that for large enough values of the convective heat transfer coefficient μ , \hat{T}_g will decay quickly enough to become $O(\eta)$ within the domain, at which point the equations (6.7) of region II are no longer valid.

In this section we study the case $\mu \gg 1$, for which T_g becomes $O(\eta)$ within the domain. Since $\mu \gg 1$, the heat transfer between phases is fast enough that the two temperatures T_s and T_g become near equal over a short lengthscale. We find that the lengthscale over which the temperatures equilibrate in this way is $O(-\log(\eta)/\mu)$. In this section, we therefore restrict our attention to the case where the convective heat transfer coefficient μ is sufficiently large, $\mu \gg -\log(\eta) \gg 1$, that the two temperatures equilibrate over a lengthscale smaller than $O(1)$, i.e. within the domain $x \in [s, 1]$. With $\mu \gg 1$, the solid temperature scaling (3.2), is denoted η_D , and we note $\eta_D > \eta_C > \eta_B$. We also require that $\mu \ll \delta^{-1}e^{-A}$, so that $\eta_D \ll 1$. This ensures that the asymptotic expansion in powers of η_D remains valid. Although not strictly a distinguished limit of the problem, it is interesting to study this regime $-\log(\eta_D) \ll \mu \ll \delta^{-1}e^{-A}$ in order to understand how the solution structure evolves as μ increases from $O(1)$ in case C to the distinguished limit $\mu = O(\delta^{-1})$, which we study in case E below. Specifically, all of the chemical reaction in case D occurs in a (wide, $O(-\log(\eta)/\mu)$) boundary layer about the free boundary $x = s$, whereas in case C the chemical reaction occurred throughout the entire $O(1)$ domain (except in a heating boundary layer located at $x = 1$). This is because the heat transfer between phases now occurs much faster. (In case E, with the inter-phase heat transfer faster still, we will see that the reaction regions are confined to an even narrower region around $x = s$.)

We will not study the case $1 \ll \mu \ll -\log(\eta_D)$, since this limit has the same structure of case C, as we will show below. We also do not deal fully with the distinguished limit $\mu = O(-\log(\eta_D))$, since there are a plethora of subcases for the asymptotic structure in this case, depending on whether the two temperatures equilibrate over the domain or not, and how close the point at which they equilibrate is to the boundary $x = 1$ of the domain. We discuss some of these possible subcases in more detail in the discussion below.

Although in cases C (above) and E (below) we find time-dependent solutions, in case D we restrict our attention to the steady-state case, for simplicity. We note, however, that time-dependent solutions in case D are likely to have the same structure as those we later discuss in cases E and F, below. We find that there are two separate steady-state behaviours in the regime $-\log(\eta_D) \ll \mu \ll \delta^{-1}e^{-A}$, depending on the model parameters. Specifically, in case Da we suppose $Kf < 1$ near $x = 1$, so that the heat flux in the gas is smaller in

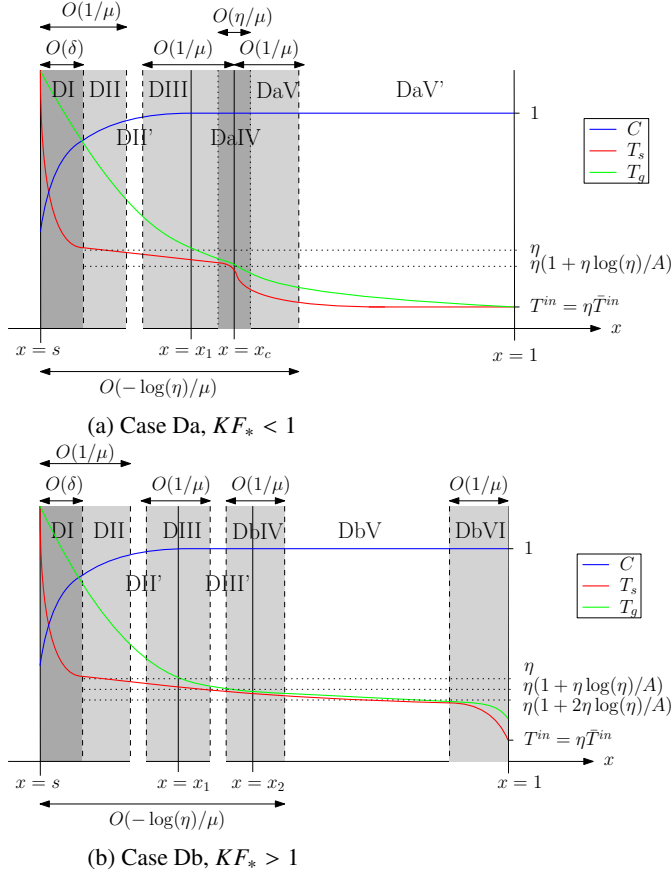


Figure 7: Schematics of the steady-state solution structures in case D: $\mu = O(1)$.

838 magnitude than the heat flux in the solid in the opposite direction. In case Db we consider the
 839 opposite case, in which $Kf > 1$ near $x = 1$. The schematics illustrating the solution structure
 840 in these two steady-state cases Da and Db are shown in figure 7, and the changes of variable
 841 for each region are summarised in table 4.

842 7.1. Behaviour common to cases Da and Db

843 There are several regions of the domain near to the free boundary $x = s$ where the behaviour
 844 is the same for both cases Da and Db.

845 7.1.1. Region DI

846 As usual we find a reaction boundary layer, region DI, of width $O(\delta)$ at $x = s$, within which
 847 the heat for the reaction is provided by the radiation onto the free boundary. Expanding the
 848 dependent variables in powers of η_D , by setting

$$849 \quad T_s = T_s^0(X) + \eta_D T_s^1(X) + O(\eta_D^2), \quad C = C^0(X) + \eta_D C^1(X) + O(\eta_D^2), \quad (7.1a)$$

$$850 \quad T_g = T_g^0(X) + \eta_D T_g^1(X) + O(\eta_D^2), \quad f = f^0(X) + \eta_D f^1(X) + O(\eta_D^2), \quad (7.1b)$$

$$851 \quad s = s_0 + \eta_D s_1 + O(\eta_D^2), \quad (7.1c)$$

Region	Spatial Variable	Size of Q	Dominant terms in (3.1)	Dependent Variables
DI	$x = s + \delta X$	$Q = O(1)$	1, 2, 5	C, f, T_s, T_g
DII & DII'	$x = s + y/\mu$	$Q = O(\delta\mu)$,	3, 5	$C = \hat{C}, f = \hat{f},$ $T_s = \eta_D(1 + \eta_D \hat{T}_s), T_g = \hat{T}_g$
DIII & DIII'	$x = x_1 + z/\mu$	$Q = O(\delta\mu\eta_D)$	3, 4, 5	$C = \mathcal{C}, f = \mathcal{F}, T_g = \eta_D \mathcal{T}_g$ $T_s = \eta_D(1 + \eta_D \log(\eta_D)/A + \eta_D \mathcal{T}_s),$
DaIV	$x = x_c + \eta_D Y/\mu$	$Q = O(\delta\mu\eta_D)$	1, 3, 4, 5	$C = \tilde{C}, f = \tilde{f}, T_g = \eta_D \tilde{T}_g,$ $T_s = \eta_D(1 + \eta_D \log(\eta_D)/A + \eta_D \tilde{T}_s),$
DaV	$x = x_c + Z/\mu$ ($Z > 0$)	$Q \ll \delta\mu\eta_D$	1, 3, 4	$C = \bar{C}, f = \bar{f},$ $T_s = \eta_D \bar{T}_s, T_g = \eta_D \bar{T}_g$
DaV'	x	$Q \ll \delta\mu\eta_D$	1	-
DbIV	$x = x_2 + Z/\mu$	$Q = O(\delta\mu\eta_D^2)$	1, 3, 4, 5	$C = \tilde{C}, f = \tilde{f},$ $T_g = \eta_D(1 + 2\eta_D \log(\eta_D)/A + \eta_D \tau_g),$ $T_s = \eta_D(1 + 2\eta_D \log(\eta_D)/A + \eta_D \tau_s),$
DbV	x	$Q \ll \delta\mu\eta_D^2$	1	-
DbVI	$x = 1 + Z/\mu$	$Q \ll \delta\mu\eta_D^2$	1, 3, 4	$C = \bar{C}, f = \bar{f},$ $T_s = \eta_D \bar{T}_s, T_g = \eta_D \bar{T}_g$

Table 4: Summary of the asymptotic regions of the domain, and the changes of variable in these regions, for the steady-state cases D (a and b): $-\log(\eta_D) \ll \mu \ll \delta^{-1}$.

we obtain the same equations (4.8a)–(4.8c) at leading order since $\mu \ll \delta^{-1}$ (although with $\dot{s}_0 = 0$, since we restrict to steady state). The far-field solid concentration must satisfy (6.3) as in case C, where C^∞ is yet to be determined by matching with the outer problem.

7.1.2. Region DII

Outside region DI, we require $T_s \sim \eta_D$, in order to balance the terms 3 and 5 in the solid heat equation (3.1). However, since then $Q = O(\mu) \gg 1$, this region, which we denote region DII, must have a shorter lengthscale than $O(1)$ in order to obtain a balance in the gas temperature equation. In this region the heat for the reaction is provided by the heat transfer between phases. Region DII is therefore a second, wider boundary layer, width $O(\mu^{-1})$, about $x = s_0$, and so we make the change of variables $x = s_0 + y/\mu$. We look for a solution

$$T_s = \eta_D (1 + \eta_D \hat{T}_s), \quad (7.2)$$

and we also use the notation $C = \hat{C}$, $f = \hat{f}$, and $T_g = \hat{T}_g$ in region DII for clarity. We expand in powers of $\eta_D \ll 1$, setting

$$\begin{aligned} \hat{T}_s &= \hat{T}_s^0(y) + O(\eta_D), & \hat{C} &= \hat{C}^0(y) + O(\eta_D), \\ \hat{T}_g &= \hat{T}_g^0(y) + O(\eta_D), & \hat{f} &= \hat{f}^0(y) + O(\eta_D). \end{aligned} \quad (7.3)$$

Substituting into (2.12a)–(2.12d), we find that at leading order

$$-\frac{d\hat{C}^0}{dy} = -\hat{C}^0 \exp\left(A\left(1 + \hat{T}_s^0\right)\right), \quad \hat{T}_g^0 = \gamma \hat{C}^0 \exp\left(A\left(1 + \hat{T}_s^0\right)\right), \quad (7.4a)$$

$$\frac{d\hat{f}^0}{dy} = \hat{C}^0 \exp\left(A\left(1 + \hat{T}_s^0\right)\right), \quad K \frac{d}{dy}(\hat{f}^0 \hat{T}_g^0) = -\hat{T}_g^0. \quad (7.4b)$$

871 Precisely as in (6.11) for region CII of case C, we find the solutions

$$872 \quad \hat{T}_g^0 = -\frac{\gamma W(a_D)}{K(1+W(a_D))}, \quad \hat{f}^0 = \frac{F_s(\gamma + KG_s)}{\gamma + K\hat{T}_g^0}, \quad (7.5)$$

873 of equations (7.4b), where

$$874 \quad a_D = -\frac{KG_s}{\gamma + KG_s} \exp\left(-\frac{1}{\gamma + KG_s} \left(\frac{\gamma}{KF_s} y + KG_s\right)\right), \quad (7.6)$$

875 and the matching constants F_s and G_s are as defined in (6.4) (with $\dot{s}_0 = 0$, since we are in
876 steady state). The leading-order solid concentration therefore satisfies

$$877 \quad -\frac{d\hat{C}^0}{dy} = \frac{W(a_D)}{K(1+W(a_D))}, \quad (7.7)$$

878 along with $\hat{C}^0 = C^\infty$ at $y = 0$, and a matching condition to the right, as y becomes large. We
879 will find below that C is uniform to leading order in all regions to the right of region DII, in
880 both cases Da and Db. Thus the matching condition is $\hat{C}^0 \rightarrow 1$ as $y \rightarrow \infty$. From (7.5) we
881 see that $\hat{T}_g^0 \rightarrow 0$ as $y \rightarrow \infty$, and so the solution of (7.7) is

$$882 \quad \hat{C}^0 = 1 - \frac{KF_s(\gamma + KG_s)\hat{T}_g^0}{\gamma(\gamma + K\hat{T}_g^0)}. \quad (7.8)$$

883 Applying the boundary conditions at $y = 0$, where $\hat{T}_g^0 = G_s$, we therefore fix the value of C^∞
884 to be

$$885 \quad C^\infty = 1 - \frac{KF_s G_s}{\gamma}. \quad (7.9)$$

886 Having found \hat{T}_g^0 and \hat{C}^0 , the solid temperature variation, given by (7.4a) (right), is then

$$887 \quad \begin{aligned} 888 \quad \hat{T}_s^0 &= \frac{1}{A} \log\left(\frac{\hat{T}_g^0}{\gamma\hat{C}^0}\right) - 1 \\ 889 \quad &= -1 - \frac{1}{A} \log\left(K(1+W(a_D))\left(\frac{1}{-W(a_D)} - \frac{F_s(\gamma + KG_s)}{\gamma}\right)\right). \end{aligned} \quad (7.10)$$

890 We note that this region DII is exactly analogous to region CII in case C with $\mu = O(1)$,
891 except that since the convective heat transfer coefficient μ is now larger, the decay length of
892 \hat{T}_g^0 is shorter. We see that the equations (7.4) hold until \hat{T}_g^0 becomes order η_D , at which point
893 term 4 must enter the dominant balance of equation (3.1). Since for small a_D , $W(a_D) \sim a_D$,
894 we see that $\hat{T}_g^0 \sim \eta_D$ when $-\gamma a_D/K = \eta_D$, which occurs at the point $y = y_*$, defined by
895 $\gamma a_D(y_*)/K = \eta_D$. Rearranging, this gives

$$896 \quad y_* = \frac{1}{\gamma} KF_s(\gamma + KG_s) \left(-\log(\eta_D) + \log\left(\frac{\gamma G_s}{\gamma + KG_s}\right) - \frac{KG_s}{\gamma + KG_s}\right). \quad (7.11)$$

897 We see that point $y_* = O(-\log(\eta_D))$ is large. As y becomes larger than $O(1)$, we strictly
898 leave region DII, and enter region DII', an extension of DII, within which the lengthscale is
899 $O(-\log(\eta_D)/\mu)$. The dominant physical processes in region DII' (heat transfer from gas to
900 solid, which provides energy for the chemical reaction) are the same as in region DII, except
901 that f is uniform at leading order, and thus T_g is exponentially decaying.

902 In the original variables, the point y_* is at $x_1 := s_0 + y_*/\mu$. As mentioned at the start of
903 this section, we notice that if $1 \ll \mu \ll -\log(\eta_D)$ then $x_1 - s_0 \gg 1$ and so we revert to

a structure like case C, since \hat{T}_g remains $O(1)$ throughout the domain. Conversely, in the regime $-\log(\eta_D) \ll \mu$ studied in this section, we have $x_1 - s_0 \ll 1$ and so \hat{T}_g^0 becomes small within the domain. In the distinguished limit $\mu = O(-\log(\eta_D))$, we see that $x_1 - s_0 = O(1)$, and we may be in either of these cases, or instead have x_1 close to 1, for which a number of additional subcases arise.

7.1.3. Region DIII

With $\mu \gg -\log(\eta_D)$, the point x_1 is an $O(-\log(\eta_D)/\mu) \ll 1$ distance from s_0 (and so is definitely contained within the domain). Around this point x_1 , there must be an $O(\mu^{-1})$ transition layer, denoted region DIII, in which term 4 enters the dominant balance in (3.1). In this region we use the change of spatial variables $x = x_1 + z/\mu$. Since now $T_g = O(\eta_D)$, the balance of terms 3 and 5 requires that term 5, the chemical reaction rate, be $O(\delta\mu\eta_D)$. Heat transfer between the two phases is slower than in regions DII-DII' since the difference between the two temperatures is now smaller, and so the chemical reaction driven by this temperature difference is slower in this region than in region DII and DII'. Thus, the solid temperature must be of the form

$$T_s = \eta_D \left(1 + \frac{\eta_D \log(\eta_D)}{A} + \eta_D \mathcal{T}_s \right). \quad (7.12)$$

We also use the change of variables $T_g = \eta_D \mathcal{T}_g$ in region DIII, and set $f = \mathcal{F}$, $C = C$ for clarity of notation, and we expand in powers of η_D , setting

$$\begin{aligned} \mathcal{T}_s &= \mathcal{T}_s^0(z) + O(\eta_D), & C &= C^0(z) + O(\eta_D), \\ \mathcal{T}_g &= \mathcal{T}_g^0(z) + O(\eta_D), & \mathcal{F} &= \mathcal{F}^0(z) + O(\eta_D). \end{aligned} \quad (7.13)$$

At leading order in (2.12a) and (2.12b), we find that both C^0 and \mathcal{F}^0 are uniform in region DIII. This is because the chemical reaction rate is now $Q = O(\delta\eta_D\mu)$, and so there is only an $O(\eta_D)$ mass consumption over region DIII. Indeed, we will find that in all regions to the right of region DIII (in either case Da or Db), C and f are uniform up to $O(\eta_D)$. Thus by matching to the right we will find that $C^0 = 1$, and matching at leading order with region DII, we have

$$\mathcal{F}^0 = F_* := \frac{F_s(\gamma + KG_s)}{\gamma} = \hat{f}^0|_{y=y_*} + O(\eta_D). \quad (7.14)$$

At leading order, the heat equations (2.12c) and (2.12d) for \mathcal{T}_s^0 and \mathcal{T}_g^0 become

$$\mathcal{T}_g^0 - \left(1 + \eta_D \frac{\log(\eta_D)}{A} \right) = \gamma \exp \left(A \left(1 + \mathcal{T}_s^0 \right) \right), \quad (7.15)$$

$$KF_* \frac{d\mathcal{T}_g^0}{dz} = -\mathcal{T}_g^0 + \left(1 + \eta_D \frac{\log(\eta_D)}{A} \right). \quad (7.16)$$

Here we have included the $O(-\eta_D \log(\eta_D))$ terms, since these are larger than the next order η_D , and we can find an explicit solution taking both $O(1)$ and $O(-\eta_D \log(\eta_D))$ terms into account together. The ODE (7.16) for \mathcal{T}_g^0 has the general solution

$$\mathcal{T}_g^0 = 1 + \eta_D \frac{\log(\eta_D)}{A} + \exp \left(-\frac{1}{KF_*} z \right), \quad (7.17)$$

where we have fixed the constant of integration by matching with region DII. Finally, from (7.15) we compute

$$\mathcal{T}_s^0 = -\frac{1}{A} \left(\log(\gamma) + \frac{1}{KF_*} z \right) - 1, \quad (7.18)$$

completing the analysis in region DIII.

7.1.4. Region DaV and DbVI

Regions DI–DIII as described above are common to both cases Da and Db; these are all reaction regions, with the chemical reaction playing a dominant role. We now pause in our analysis moving left to right through the domain, and instead investigate the behaviour near the $x = 1$ boundary, where there is negligible chemical reaction. We will find different behaviour for the cases Da and Db, depending on whether the overall heat flux $Kf - 1 = KF_* - 1 + O(\eta_D)$ is negative or positive, respectively.

On the right side of the domain, the solid temperature must decrease from close to η_D at the left of the domain to the input value $T^{\text{in}} = \eta_D \bar{T}^{\text{in}}$. (As in regions BIV and CIV, here the heat transferred from the gas to the solid is used to heat the solid material from its input temperature, T^{in}). We therefore rescale

$$T_s = \eta_D \bar{T}_s \quad \text{and} \quad T_g = \eta_D \bar{T}_g, \quad (7.19)$$

noting that T_g must be $O(\eta_D)$ in this region too because it is $O(\eta_D)$ in region DIII, and can only decrease through the rest of the domain. With $\bar{T}_s < 1 + \eta_D \log(\eta_D)/A$, we notice that the chemical reaction rate $\bar{Q} \ll \delta\mu\eta_D$ is small. In order to balance the heat advection with heat transfer between phases in the gas heat equation, we must scale the space variable to an $O(1/\mu)$ domain. Thus the region over which T_s changes must be a boundary layer. We make the change of variables $x = x_c + Z/\mu$, where $Z = O(1)$, and x_c (the position of this boundary layer) is an order 1 point in the domain, to be determined. As well as (7.19), we set $f = \bar{f}$ and $C = \bar{C}$ in this region for clarity of notation, but note that since $\bar{Q} \ll \delta\mu\eta_D$ is small, $\bar{C} = 1 + O(\eta_D)$ and $\bar{f}^0 = F_* + O(\eta_D)$ are uniform over this region at leading order, fixed by matching with regions to the right and left, respectively. We expand the temperatures in powers of η_D , by setting

$$\bar{T}_s = \bar{T}_s^0(Z) + O(\eta_D), \quad \bar{T}_g = \bar{T}_g^0(Z) + O(\eta_D). \quad (7.20)$$

At leading order in (2.12c) and (2.12d), we therefore find

$$-\frac{d\bar{T}_s^0}{dZ} = \bar{T}_g^0 - \bar{T}_s^0, \quad KF_* \frac{d\bar{T}_g^0}{dZ} = -\bar{T}_g^0 + \bar{T}_s^0, \quad (7.21)$$

which admit a general solution

$$\bar{T}_s^0 = b_1 + KF_* b_2 \exp\left(\frac{KF_* - 1}{KF_*} Z\right), \quad \bar{T}_g^0 = b_1 + b_2 \exp\left(\frac{KF_* - 1}{KF_*} Z\right), \quad (7.22)$$

where b_1 and b_2 are constants to be determined. We notice that the position of the boundary layer, x_c , must depend on the sign of $KF_* - 1$, and we consider the cases Da ($KF_* < 1$) and Db ($KF_* > 1$) separately below. In case Da with $KF_* < 1$, we find that this boundary layer must be at the left side of the domain (region DaV), whereas in case Db with $KF_* > 1$, we must take $x_c = 1$ so that the boundary layer is region DbVI, on the right side of the domain. From the nondimensionalisation, we see that

$$KF_* < 1 \quad \text{if} \quad c_{p,g}f < c_{p,s}u_s C_s, \quad (7.23)$$

and vice versa. Thus, since both phases have the same temperature at leading order on an

983 $O(1)$ lengthscale, we are comparing the heat flux in the gas (left-to-right) with that in the
 984 solid (right-to-left).

985 7.2. Case $Da: KF_* < 1$

986 If $KF_* < 1$, then the heat flux in the solid is greater than that in the gas, and so the overall
 987 heat transport is right-to-left.

988 7.2.1. Region DaV

989 From the form of the solution (7.22), we require that x_c is on the left side of the domain, so
 990 that the solution remains bounded as $Z \rightarrow \infty$ and we leave the boundary layer. This boundary
 991 layer is denoted region DaV in figure 7.

992 As $Z \rightarrow \infty$, we have $\bar{T}_s^0, \bar{T}_g^0 \rightarrow b_1$, so in this case we must take $b_1 = \bar{T}^{\text{in}}$, in order to satisfy
 993 the boundary condition at $x = 1$. The value of b_2 is fixed by matching at $Z = 0$, or $x = x_c$.
 994 We notice that the difference in solutions at $Z = 0$ is

$$995 \left(\bar{T}_g^0 - \bar{T}_s^0 \right) \Big|_{Z=0} = (1 - KF_*)b_2 = O(1), \quad (7.24)$$

996 thus $T_g - T_s = O(\eta_D)$ at $Z = 0$. We must therefore have x_c within the $O(1/\mu)$ transition
 997 layer DIII about x_1 , in which $T_g - T_s = O(\eta_D)$. Since $T_s = \eta_D(1 + \eta_D \log(\eta_D)/A) + O(\eta_D^2)$
 998 (by (7.12)) throughout region DIII, we fix b_2 to be

$$999 b_2 = \frac{1}{KF_*} \left(1 + \eta_D \frac{\log(\eta_D)}{A} - \bar{T}^{\text{in}} \right). \quad (7.25)$$

1000 Thus the solutions (7.22) in this boundary layer region DaV (to the right of $x = x_c$) are

$$1001 \bar{T}_s^0 = \bar{T}^{\text{in}} + \left(1 + \eta_D \frac{\log(\eta_D)}{A} - \bar{T}^{\text{in}} \right) \exp \left(-\frac{1 - KF_*}{KF_*} Z \right), \quad (7.26a)$$

$$1002 \bar{T}_g^0 = \bar{T}^{\text{in}} + \frac{1}{KF_*} \left(1 + \eta_D \frac{\log(\eta_D)}{A} - \bar{T}^{\text{in}} \right) \exp \left(-\frac{1 - KF_*}{KF_*} Z \right). \quad (7.26b)$$

1004 At $x = x_c$, or $Z = 0$, we have $\bar{T}_g^0 = (1 + \eta_D \log(\eta_D)/A)/(KF_*)$. Imposing continuity of T_g at
 1005 $x = x_c$ determines the position of x_c within region DIII, i.e., x_c is the point at which

$$1006 \mathcal{T}_g^0 = \frac{1 + \eta_D \log(\eta_D)/A}{KF_*}. \quad (7.27)$$

1007 Using the form of \mathcal{T}_g^0 given by (7.17), we find that

$$1008 x_c = x_1 + \frac{1}{\mu} KF_* \log \left(\frac{1}{(1 - KF_*)(1 + \eta_D \log(\eta_D)/A)} \right). \quad (7.28)$$

1009 7.2.2. Region DaIV

1010 In order to match between the $O(1/\mu)$ regions DIII and DaV on either side of x_c , we must
 1011 introduce a narrower transition layer of width $O(\eta_D/\mu)$ at $x = x_c$, which we refer to as region
 1012 DaIV. This region is entirely analogous to regions BIII and CIII, in that its only function is
 1013 to smooth the transition between neighbouring regions. Exactly as in those cases we see that
 1014 all of f , C , and T_g are uniform to leading order over this region (although, unlike cases B and
 1015 C, T_g is now $O(\eta_D)$), and we are left with a single ODE for the solid temperature variation.
 1016 The changes of variable for this analysis are given in table 4.

1017 To the right of region DaV is region DaV', filling the remainder of the domain. This
 1018 is an extension of region DaV, in which all variables are uniform at leading order, with
 1019 $C = 1 + O(\eta_D)$, $f = F_* + O(\eta_D)$, $T_s = \eta_D \bar{T}^{\text{in}} + O(\eta_D^2)$, and $T_g = T_s + O(\eta_D^2)$.

7.2.3. Composite solution

We can form a leading-order, composite, steady-state solution as follows. Since $C = 1$ at leading order in regions DIII–DaV, the leading-order composite solution is simply

$$C^{\text{Da}} = C^0 \left(\frac{x - s_0}{\delta} \right) + \hat{C}^0(\mu(x - s_0)) - C^\infty. \quad (7.29)$$

The gas temperature is $O(1)$ in regions DI and DII, but $O(\eta_D)$ in regions DIII–DaV. Since we have not computed the $O(\eta_D)$ correction in regions DI–DII, we assume that this correction is $\eta_D(1 + \eta_D \log(\eta_D)/A)$ so that the composite solution is correct to $O(\eta_D)$ in regions DIII–DaV. The composite solution is defined piecewise on either side of the transition layer DaIV. The centre of this transition layer is x_c , given by (7.28), which is defined so that there is a continuous transition between $T_s = \eta_D \mathcal{T}_g^0$ in region DIII and $T_s = \eta_D \bar{T}_g$ in region DaV. For the composite solution, we choose to define a slightly different changeover point $x_c^* = x_c + O(\eta_D/\mu)$, so that the composite solution is continuous at this point. We therefore use

$$T_g^{\text{Da}} = \begin{cases} T_g^0 \left(\frac{x - s_0}{\delta} \right) + \hat{T}_g^0(\mu(x - s_0)) - G_s \\ \quad + \eta_D \mathcal{T}_g^0(\mu(x - x_1)) - \exp \left(-\frac{\mu}{KF_*} (x - x_1) \right), & \text{if } x < x_c^*, \\ \eta_D \bar{T}_g^0(\mu(x - x_c)), & \text{if } x > x_c^*, \end{cases} \quad (7.30)$$

which, from the form of \mathcal{T}_g^0 in (7.17), simplifies to

$$T_g^{\text{Da}} = \begin{cases} T_g^0 \left(\frac{x - s_0}{\delta} \right) + \hat{T}_g^0(\mu(x - s_0)) - G_s + \eta_D \left(1 + \eta_D \frac{\log(\eta_D)}{A} \right), & \text{if } x < x_c^*, \\ \eta_D \bar{T}_g^0(\mu(x - x_c)), & \text{if } x > x_c^*. \end{cases} \quad (7.31)$$

The solid temperature is similarly $O(1)$ in region DI, but $O(\eta_D)$ everywhere else. As in previous cases, we set the $O(\eta_D)$ correction in region DI to be $\eta_D(1 + \eta_D \log(\eta_D)/A)$ so that the composite solution is accurate to $O(\eta_D)$ in regions DII–DaV. We neglect the $O(\eta_D^2)$ corrections in regions DII and DIII for this composite solution. We form the leading-order composite solution:

$$T_s^{\text{Da}} = \begin{cases} T_s^0 \left(\frac{x - s_0}{\delta} \right) + \eta_D \left(1 + \eta_D \frac{\log(\eta_D)}{A} \right), & \text{if } x < x_c, \\ \eta_D \bar{T}_s^0(\mu(x - x_c)), & \text{if } x > x_c. \end{cases} \quad (7.32)$$

7.3. Case Db: $KF_* > 1$

In the case $KF_* > 1$, the heat flux in the gas is greater than in the solid. We therefore require the position of the boundary layer over which T_s decays to T_s^{in} to be at the far right of the domain, at $x_c = 1$. This is so that the variable $Z < 0$, and the solution (7.22) is bounded as we leave the boundary layer ($Z \rightarrow -\infty$). This boundary layer is therefore region DbVI in figure 7.

In this case, we notice that as $Z \rightarrow -\infty$, both $\bar{T}_s^0, \bar{T}_g^0 \rightarrow b_1$, so that far from $x = 1$, we have $T_g - T_s = O(\eta_D^2)$. In region DIII, we have $T_g - T_s = O(\eta_D)$. We therefore cannot match directly with region DIII: there must be another region within which $T_s - T_g = O(\eta_D^2)$. We denote this region DbIV.

7.3.1. Region DbIV

We note that the analysis of region DIII holds so long as $T_g - T_s \gg \eta_D^2$. As T_g is decaying through region DIII, $T_g - T_s$ is decreasing. At the point where $T_g - T_s = O(\eta_D^2)$, the advection (term 1 in (3.1)) must also enter the dominant balance. From (7.17), we see

1058 that $T_g - T_s = \eta_D^2$ when

$$1059 \quad \exp\left(-\frac{1}{KF_*}z\right) = \eta_D, \quad (7.33)$$

1060 i.e., at the point

$$1061 \quad z_* = -KF_* \log(\eta_D). \quad (7.34)$$

1062 Like y_* given by (7.11), we note that $z_* = O(-\log(\eta_D))$ is large. Strictly speaking, there is
 1063 therefore another region DbIII' with lengthscale $O(-\log(\eta_D)/\mu)$ to the right of region DIII,
 1064 but since this is a subregion of region DIII (the same equations hold, simply over a longer
 1065 lengthscale), we do not analyse this region separately. Although z_* is large, in the original
 1066 variables, this is the point $x_2 := s_0 + (y_* + z_*)/\mu \ll 1$, since $\mu \gg -\log(\eta_D)$. Thus x_2 remains
 1067 within the $O(-\log(\eta_D)/\mu)$ boundary layer around $x = s_0$.

1068 Region DbIV is the transition layer around the point x_2 , in which all the terms 1, 3, 4, and
 1069 5 balance in the solid heat equation (3.1). Since $T_g - T_s = O(\eta_D^2)$ in region DbIV, we make
 1070 the change of variables

$$1071 \quad T_s = \eta_D \left(1 + 2\eta_D \frac{\log(\eta_D)}{A} + \eta_D \frac{\tau_s}{A}\right), \quad T_g = \eta_D \left(1 + 2\eta_D \frac{\log(\eta_D)}{A} + \eta_D \frac{\tau_g}{A}\right), \quad (7.35)$$

1073 so that at leading order both T_s and T_g are uniform through region DbIV. The heat exchange
 1074 terms (3 and 4) now combine to be $O(\mu\eta_D^2)$, and the heat lost to the chemical reaction (term
 1075 5) is likewise $O(\mu\eta_D^2)$, since

$$1076 \quad Q(C, T_s) = \delta\mu \left(\eta_D^2 C e^{A+\tau_s} + O\left(\eta_D^3\right)\right). \quad (7.36)$$

1077 As in regions DII and DIII, we require an $O(1/\mu)$ lengthscale to balance advection and heat
 1078 transfer terms in the gas heat equation, and so we make the change of variables $x = x_2 + Z/\mu$.
 1079 As in region DIII, we note that since the reaction rate is small, $C = 1 + O(\eta_D)$, $f = F_* + O(\eta_D)$
 1080 are uniform at leading order throughout this region. Expanding in powers of η_D , taking

$$1081 \quad \tau_s = \tau_s^0(Z) + O(\eta_D), \quad \tau_g = \tau_g^0(Z) + O(\eta_D), \quad (7.37)$$

1083 we find that at leading order (2.12c) and (2.12d) become

$$1084 \quad -\frac{d\tau_s^0}{dZ} = (\tau_g^0 - \tau_s^0) - \gamma A e^{A+\tau_s^0}, \quad KF_* \frac{d\tau_g^0}{dZ} = -(\tau_g^0 - \tau_s^0). \quad (7.38)$$

1086 This transition region DbIV plays the same role as regions BIII, CIII, and DaIV, in cases
 1087 B, C, and Da, respectively. It is in this region that term 1 enters the dominant balance of
 1088 (3.1), while term 5 leaves the dominant balance. However, while T_g is uniform at leading
 1089 order over the transition region DbIV, we must solve for the variation, τ_g^0 , simultaneously
 1090 with the solid temperature variation, τ_s^0 , via the coupled system (7.38), rather than solving a
 1091 single ODE for the solid temperature variation, as we did in regions BIII, CIII, and DaIV.

1092 While we cannot solve the system (7.38) explicitly, we can study solutions using a phase-
 1093 plane analysis. We first rescale $\tilde{Z} = KF_* Z$ so that the system (7.38) becomes

$$1094 \quad \frac{d\tau_s^0}{d\tilde{Z}} = -c_1(\tau_g^0 - \tau_s^0) + c_2 e^{\tau_s^0}, \quad \frac{d\tau_g^0}{d\tilde{Z}} = -(\tau_g^0 - \tau_s^0). \quad (7.39)$$

1096 in terms of the two parameters $c_1 = KF_*$ and $c_2 = KF_* \gamma A e^A$. Solutions of this system (7.39)
 1097 are shown as trajectories in the phase-plane diagram in figure 8. The black lines shown in

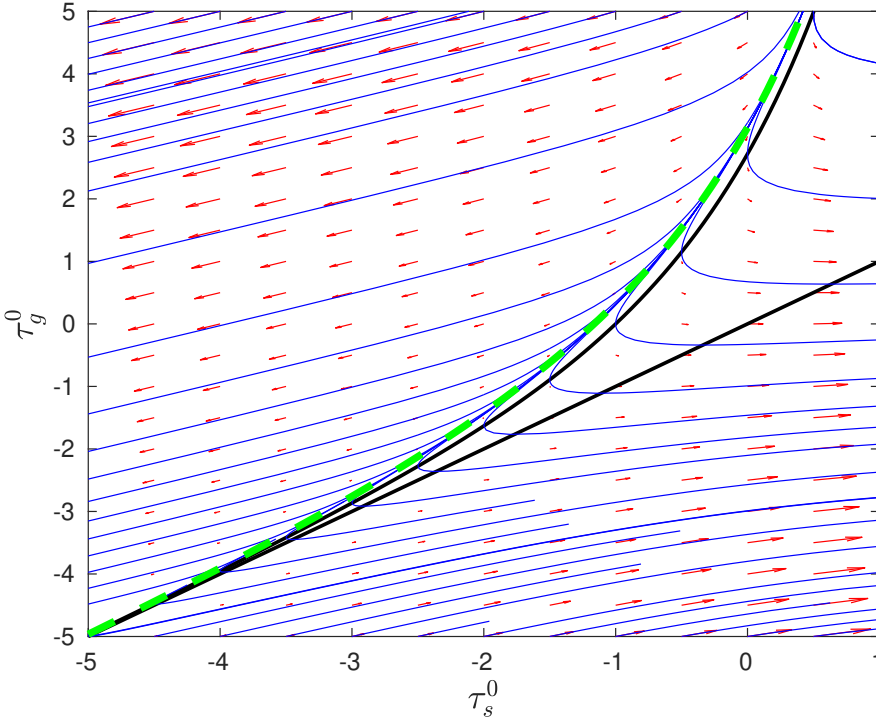


Figure 8: Phase plane for the steady-state system (7.39). Nullclines are in black and trajectories in blue. The green dashed curve is the line $\tau_g^0 = \tau_s^{\text{limit}}(\tau_s^0)$ given by (7.42). We take physically relevant values $\gamma = A = 1$ and $KF_* = 1$, so that $c_1 = 2$, and $c_2 = 5.44$.

figure 8 are the nullclines

$$\tau_g^0 = \tau_s^0 \quad \text{and} \quad \tau_g^0 = \tau_s^0 + \frac{c_2}{c_1} e^{\tau_s^0}, \quad (7.40)$$

on which $d\tau_g/d\bar{Z} = 0$ and $d\tau_s/d\bar{Z} = 0$, respectively. As $\bar{Z} \rightarrow -\infty$, both τ_s^0 and τ_g^0 must grow exponentially, in order to match with region DIII. From the phase-plane diagram in figure 8, we see that all such trajectories follow just above the $d\tau_s^0/d\bar{Z} = 0$ nullcline as $\bar{Z} \rightarrow -\infty$. This is to be expected, since the advection term 1 must become small as $\bar{Z} \rightarrow -\infty$ in order to obtain the dominant balance between terms 3 and 5 in DIII. We observe in figure 8 that these trajectories stay just above the $d\tau_s^0/d\bar{Z} = 0$ nullcline, before either peeling away to the left, or turning the corner and crossing both nullclines, eventually approaching curves with τ_g^0 equal to a constant. In order to match to the right of region DbIV, the solution trajectory must not cross the nullclines, so that $\tau_g^0 > \tau_s^0$ everywhere, and both $\tau_g^0, \tau_s^0 \rightarrow -\infty$ as $\bar{Z} \rightarrow \infty$.

The trajectories do not cross the nullclines for any \bar{Z} , provided that the inequality

$$\frac{d\tau_g^0}{d\bar{Z}} \bigg/ \frac{d\tau_s^0}{d\bar{Z}} = \frac{d\tau_g^0}{d\tau_s^0} < \frac{d}{d\tau_s^0} \left(\tau_s^0 + \frac{c_2}{c_1} e^{\tau_s^0} \right) \quad (7.41)$$

holds at all points on the solution trajectory. Substituting in the derivatives from (7.39), we

1114 see that (7.41) reduces to the inequality

$$1115 \quad \tau_g^0 > \frac{(c_1 \tau_s^0 + c_2 e^{\tau_s^0}) \left(1 + \frac{c_2}{c_1} e^{\tau_s^0}\right) - \tau_s^0}{c_1 + c_2 e^{\tau_s^0} - 1} =: \tau_g^{\text{limit}}. \quad (7.42)$$

1116 The trajectory $\tau_g^0 = \tau_g^{\text{limit}}(\tau_s^0)$ is plotted as the dashed green curve in figure 8, and is seen to
 1117 divide the trajectories crossing the nullclines from those remaining above them. As $\tau_s^0 \rightarrow \infty$,
 1118 we have

$$1119 \quad \tau_g^{\text{limit}} \sim \tau_s^0 + \frac{c_2}{c_1} e^{\tau_s^0} + \frac{1}{c_1} + \dots. \quad (7.43)$$

1120 Therefore, as long as $\tau_g^0 > \tau_s^0 + \gamma \exp(A(1 + \tau_s^0)) + 1/c_1$ in the limit as $\bar{Z} \rightarrow -\infty$ (which
 1121 must be true from the matching with region DIII), the trajectories never cross the nullclines.

1122 We notice that, on these trajectories, τ_s^0 becomes negative as $\bar{Z} \rightarrow \infty$, and so the
 1123 exponential term in (7.39), representing the heat consumed by the chemical reaction, becomes
 1124 exponentially small in this limit. As $\bar{Z} \rightarrow \infty$, we therefore see by combining (7.39) that
 1125 $\tau_s^0 - c_1 \tau_g^0$ approaches a constant, so that the trajectories approach straight lines, as can be
 1126 seen in figure 8. We also notice that some such trajectories follow the curve $\tau_g^{\text{limit}}(\tau_s^0)$ for a
 1127 long time before peeling off to the $\tau_s^0 - c_1 \tau_g^0$ behaviour. The curve $\tau_g^{\text{limit}}(\tau_s^0)$ approaches the
 1128 nullclines as both τ_s^0 and τ_g^0 decrease below zero, and the nullclines become closer together.
 1129 Thus on these trajectories remaining close to $\tau_g^{\text{limit}}(\tau_s^0)$, both the exponential chemical reaction
 1130 term in (7.39) and the heat transfer terms $\tau_g^0 - \tau_s^0$ are very small, so that both $d\tau_g^0/d\bar{Z}$ and
 1131 $d\tau_s^0/d\bar{Z}$ are small. The solution we are concerned with must lie on one of these very slowly
 1132 moving trajectories, since $\tau_g^0 - \tau_s^0$ cannot grow until we reach the boundary layer region
 1133 DbVI. Thus the transition layer region DbIV must actually extend fully into region DbV,
 1134 which may equally be considered a subregion of either DbIV or DbVI.

1135 7.3.2. Regions DbV and DbVI

1136 To the right of region DbIV, the heat lost to the chemical reaction, term 5 in (3.1), is not
 1137 included in the dominant balance, so the system is purely advective, until the heat transfer
 1138 between phases becomes important again in region DbVI. Thus in region DbV all dependent
 1139 variables are constant at leading order, namely

$$1140 \quad T_s = T_g = \eta_D \left(1 + 2\eta_D \frac{\log(\eta_D)}{A}\right), \quad f = F_*, \quad C = 1, \quad (7.44)$$

1142 where we have fixed the constants $f = F_*$ by matching with region DbIV, and $C = 1$ by
 1143 matching with region DbVI.

1144 Using this behaviour in region DbV, we may complete our solution in region DbVI. By
 1145 matching between regions DbV and DbVI, we find $b_1 = 1 + 2\eta_D \log(\eta_D)/A$, and applying
 1146 the boundary condition $\bar{T}_s^0 = \bar{T}^{\text{in}}$ at $Z = 0$, we find

$$1147 \quad b_2 = \frac{1}{KF_*} (\bar{T}^{\text{in}} - a_1) = \frac{1}{KF_*} \left(\bar{T}^{\text{in}} - 1 - 2\eta_D \frac{\log(\eta_D)}{A} \right). \quad (7.45)$$

1148 Thus, in region DbVI,

$$1149 \quad \bar{T}_s^0 = 1 + 2\eta_D \frac{\log(\eta_D)}{A} + \left(\bar{T}^{\text{in}} - 1 - 2\eta_D \frac{\log(\eta_D)}{A} \right) \exp\left(\frac{KF_* - 1}{KF_*} Z\right), \quad (7.46)$$

$$1150 \quad \bar{T}_g^0 = 1 + 2\eta_D \frac{\log(\eta_D)}{A} + \frac{1}{KF_*} \left(\bar{T}^{\text{in}} - 1 - 2\eta_D \frac{\log(\eta_D)}{A} \right) \exp\left(\frac{KF_* - 1}{KF_*} Z\right), \quad (7.47)$$

1151

1152 completing the analysis of case Db.

1153 7.3.3. Composite solution

1154 We can therefore construct a leading-order, steady-state composite solution for case Db.
 1155 Since C and f are everywhere $O(1)$, and are constant to leading order in regions DIII–DbVI,
 1156 the composite expansions are simply

$$1157 \quad C^{\text{Db}} = C^0 \left(\frac{x - s_0}{\delta} \right) + \hat{C}^0(\mu(x - s_0)) - C^\infty, \quad (7.48)$$

$$1158 \quad f^{\text{Db}} = f^0 \left(\frac{x - s_0}{\delta} \right) + \hat{f}^0(\mu(x - s_0)) - F_s. \quad (7.49)$$

1160 Both T_s and T_g are $O(1)$ at $x = s$, but become $O(\eta_D)$ as we move further into the domain.
 1161 As in the previous cases there is freedom to choose a composite solution. Since $T_s \sim \eta_D$ is
 1162 uniform through regions DII–DbV, we use the composite solid temperature

$$1163 \quad T_s^{\text{Db}} = T_s^0 \left(\frac{x - s_0}{\delta} \right) + \eta_D \bar{T}_s^0(\mu(x - 1)), \quad (7.50)$$

1165 so that T_s is accurate with error $O(\eta_D)$ in region DI, with error $O(\eta_D^2)$ in regions DbIV–DbVI,
 1166 but with $O(\eta_D \log(\eta_D))$ error in regions DII–DbIII. Similarly, we choose the composite gas
 1167 temperature

$$1168 \quad T_g^{\text{Db}} = T_g^0 \left(\frac{x - s_0}{\delta} \right) + \hat{T}_g^0(\mu(x - s_0)) - G_s + \eta_D \bar{T}_g^0(\mu(x - 1)), \quad (7.51)$$

1170 accurate to $O(\eta_D)$ in regions DI–DII, to $O(\eta_D \log(\eta_D))$ in region DIII, and to $O(\eta_D^2)$ in
 1171 regions DbIV–DbVI.

1172 8. Case E: $\mu = O(\delta^{-1})$, large heat transfer

1173 In this section we study the behaviour of solutions of (2.12) for large convective heat transfer
 1174 rates: $\mu = O(\delta^{-1})$. We therefore change notation and write $\mu = M\delta^{-1}$, for $M = O(1)$.
 1175 We return to studying time-dependent behaviour in general, although we will highlight the
 1176 steady-state solution structures in particular.

1177 As for case D above, the heat transfer between the phases is large enough that over the
 1178 majority of the domain the solid and gas temperatures are the same. Unlike case D, however,
 1179 the two temperatures may now only differ at leading order in regions of width $O(\delta)$. In
 1180 particular, heat is transferred between phases in the conduction boundary layer, region EI, at
 1181 $x = s$. Region EI is the reaction region in this distinguished limit, and the heat for the reaction
 1182 is provided by both the radiation onto the free boundary and by the heat transferred from the
 1183 gas to the solid. Therefore, unlike in all previous cases A–D, we can no longer decouple the
 1184 gas and solid equations in region EI. In the previous cases, we used the notation F_s and G_s
 1185 given by (6.4) for the leading-order flux and temperature of gas leaving region I, respectively.
 1186 We use the different notation f^∞ and T_g^∞ for case E to highlight that the far-field forms (6.4)
 1187 no longer hold for case E.

1188 As in case D, we find that the structure of the solution outside of region EI depends on the
 1189 direction of the characteristic curves for the temperature problem. In the general unsteady
 1190 case, we must consider the gradient of these characteristic curves in relation to the speed of
 1191 the free boundary \dot{s} , leading to a variety of possible time-dependent solution structures. In
 1192 steady state, so that $\dot{s} = 0$, we find two distinct regimes for the cases where $Kf^\infty - 1$ either is
 1193 negative (which we call case Ea) or positive (case Eb). The case Da with $KF_* < 1$ is related
 1194 to the case Ea with $Kf^\infty < 1$, as μ increases, and we can similarly relate cases Db and Eb.

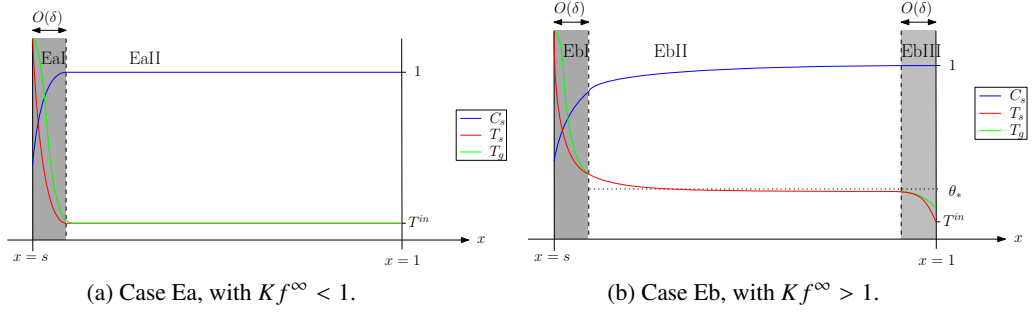


Figure 9: Schematic diagrams illustrating the asymptotic solution structures, in steady state, for case E, where $\mu = O(\delta^{-1})$. Time dependent solutions may have these, or other structures.

Region	Spatial Variable	Size of Q	Dominant terms in (3.1)	Dependent Variables
EI	$x = s + \delta X$	$Q = O(1)$	1, 2, 3, 4, 5	C, f, T_s, T_g
EaII	x	$Q \ll \delta T^{\text{in}}$	1	$C = 1, f = f^\infty,$ $T_s = T_g = T^{\text{in}}$
EbII	x	$Q = O(\delta \theta_*^2)$	1, 5	$C = 1 + \theta_*^2 \hat{C},$ $T_s = T_g = \theta_*(1 + \theta_* \hat{T})$
EbIII	$x = 1 - \delta Y$	$Q \ll \delta \theta_*^2$	1, 2, 3, 4	$C = 1, f = f^\infty,$ $T_s = \theta_* \bar{T}_s, T_g = \theta_* \bar{T}_g$

Table 5: Summary of the notation in each asymptotic region in the cases Ea ($\mu = O(\delta^{-1})$, $Kf^\infty < 1$) and Eb ($\mu = O(\delta^{-1})$, $Kf^\infty > 1$), corresponding to the diagrams in figure 9.

The structures of the two types of steady-state solution in case E are illustrated in figure 9, and the changes of variable are summarised in table 5.

8.1. Region EI

As usual we look for a boundary layer, region EI, of width $O(\delta)$ at $x = s$, setting $x = s + \delta X$. Unlike the previous cases, we now have heat transfer between the solid and gas phases on the $O(\delta)$ lengthscale, and so the solid and gas equations in region EI do not decouple. At leading order in δ , the equations in region EI are quasi-steady, so that we have $f = f_* + (1 + \dot{s})(C - C_*) + O(\delta)$ here. To leading order in δ , the equations for C , T_s , and T_g are

$$-(1 + \dot{s}) \frac{\partial C}{\partial X} = -C \exp \left(A \left(1 - \frac{1}{T_s} \right) \right), \quad (8.1a)$$

$$-(1 + \dot{s}) C \frac{\partial T_s}{\partial X} = \frac{\partial^2 T_s}{\partial X^2} + M(T_g - T_s) - \gamma C \exp \left(A \left(1 - \frac{1}{T_s} \right) \right), \quad (8.1b)$$

$$K \frac{\partial}{\partial X} (f T_g) = T_s C \exp \left(A \left(1 - \frac{1}{T_s} \right) \right) - M(T_g - T_s), \quad (8.1c)$$

1207 with boundary conditions

$$1208 \quad C = C_*, \quad T_s = T_g = \frac{\rho}{s} \quad \text{at } X = 0. \quad (8.1d)$$

1210 As in cases A–D, we will see (in Section 8.2 below) that the main source of error in our
 1211 approximation in this region EI is the switchback error due to the non-zero temperatures in
 1212 region EII. Thus, although we have only neglected terms of order δ in (8.1), the error in the
 1213 solution is in fact greater than $O(\delta)$. We note that all the physical processes come into the
 1214 dominant balance in this boundary layer EI, except for the time derivatives. Like the region-I
 1215 problem in cases A–D, (8.1) is quasi-steady.

1216 The system (8.1) is closed by applying appropriate matching conditions as $X \rightarrow \infty$, but
 1217 it is not immediately clear what the correct conditions are. In the far field, as $X \rightarrow \infty$, we
 1218 require that the chemical reaction rate becomes small in order that the rate of change of C
 1219 becomes small. This means we expect T_s to be small as we leave the boundary layer. Using
 1220 the far-field conditions

$$1221 \quad T_s \rightarrow 0, \quad C \rightarrow C^\infty(t) \quad \text{as } X \rightarrow \infty, \quad (8.2)$$

1223 as in cases C and D, where $C^\infty(t)$ is to be determined, the system (8.1) may be shown to be
 1224 correctly specified so long as

$$1225 \quad K(f_* + (1 + \dot{s})(C^\infty - C_*)) < (1 + \dot{s})C^\infty, \quad (8.3)$$

1226 where, as always, s is found as part of the solution of the region-I problem. Since \dot{s} and C^∞
 1227 are functions of time, we note that (8.3) may hold for certain times, and not others. This
 1228 condition (8.3) is precisely the requirement that, in the far-field of the moving boundary layer
 1229 EI, the heat flux left-to-right in the gas is less than the heat flux right-to-left in the solid.
 1230 Thus the far-field conditions (8.2) can only be imposed if the overall direction of heat flow is
 1231 right-to-left within the moving boundary layer, i.e., *into* the boundary layer. In this case, we
 1232 note that the conditions (8.2) ensure that $T_g \rightarrow 0$ as $X \rightarrow 0$ also, and so $T_s - T_g \rightarrow 0$ in the
 1233 far-field limit.

1234 We restrict to the case $K < 1$, i.e., $c_{p,g} < c_{p,s}$, which we expect to be physically relevant
 1235 in general (and is certainly relevant for the silicon furnace (Luckins *et al.* 2021)). In this case
 1236 we note that

$$1237 \quad C^\infty - K(C^\infty - C_*) = C^\infty(1 - K) + KC_* > 0 \quad (8.4)$$

1238 is positive. The inequality (8.3) may therefore be rearranged to

$$1239 \quad \dot{s} > -1 + \frac{Kf_*}{C^\infty - K(C^\infty - C_*)} =: U(C^\infty). \quad (8.5)$$

1240 Thus the matching conditions (8.2) are appropriate if the position of the free boundary does
 1241 not decrease too rapidly.

1242 We note that (regardless of the size of the convective heat transfer coefficient μ) for
 1243 physically relevant solutions we require $\dot{s} > -1$, since the fastest the free boundary can move
 1244 inwards is the speed of the solid material. Since $K > 1$, we see from (8.5) that $U > -1$.
 1245 Thus we expect both the situations when (8.5) does and does not hold to be possible, and
 1246 physically relevant. If (8.5) does not hold, so that $\dot{s} < U$, the far-field conditions (8.2) cannot
 1247 be imposed. The overall direction of heat transfer in the far field of the boundary layer is now
 1248 left-to-right, and so we must understand the decay behaviour of the region EI problem, in
 1249 order to choose the correct far-field conditions. Since all physical effects are included in the
 1250 region EI equations (8.1), in the far field we will simply have some of these effects dropping
 1251 out of the dominant balance as the lengthscale becomes large. We will find the appropriate
 1252 far-field behaviour of the region EI model by examining the system on greater lengthscales.

8.2. The $O(1)$ domain

We now investigate the behaviour in the majority of the domain for either of the cases $\dot{s} > U$ or $\dot{s} < U$. On an $O(1)$ lengthscale, we note from the mass equations (2.12a)–(2.12b) that the chemical reaction rate must be small, at most $O(\delta)$. Since the chemical reaction rate is small, T_s must be small. We suppose that $T_s = O(\theta)$ for some small $\theta \ll 1$ to be determined. From the (dominant) $M(T_g - T_s)$ term in either energy equation (2.12c) or (2.12d), we must therefore have $T_g = O(\theta)$, as well. By balancing the advection or chemical reaction terms in the solid heat equation, we see that the difference $T_g - T_s$ must be at most order

$$\epsilon := \max \left(\delta\theta, \exp \left(-\frac{A}{\theta} \right) \right) \ll \theta, \quad (8.6)$$

so that the two temperatures are equal at leading order in θ . Thus the model (2.12) reduces to a single-temperature system over $O(1)$ lengthscales.

Specifically, we write $T_s = \theta T + \epsilon T_s^1$ and $T_g = \theta T + \epsilon T_g^1$. Adding the two heat equations (2.12c) and (2.12d) together, the convective heat transfer between the phases cancel, and we obtain a single equation for the leading-order temperature T , namely

$$\delta\theta \left(\frac{\partial}{\partial t} (CT) + \frac{\partial}{\partial x} ((Kf - C)T) \right) = -\gamma C \exp \left(A \left(1 - \frac{1}{\theta T} \right) \right). \quad (8.7)$$

Here we have absorbed the term for the heat transfer between phases due to the mass transfer into the advection term, by using the solid mass equation (2.12a). We have neglected the heat diffusion term, which is always smaller than the advection term on lengthscales greater than $O(\delta)$. Only the two remaining terms in (8.7) — heat advection, and heat consumed by chemical reaction — can possibly enter the dominant balance, and we must choose the appropriate θ to ensure the correct balance. We will see that the $O(\epsilon)$ correction is smaller than the corrections due to other effects, and so the single-temperature model (8.7) is indeed valid. We note that equation (8.7) is a first-order, hyperbolic equation for T , and so our entire system is hyperbolic on the $O(1)$ lengthscale: the C characteristic curves travel right-to-left, the f characteristic curves travel left-to-right, and the T characteristic curves from (8.7) travel in direction $Kf - C$. The correct choice of scaling θ , and so the balance in (8.7), depends on the direction of the T characteristics, and hence on the sign of $Kf - C$.

We notice that the chemical reaction rate must be at most order $\delta\theta$ over this $O(1)$ lengthscale in order to be balanced by the advection term in (8.7). From the equations of conservation of mass (2.12a)–(2.12b), this means that both C and f are uniform at leading order in θ over $O(1)$ domains. We will later see that there are no regions of $O(1)$ variation in C or f outside of region EI, and thus both

$$C = 1 + \epsilon_C \hat{C} \quad \text{and} \quad f = f^\infty(t) + \epsilon_C \hat{f} \quad (8.8)$$

are uniform at leading order over the entire $O(1)$ domain $x > s(t)$. Here the scaling $\epsilon_C \ll 1$ of the correction terms is yet to be determined. This depends on which boundary the T characteristic curves originate: we will find $\epsilon_C \sim \delta^{-1} Q(T^{\text{in}}) = o(T^{\text{in}})$ for when these originate at the $x = 1$ boundary, and $\epsilon_C = \theta_*^2$ when these originate at $x = s$ (in either case $\epsilon_C \gg \epsilon$, the error in the single-temperature approximation, defined by (8.6)). In (8.8) we have fixed $C^\infty = 1$ at leading order using the boundary condition at $x = 1$, and

$$f^\infty(t) = f_* + (1 + \dot{s}(t))(1 - C_*), \quad (8.9)$$

by matching with the boundary layer EI as $X \rightarrow \infty$. We note that the leading-order gas flux f^∞ is spatially uniform but not constant in time. Thus the direction of the characteristic

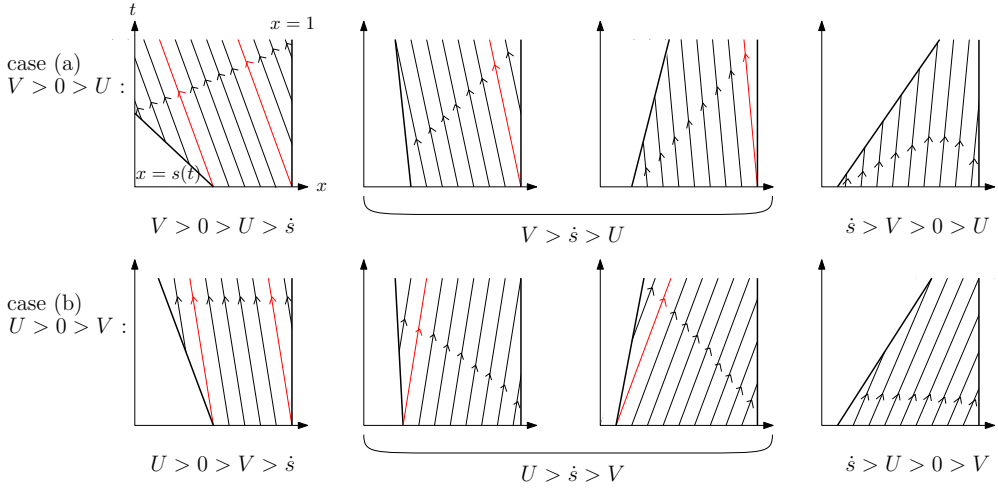


Figure 10: Characteristic diagrams in the cases $V > 0 > U$ and $V < 0 < U$, for different sizes of \dot{s} . The red characteristics mark the boundaries between regions with the characteristics originating at different boundaries of the domain, or at the initial data. In general, we expect to have different dominant behaviour on either side of these bounding characteristics.

1296 curves for T are uniform over the entire $O(1)$ domain, and are given by

1297
$$Kf - C = Kf^\infty(t) - 1 + O(\epsilon_C). \quad (8.10)$$

1298 Since the characteristic curve slopes depend only on time and do not vary spatially, we do
1299 not expect characteristic curves to cross anywhere in the domain.

1300 We will have different behaviour (and different θ scalings) in regions where the charac-
1301 teristics of (8.7) originate at different boundaries of the (x, t) domain. We note that these
1302 T -characteristic curves, with gradient $Kf^\infty - 1$, can originate at $x = 1$ only if $Kf^\infty < 1$, or
1303 equivalently only if

1304
$$\dot{s} < V := \frac{1 - K(f_* + (1 - C_*))}{K(1 - C_*)}. \quad (8.11)$$

1305 Also, characteristic curves can originate at $x = s(t)$ only if $Kf^\infty - 1 > \dot{s}$, or equivalently
1306 (since we are assuming throughout that $K < 1$) only if

1307
$$\dot{s} < U, \quad (8.12)$$

1308 where (in a slight abuse of notation) we write $U := U|_{C^\infty=1}$ for the function $U(C^\infty)$ defined
1309 as in (8.5), evaluated at $C^\infty = 1$. Thus characteristic curves in the outer domain originate at
1310 $x = s$ if and only if the heat transfer is left-to-right in the far-field of the (moving) boundary
1311 layer EI. We note that U and V have opposite signs: if (as in case Ea) $K(f_* + 1 - C_*) < 1$ then
1312 $U < 0 < V$, whereas if (as in case Eb) $K(f_* + 1 - C_*) > 1$ then $U > 0 > V$. For either sign of
1313 $K(f_* + 1 - C_*) - 1$, there are a variety of solution structures depending on which, if any, of
1314 (8.11) and (8.12) hold, since (8.11) and (8.12) are neither mutually exclusive nor mutually
1315 inclusive. In particular, the steady-state solutions in the cases Ea and Eb, are illustrated in
1316 figures 9a and 9b. The characteristic diagrams for the T problem (8.7), showing the different
1317 structures possible (in the general, non-steady case), are presented in figure 10. As \dot{s} changes
1318 continuously in time, there are other structures possible than those shown here.

1319 We consider regions with characteristic curves originating at $x = 1$ and $x = s$ separately,
1320 as the temperature scaling θ , and so too the solution behaviour, is different in these two
1321 cases. To fully determine the non-steady solutions, we should also investigate the case when

characteristic curves originate at the $t = 0$ axis in the diagrams of figure 10. The solution in this case is determined by the initial conditions, in particular on the magnitude of the temperature, but for simplicity we do not discuss this here.

8.2.1. T characteristics originating at $x = 1$

In a region with the characteristics originating from $x = 1$, since $T = T^{\text{in}}$ at $x = 1$, we take $\theta = T^{\text{in}} \ll 1$. Since $Q(T^{\text{in}}) \ll \delta T^{\text{in}}$, the chemical reaction terms in both the heat and mass equations are negligible, and so at leading order (expanding in powers of T^{in}) we find $T_s = T_g = T^{\text{in}}$, and of course as above we have $C = 1$ and $f = f^\infty$ throughout this region. This is true for the steady-state case Ea, with $K f^\infty < 1$. The leading-order, steady-state, composite solution in this case is given in (8.29) below. Regions with T characteristics originating at $x = 1$ are therefore purely advective: there is no change of temperature, solid concentration, or gas flux, since the material is too cold for any chemical reaction to occur.

8.2.2. T characteristics originating at $x = s(t)$

In a region where the characteristics originate at $x = s$, then the temperature scaling $\theta = \theta_*$ must be determined by the temperature leaving the boundary layer EI. We suppose that the temperature is approximately constant, and make the changes of variables $T = \theta_*(1 + \theta_* \hat{T})$ and $C = 1 + \theta_*^2 \hat{C}$ and $f = f^\infty + \theta_*^2 \hat{f}$. In (8.7), we see that θ_* must be determined by a balance between the chemical reaction term and the heat advection, and we therefore require that θ_* is the smallest positive solution of

$$\delta \theta_*^2 e^{A/\theta_*} = 1, \quad (8.13)$$

namely,

$$\theta_* = \frac{-A}{2W_{-1}\left(-\frac{A}{2}\sqrt{\delta}\right)} = \frac{A}{\log\left(\frac{1}{\delta}\right)} \left(1 + \frac{\log(\log(\delta)^2)}{\log(\delta)} + \dots\right), \quad (8.14)$$

and we note that $\theta_* \rightarrow 0$ as $\delta \rightarrow 0$. As an aside, we also note that the temperature through the majority of the domain in case Db is

$$\eta_D \left(1 + 2\eta_D \frac{\log(\eta_D)}{A}\right) = \frac{A}{\log\left(\frac{1}{\delta\mu}\right)} \left(1 + \frac{\log(\log(\delta\mu)^2)}{\log(\delta\mu)} + \dots\right), \quad (8.15)$$

which is the same as θ_* to leading order, since we had $\mu \ll \delta^{-1}$ in case Db. Indeed all of $\eta_B, \eta_C, \eta_D \sim A/(-\log(\delta))$ at leading order, although the correction terms differ, and, being logarithmic, are not particularly small.

At leading order in θ_* , the equations (2.12a)–(2.12b) and (8.7) become

$$\frac{\partial \hat{C}}{\partial t} - \frac{\partial \hat{C}}{\partial x} = -\exp(A(1 + \hat{T})), \quad \frac{\partial \hat{f}}{\partial x} = \exp(A(1 + \hat{T})), \quad (8.16)$$

$$\frac{\partial \hat{T}}{\partial t} + (K f^\infty - 1) \frac{\partial \hat{T}}{\partial x} = -\gamma \exp(A(1 + \hat{T})). \quad (8.17)$$

Solving (8.17) by the method of characteristics, we find the characteristic curves, parameterised by ξ and the time t_0 at which $x = s_0$,

$$t(\xi, t_0) = \xi + t_0, \quad (8.18)$$

$$x(\xi, t_0) = s(t_0) + \int_{\xi=0}^{\xi} [K(f_* + (1 + \hat{s}(\hat{\xi} + t_0))(1 - C_*)) - 1] d\hat{\xi}. \quad (8.19)$$

1359 Along these characteristic curves,

$$1360 \quad \hat{T}(\xi) = -\frac{1}{A} \log \left(A e^A \gamma \xi \right). \quad (8.20)$$

1361 Here we have fixed the constant of integration so that \hat{T} blows up as $\xi \rightarrow 0$, i.e., as the
 1362 characteristic curve approaches $x = s_0$. We may then find \hat{C} and \hat{f} from (8.16), with the
 1363 requirements that $\hat{C} = 0$ at $x = 1$ and $\hat{f} = 0$ at $x = s(t)$.

1364 In particular, in steady state, the full solution is

$$1365 \quad T = \theta_* - \frac{\theta_*^2}{A} \log \left(\frac{A \gamma e^A}{K F^\infty - 1} (x - s) \right), \quad C = 1 + \theta_*^2 \frac{K f^\infty - 1}{A \gamma} \log \left(\frac{x - s}{1 - s} \right), \quad (8.21)$$

1367 and, as always in steady state, $f = f_* + C - C_*$. Specifically, this is the region EbII solution
 1368 in the steady-state case Eb, illustrated in figure 9b, since in case Eb, characteristic curves
 1369 originate at $x = s$ and end at $x = 1$.

1370 Given this steady-state solution, we now understand the far-field behaviour, and the
 1371 appropriate boundary conditions for the region-EbI problem. Since equation (8.1a) is first
 1372 order in C , we prescribe the leading-order far-field behaviour

$$1373 \quad C \rightarrow 1 \quad \text{as } X \rightarrow \infty, \quad (8.22)$$

1375 while for the T_s boundary condition, we can impose the correct far-field balance

$$1376 \quad (K f^\infty - 1) \frac{dT_s}{dX} + \gamma \exp \left(A \left(1 - \frac{1}{T_s} \right) \right) \rightarrow 0 \quad \text{as } X \rightarrow \infty. \quad (8.23)$$

1378 We note that when characteristics of the outer problem move *into* region EI, the leading-
 1379 order problem (8.1) is accurate to order $\theta \ll 1$, because the temperature (which is order θ)
 1380 outside the boundary layer induces a switchback correction within the boundary layer. In
 1381 particular, in the steady-state case Ea, we found $\theta = T^{\text{in}}$, and thus the switchback error in
 1382 case Ea is $O(T^{\text{in}})$. Conversely, when $\dot{s} < U$ and so the characteristics of the outer problem
 1383 originate at $x = s$, the boundary conditions are given by (8.22)–(8.23), and we do not have a
 1384 switchback correction due to the outer region. Instead the main source of error is the $O(\theta_*^2)$
 1385 error in the far-field boundary condition (8.22) for C .

1386 8.3. Region EbIII

1387 In situations where characteristics start at $x = s$ and end at $x = 1$ (such as in the steady-state
 1388 case Eb in figure 9b), we must introduce a boundary layer at $x = 1$ of width $O(\delta)$, in order
 1389 to impose the boundary condition $T = T^{\text{in}}$ at $x = 1$. (In steady state, we denote this boundary
 1390 layer region EbIII.) This is the region, analogous to regions BIV and CIV, in which the heat
 1391 transferred from the gas to the solid heats the solid from its input temperature, T^{in} . We make
 1392 the change of variables $x = 1 - \delta Y$, and set

$$1393 \quad T_s = \theta_* \bar{T}_s, \quad T_g = \theta_* \bar{T}_g, \quad (8.24)$$

1394 for $\bar{T}_s < 1$. The chemical reaction rate is then

$$1395 \quad \bar{Q} \sim \exp \left(-\frac{A}{\theta_* \bar{T}_s} \right) \ll e^{-A/\theta_*} = \delta \theta_*^2, \quad (8.25)$$

1396 by definition of θ_* . Thus as the chemical reaction rate is small, so that $C = 1 + O(\theta_*^2)$
 1397 and $f = f^\infty + O(\theta_*^2)$ are uniform to leading order in the boundary layer. We expand $\bar{T}_s =$
 1398 $\bar{T}_s^0(Y, t) + O(\theta_*)$ and $\bar{T}_g = \bar{T}_g^0(Y, t) + O(\theta_*)$, and at leading order in the heat equations (2.12c)

1399 and (2.12d) we find the quasi-steady equations

$$1400 \quad \frac{\partial \bar{T}_s^0}{\partial Y} = \frac{\partial^2 \bar{T}_s^0}{\partial Y^2} + M(\bar{T}_g^0 - \bar{T}_s^0), \quad K f^\infty \frac{\partial \bar{T}_g^0}{\partial Y} = M(\bar{T}_g^0 - \bar{T}_s^0), \quad (8.26a)$$

1402 (the time-dependence is through $f^\infty(t)$), with boundary conditions

$$1403 \quad \bar{T}_s^0 = \frac{T^{\text{in}}}{\theta_*} \quad \text{at } Y = 0, \quad \bar{T}_s^0, \bar{T}_g^0 \rightarrow 1 \quad \text{as } Y \rightarrow \infty. \quad (8.26b)$$

1405 The solution of (8.26) is

$$1406 \quad \bar{T}_s^0 = 1 - \left(1 - \frac{T^{\text{in}}}{\theta_*}\right) \exp(\chi(t)Y), \quad \bar{T}_g^0 = 1 + \frac{\chi(t) - 1}{K f^\infty} \left(1 - \frac{T^{\text{in}}}{\theta_*}\right) \exp(\chi(t)Y), \quad (8.27)$$

1408 where the function of time $\chi(t)$ is given by

$$1409 \quad \chi(t) = \frac{1}{2} \left(\frac{M}{K f^\infty} + 1 \right) - \frac{1}{2} \sqrt{\left(\frac{M}{K f^\infty} - 1 \right)^2 + 4M}. \quad (8.28)$$

1410 8.4. Composite solutions for cases Ea and Eb

1411 In case Ea, the characteristic curves originate at $x = 1$, and so all dependent variables are
1412 uniform to leading order outside region EI. In this case the steady-state composite solution is

$$1413 \quad C^{\text{Ea}} = C^0 \left(\frac{x - s_0}{\delta} \right), \quad T_s^{\text{Ea}} = T_s^0 \left(\frac{x - s_0}{\delta} \right) + T^{\text{in}}, \quad T_g^{\text{Ea}} = T_g^0 \left(\frac{x - s_0}{\delta} \right) + T^{\text{in}}. \quad (8.29)$$

1415 The steady-state composite solution in case Eb, when characteristics originate at $x = s$, is

$$1416 \quad C^{\text{Eb}} = C^0 \left(\frac{x - s_0}{\delta} \right), \quad (8.30a)$$

$$1417 \quad T_s^{\text{Eb}} = T_s^0 \left(\frac{x - s_0}{\delta} \right) + \theta_* \bar{T}_s^0 \left(\frac{1 - x}{\delta} \right) - \theta_*, \quad (8.30b)$$

$$1418 \quad T_g^{\text{Eb}} = T_g^0 \left(\frac{x - s_0}{\delta} \right) + \theta_* \bar{T}_g^0 \left(\frac{1 - x}{\delta} \right) - \theta_*. \quad (8.30c)$$

1420 8.5. Additional structures in some time-dependent cases

1421 Some time-dependent solutions will have the same structure as the steady-state cases Ea and
1422 Eb. Additional structures are also possible in situations where characteristic curves originate
1423 at both $x = 1$ and $x = s$. The boundary between these regions is the characteristic curve (8.19)
1424 which comes from $x = s$ at the point where $\dot{s} = \min(U, V)$ and subsequently $\dot{s} < \min(U, V)$
1425 (shown in red in figure 10). We denote this dividing characteristic curve by $x_0(t)$. Around
1426 this characteristic curve, we expect there to be a thin layer, of width $\sqrt{\delta}$ to balance the time-
1427 derivative and diffusion terms, in which diffusion smooths out the discontinuity between the
1428 two regions. A schematic of the solution structure in this case is shown in figure 11.

1429 Combining the analyses above we can understand the time-dependent solutions from a
1430 number of initial states and values of \dot{s} . Of course, \dot{s} is found as part of the solution of the
1431 boundary layer problem (8.1), so that the solution structure may change at different times,
1432 and not all ranges of \dot{s} considered in this section may be obtainable from physically relevant
1433 initial conditions.

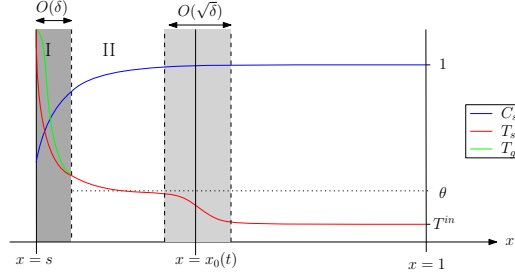


Figure 11: Schematic in a case where characteristics originate at both $x = 1$ and $x = s(t)$ (with initial condition $T = T^{\text{in}}$ for $x > s$).

9. Case F: $\mu \gg \delta^{-1}$, very large heat transfer

In this section we consider $\mu \gg \delta^{-1}$, so that the heat transfer between phases is the dominant term in each of the heat equations, unbalanced by any other term on lengthscales greater than $O(\mu^{-1})$. Thus, on lengthscales greater than $O(\mu^{-1})$, we must have a single temperature $T_s = T_g =: T$ with $O(\mu^{-1})$ corrections. Writing $T_s = T + \mu^{-1}T_s^1$ and $T_g = T + \mu^{-1}T_g^1$, and adding the two heat equations at leading order in μ^{-1} , as in case E, we are left with a single equation for T ,

$$\delta \left(\frac{\partial}{\partial t} (CT) + \frac{\partial}{\partial x} ((Kf - C)T) \right) = \delta^2 \frac{\partial^2 T}{\partial x^2} - \gamma C \exp \left(A \left(1 - \frac{1}{T} \right) \right). \quad (9.1a)$$

As in case E, we have absorbed the term for the heat transfer between phases due to the mass transfer into the advection term, by using the solid mass equation (2.12a). Since $T_s = T + O(\mu^{-1})$, the equations of conservation of mass, (2.12a) and (2.12b), may be written, to leading order in μ^{-1} , as

$$\delta \left(\frac{\partial C}{\partial t} - \frac{\partial C}{\partial x} \right) = -C \exp \left(A \left(1 - \frac{1}{T} \right) \right), \quad (9.1b)$$

$$\delta \frac{\partial f}{\partial x} = C \exp \left(A \left(1 - \frac{1}{T} \right) \right). \quad (9.1c)$$

The equations (9.1) are valid — at leading order in μ^{-1} — in the entirety of the domain except in boundary layers of width $O(\mu^{-1})$, in which T_s and T_g may differ at leading order. Since at $x = s$ we have imposed $T_s = T_g = \rho/s$ are equal, we do not encounter any such regions, and the system (9.1) holds at leading order throughout the domain. (We would, however, need to include the $O(\mu^{-1})$ terms in order to look for corrections to the leading-order solutions.)

As in Section 8, we find different behaviour depending on the relative sizes of \dot{s} , U , and V . These structures are identical to those obtained in the case $\mu = O(\delta^{-1})$ as described in Section 8, and the analysis for the $O(1)$ regions of the domain is identical. However, in the boundary layer(s) of width $O(\delta)$, the gas and solid temperatures remain equal at leading order in μ^{-1} .

Specifically, in the boundary layer of width δ located at $x = s$ (the reaction region), denoted region FI, we make the usual change of variables $x = s + \delta X$. We find that $f = f_* + (1 + \dot{s})(C - C_*) + O(\delta)$. We expand the remaining dependent variables as

$$C = C^0(X, t) + O(\zeta), \quad T = T^0(X, t) + O(\zeta), \quad s = s_0(t) + O(\zeta), \quad (9.2)$$

where the switchback error $\zeta \ll 1$ is determined — as in case E — by the size of the temperature in the outer problem in case Fa, so that $\zeta = T^{\text{in}}$, and by the error in C in the

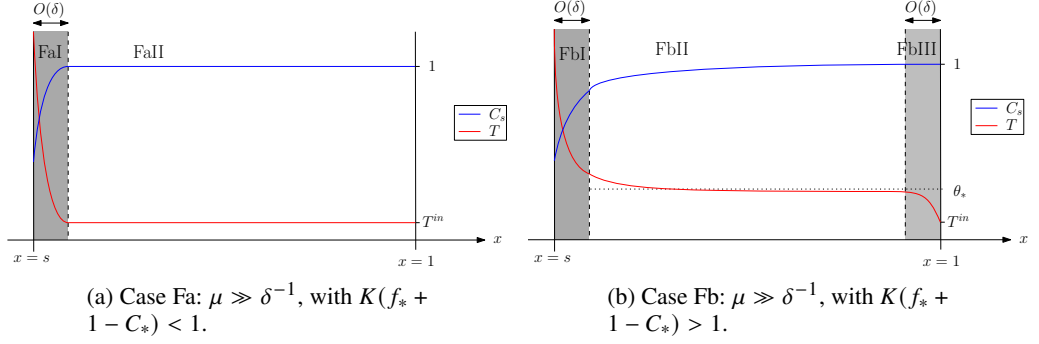


Figure 12: Schematic diagrams illustrating the asymptotic solution structures, in steady state, for case F $\mu \gg \delta^{-1}$.

Region	Spatial Variable	Size of Q	Dominant terms in (3.1)	Dependent Variables
FI	$x = s + \delta X$	$Q = O(1)$	1, 2, 3, 4, 5	$C, f,$ $T_s = T_g = T$
FaII	x	$Q \ll \delta T^{\text{in}}$	1	$C = 1, f = f^\infty,$ $T_s = T_g = T^{\text{in}}$
FbII	x	$Q = O(\delta \theta_*^2)$	1, 5	$C = 1 + \theta_*^2 \hat{C},$ $T_s = T_g = \theta_*(1 + \theta_* \hat{T})$
FbIII	$x = 1 - \delta Y$	$Q \ll \delta \theta_*^2$	1, 2	$C = \bar{C}, f = f^\infty,$ $T_s = T_g = \theta_* \bar{T}$

Table 6: Summary of the notation in each asymptotic region in the cases Fa ($\mu \gg \delta^{-1}$, $K(f_* + 1 - C_*) < 1$) and Fb ($\mu \gg \delta^{-1}$, $K(f_* + 1 - C_*) > 1$), corresponding to the diagrams in figure 12.

outer region in case Fb, so that $\zeta = \theta_*^2$. At leading order, the equations (9.1b) and (9.1a) then become

$$(1 + \dot{s}_0) \frac{\partial C^0}{\partial X} = C^0 \exp \left(A \left(1 - \frac{1}{T^0} \right) \right), \quad (9.3a)$$

$$\begin{aligned} \frac{\partial}{\partial X} \left(\left(K(f_* + (1 + \dot{s}_0)(C^0 - C_*)) - (1 + \dot{s}_0)C^0 \right) T^0 \right) \\ = \frac{\partial^2 T^0}{\partial X^2} - \gamma C^0 \exp \left(A \left(1 - \frac{1}{T^0} \right) \right). \end{aligned} \quad (9.3b)$$

The leading-order boundary conditions are

$$C^0 = C_* \quad \text{and} \quad T^0 = \frac{\rho}{s_0} \quad \text{at } X = 0, \quad (9.3c)$$

along with appropriate matching conditions as $X \rightarrow \infty$, which take the same forms as in case E, depending on whether the T characteristic curves move into or out of region FI.

The only other region which differs from case E is the boundary layer of width δ located at $x = 1$ (in which the temperature is heated from its input temperature, T^{in}), in situations for

1479 which this boundary layer is needed. In this region, denoted region FbIII in the steady-state
 1480 case Fb, we set $x = 1 - \delta Y$, and rescale $T = \theta_* \bar{T}$. As in case Eb, we see that for $\bar{T} < 1$, the
 1481 chemical reaction rate is small, $O(\delta\theta_*^2)$, and drops out of the dominant balance. Thus we
 1482 find from (9.1b)–(9.1c) that both $C = 1 + O(\theta_*^2)$ and $f = f^\infty + O(\theta_*^2)$ are uniform at leading
 1483 order. Expanding $\bar{T} = \bar{T}^0 + O(\theta_*)$, at leading order the temperature equation (9.1a) therefore
 1484 becomes

$$1485 \quad (1 - Kf^\infty) \frac{\partial \bar{T}^0}{\partial Y} = \frac{\partial^2 \bar{T}^0}{\partial Y^2}, \quad (9.4)$$

1487 which admits the solution

$$1488 \quad \bar{T}^0 = 1 - \left(1 - \frac{T^{\text{in}}}{\theta_*}\right) \exp((1 - Kf^\infty)Y). \quad (9.5)$$

1490 Here we have used the boundary conditions at $Y = 0$ and matching as $Y \rightarrow \infty$, as in region
 1491 EbIII. The rest of the analysis for case F follows precisely as for case E, with $T_s = T_g$ in
 1492 the majority of the domain. Steady-state solutions for each case Fa and Fb are illustrated
 1493 in figures 12a–12b, and the changes of variable are summarised in table 6. The respective
 1494 leading-order, steady-state composite solutions take the form

$$1495 \quad C^{\text{Fa}} = C^0 \left(\frac{x - s_0}{\delta} \right), \quad T^{\text{Fa}} = T^0 \left(\frac{x - s_0}{\delta} \right) + T^{\text{in}}, \quad (9.6)$$

1497 and

$$1498 \quad C^{\text{Fb}} = C^0 \left(\frac{x - s_0}{\delta} \right), \quad T^{\text{Fb}} = T^0 \left(\frac{x - s_0}{\delta} \right) + \theta_* \bar{T}^0 \left(\frac{1 - x}{\delta} \right) - \theta_*. \quad (9.7)$$

1500 10. Numerical solution of the leading-order problems in region I

1501 In all cases A to F, we have found leading-order solutions analytically in all regions of the
 1502 domain except for in region I. In this section, for all cases A to F we solve the relevant
 1503 region-I model numerically. In particular, in all cases A to F, we solve for the leading-order
 1504 position, $x = s_0$, of the free boundary as part of the solution of the region-I problem. The
 1505 region-I problems are all quasi-steady in that the only time derivatives in the leading-order
 1506 models are the \dot{s} terms due to the moving interface (this is also true in case D, although since
 1507 we restricted to the steady-state case, we did not show it in Section 7). However, in cases C,
 1508 E, and F, we saw that the values or the form of the boundary conditions for region I depend
 1509 on the genuinely time-varying behaviour in other regions of the domain. To examine the
 1510 region-I problem in isolation, we therefore restrict to the steady-state region-I equations in
 1511 all cases C to F. However, we will examine the quasi-steady behaviour for cases A and B, by
 1512 finding the relationship between \dot{s}_0 and s_0 . To do this we impose the value of s_0 and solve for
 1513 \dot{s}_0 , and then sweep through the value of s_0 (whereas for the steady-state solutions we impose
 1514 $\dot{s}_0 = 0$ and solve for s_0). We therefore still treat the quasi-steady region-I problem for cases
 1515 A and B as a boundary value problem.

1516 The numerical solutions of the region-I boundary value problems studied in this section are
 1517 computed in MATLAB (2021) using the inbuilt solver bvp4c. This uses a Runge-Kutta finite-
 1518 difference formula and collocation method to choose and refine the mesh. The algorithm
 1519 is fourth-order accurate as the mesh is refined, uniformly over the domain (Kierzenka &
 1520 Shampine 2001).

10.1. Cases A–D

In cases A–D, we saw that the gas variables decoupled from the leading-order problem in region I, and we obtained the system (4.8), although with different matching conditions for cases C and D. The leading-order region-I problem in all cases A–D may be summarised as

$$-(\dot{s}_0 + 1) \frac{\partial C^0}{\partial X} = -C^0 \exp \left(A \left(1 - \frac{1}{T_s^0} \right) \right), \quad (10.1a)$$

$$-(\dot{s}_0 + 1) C^0 \frac{\partial T_s^0}{\partial X} = \frac{\partial^2 T_s^0}{\partial X^2} - \gamma C^0 \exp \left(A \left(1 - \frac{1}{T_s^0} \right) \right), \quad (10.1b)$$

with the boundary conditions

$$C^0 = C_*, \quad T^0 = \frac{\rho}{s_0}, \quad \text{at } X = 0, \quad (10.1c)$$

and

$$T_s^0 \rightarrow 0, \quad C^0 \rightarrow \begin{cases} 1, & \text{in cases A and B,} \\ C^\infty, & \text{in cases C and D,} \end{cases} \quad \text{as } X \rightarrow \infty. \quad (10.1d)$$

In cases C and D, we found that the value of C^∞ was given in terms of s_0 , F_s , and G_s . In steady state, we have (from (6.14) and (7.9))

$$C^\infty = \begin{cases} 1 - F_s K \frac{G_s - \hat{T}_g^0|_{x=1}}{\gamma + K \hat{T}_g^0|_{x=1}}, & \text{in case C,} \\ 1 - \frac{K F_s G_s}{\gamma}, & \text{in case D.} \end{cases} \quad (10.2)$$

The steady-state values F_s and G_s are

$$F_s = f_* + C^\infty - C_*, \quad (10.3)$$

$$G_s = \frac{\frac{f_* \rho}{s_0} + K^{-1} \int_{\bar{X}=0}^{\infty} T_s^0 C^0 \exp \left(A \left(1 - \frac{1}{T_s^0} \right) \right) d\bar{X}}{f_* + C^\infty - C_*}, \quad (10.4)$$

and in case C, $\hat{T}_g^0|_{x=1}$ is given by

$$\hat{T}_g^0|_{x=1} = -\frac{\gamma W(a_C(1))}{K(1 + W(a_C(1)))}, \quad (10.5)$$

where

$$a_C(1) = -\frac{K G_s}{\gamma + K G_s} \exp \left(-\frac{1}{\gamma + K G_s} \left(\frac{\gamma \mu}{K F_s} (1 - s_0) + K G_s \right) \right). \quad (10.6)$$

To reduce the required domain size for numerical solutions, we replace the far-field condition $T_s^0 \rightarrow 0$ with the mixed condition

$$\frac{\partial T_s^0}{\partial X} + C^0 T_s^0 \rightarrow 0, \quad (10.7)$$

derived by considering the limit $X \rightarrow \infty$ in (10.1b). The domain size was increased until the relative error in \dot{s}_0 was comparable to that made elsewhere.

In steady state (setting $\dot{s}_0 = 0$), the system (10.1) is a third-order system, with four boundary conditions, allowing us to also solve for s_0 as part of the solution. In cases A and B we find quasi-steady solutions by prescribing the value of s_0 in (10.1), and solving for \dot{s}_0 as part of the solution. We could equivalently prescribe \dot{s}_0 (as we do for the steady-state case) and solve for s_0 .

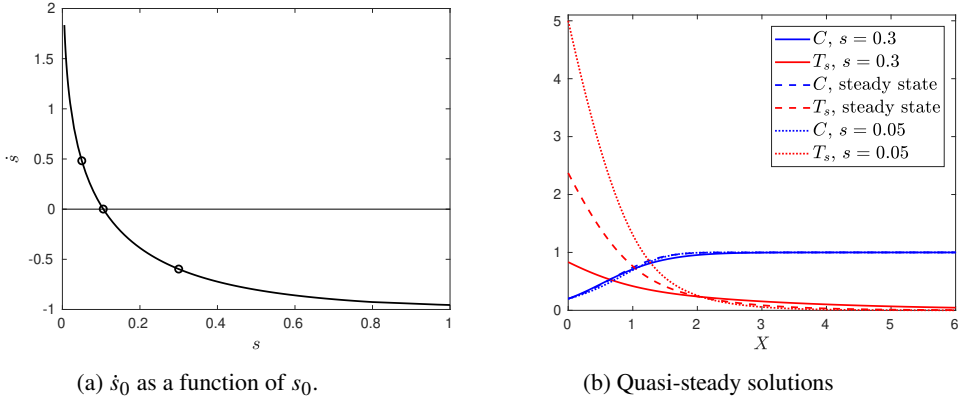


Figure 13: Numerical solutions of the region-I problem (10.1) for case A or B, taking parameter values $\gamma = 1$, $A = 1$, $C_* = 0.2$, and $\rho = 0.25$.

10.1.1. Numerical solutions in case A or B

Numerical solutions of (10.1) are shown in figure 13 in case A or B. We sweep through a range of values of s_0 , and so can understand the time-evolution of the entire system by plotting the solution \dot{s}_0 as a function of s_0 , as shown in figure 13a. We see that \dot{s}_0 becomes large and positive as $s_0 \rightarrow 0$, and that as s_0 becomes large, $\dot{s}_0 \rightarrow -1$, which is the dimensionless speed of the solid material. We observe that there is a single steady-state solution (where $\dot{s}_0 = 0$) at $s_0 \approx 0.106$. Since $\dot{s}_0 > 0$ for s_0 below the steady state, and $\dot{s}_0 < 0$ for s_0 above the steady state, this unique steady-state solution of (10.1) is stable. In figure 13b, we show the quasi-steady solution profiles T_s^0 and C^0 for three different values of s_0 , marked with circles in figure 13a, including the steady-state solution (dashed lines). For smaller s_0 , the surface temperature at $X = 0$ is greater, as required by the boundary condition (10.1c). We also see that T_s^0 decays more slowly to zero for larger s_0 . The C^0 profile does not vary significantly with s_0 , although we see variation in C^0 for a slightly larger region of X for larger s_0 , since the temperature T_s^0 decays more slowly.

In figure 14 we investigate how the solution of (10.1) in case A or B depends on the model parameters A and γ . In figures 14a and b, we plot \dot{s}_0 against s_0 , and the steady-state solutions C^0 and T_s^0 , respectively, for three values of A , the dimensionless activation energy of the chemical reaction. The temperature profile $T_s^0(X)$ at the steady state varies only slightly with A , but we see that for larger A the rate of reaction is faster, so that the steady-state C^0 varies from C_* to 1 over a shorter region of X . We also observe from figure 14a that for larger A the time-evolution curve is steeper, so that the system evolves more quickly towards its steady state.

Increasing the dimensionless energy consumed in the reaction, γ , has the effect of decreasing s_0 , as seen in figure 14c. In particular, the steady-state position s_0 decreases as γ increases, so that the surface temperature $T_s^0(0)$ increases with increasing γ , as seen in figure 14d. The temperatures must be higher at the steady state in order for there to be enough energy in the system for the chemical reactions to consume all of the incoming solid material.

We do not show the variation of solutions with the parameter ρ , as this simply introduces a scaling of s_0 , as may be seen from the form (10.1) of the model, or indeed of the full model (2.12).

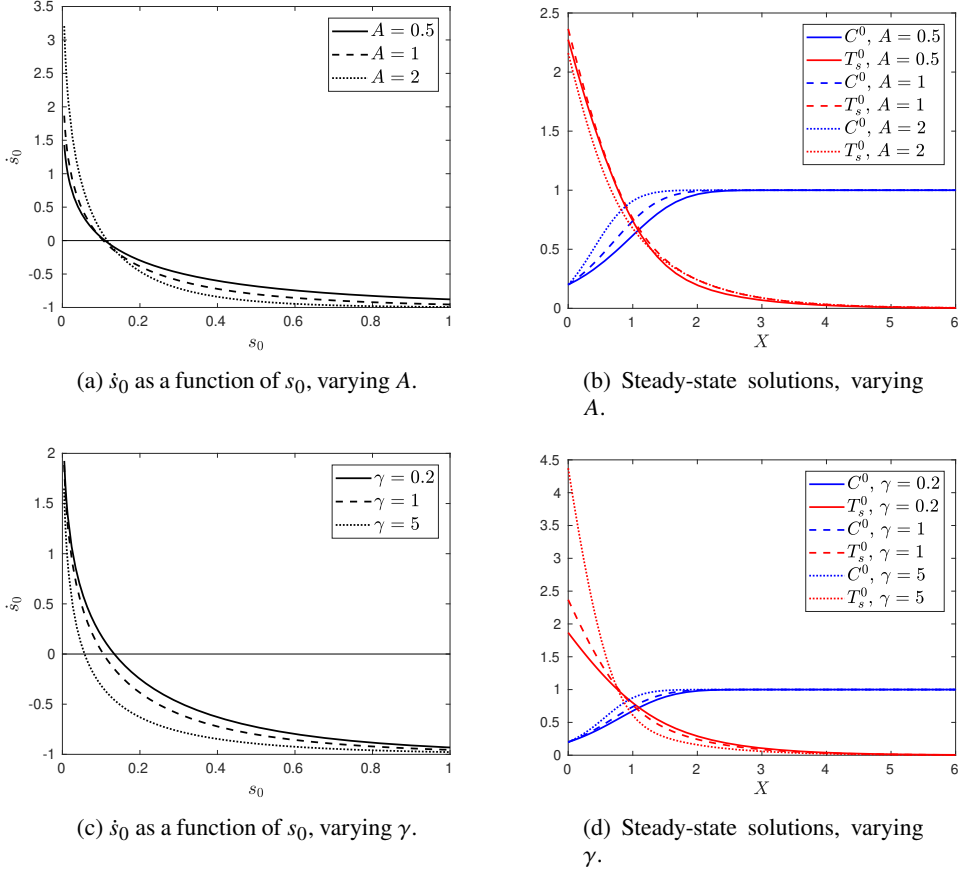


Figure 14: Numerical solutions of (10.1) for case A or B, varying the parameter values A (top) and γ (bottom). Unless otherwise stated, we take parameter values $\gamma = 1$, $A = 1$, $C_* = 0.2$, and $\rho = 0.25$.

10.1.2. Numerical solutions in case C

We show steady-state numerical solutions of (10.1) for case C in figure 15. The profiles of C^0 and T_s^0 are similar in shape to those plotted for case A or B in figure 14, but now the far-field value $C^\infty < 1$ is determined as part of the solution. Compared with solutions for case A or B, the steady-state solutions have a larger s_0 , and correspondingly cooler temperatures T_s^0 . This is because some material consumption occurs in the outer region CII, so C^∞ is smaller and we do not require such high temperatures in order for the chemical reaction to balance the influx of material. There are additional parameters in the region CI model compared to case A and B, namely μ , K , and f_* , which come into the problem through the value of C^∞ . In figure 15 we investigate varying f_* and μ (while keeping $\mu = O(1)$). We do not show the variation with K as this cannot easily be controlled in practice, and does not affect the solution much so long as K is not too small.

As well as showing the solution profiles C^0 and T_s^0 for various f_* and μ , in figures 15a and c, respectively, we also show the variation of the solution parameters s_0 , C^∞ , F_s , and G_s , sweeping through f_* and μ , in figures 15b and d, respectively. For larger f_* , there is a greater flux of gas, and so more heat may be transferred from the gas to the solid in the outer region of the domain. We see that C^∞ decreases as f_* increases, since more material is consumed in

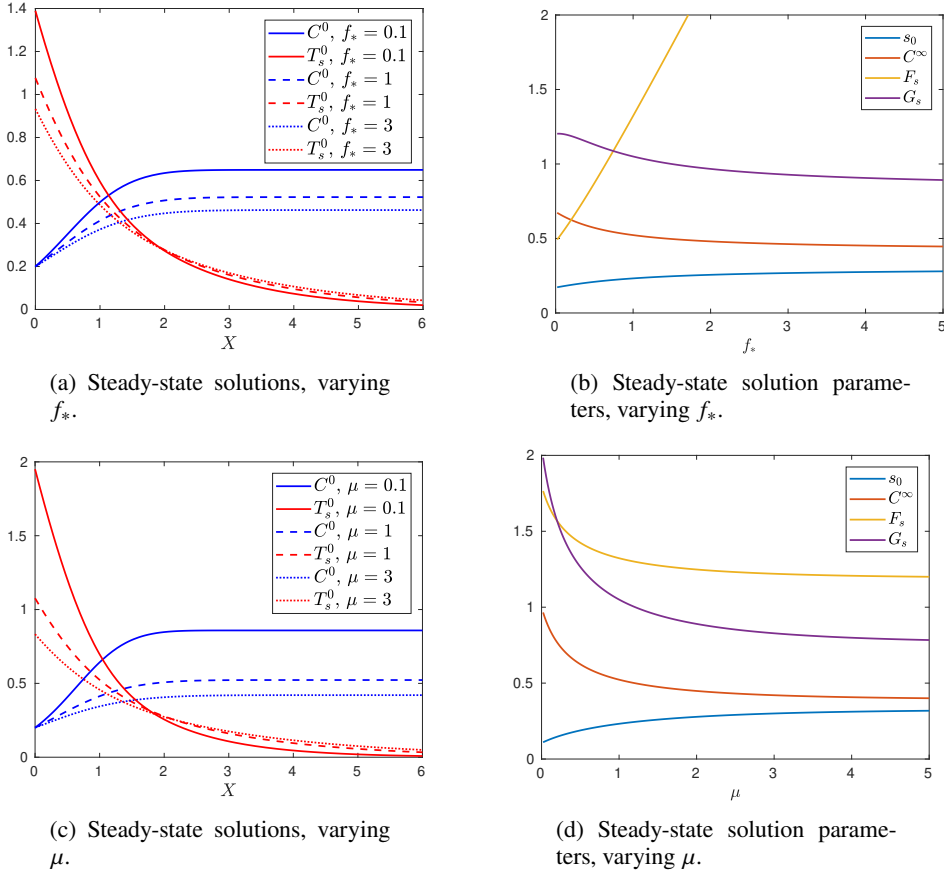


Figure 15: Numerical solutions of (10.1) for case C, varying the parameter values f_* (top) and μ (bottom). Unless otherwise stated, we take parameter values $\gamma = 1$, $A = 1$, $C_* = 0.2$, $\rho = 0.25$, $K = 0.66$, $f_* = 1$, and $\mu = 1$.

the outer region. Less heat is therefore needed in region I, and so s_0 increases. Similarly, we see that as the convective heat transfer coefficient μ increases, more material consumption can occur outside of region CI, and so C^∞ decreases, while s_0 increases. The gas flux F_s leaving region CI is a linear shift of C^∞ in this steady-state case, so decreases similarly. As s_0 increases with μ or f_* , the temperature T_s^0 becomes cooler, and this is also reflected in the decreasing temperature G_s of the gas leaving region CI.

10.1.3. Numerical solutions in case D

Solutions of the region-I problem (10.1) in case D depend on f_* and K as in case C, but do not explicitly depend on the size of μ , since the far-field concentration is $C^\infty = 1 - KF_s G_s / \gamma$. This is because the gas loses all its heat to the chemical reactions (to leading order) in the outer region, and for the region-DI analysis it does not matter exactly where in the outer region this happens.

The flux of gas through the $x = s$ boundary, f_* , is a crucial parameter for determining the gas flux F_* at the right of the domain, and thus in separating the cases Da and Db. We show the dependence of solutions to the leading-order region-I model (10.1) on f_* in figures 16a and b. Since $f = C - C_* + f_*$ everywhere in steady state, we must have $F_* = 1 - C_* + f_* + O(\eta)$.

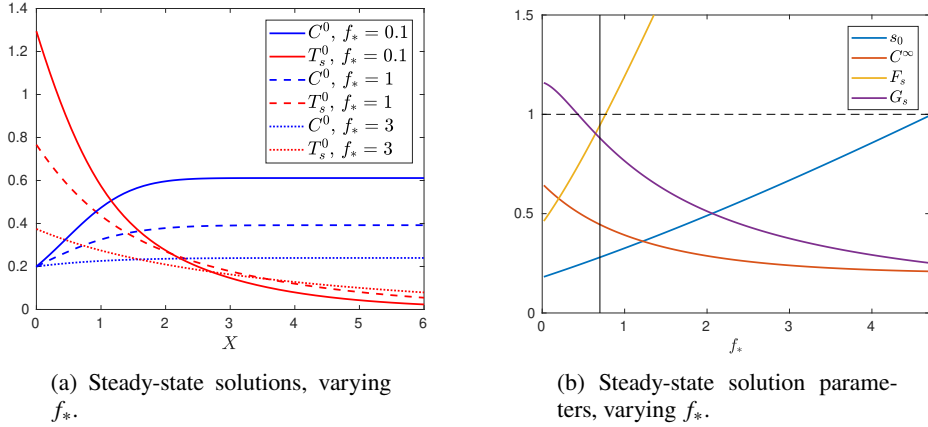


Figure 16: Steady-state numerical solutions of (10.1) for case D, varying f_* . The vertical black line in (b) at $f_* = C_* - 1 + 1/K$ separates case Da (to the left) and case Db (to the right). We take the other parameter values $\gamma = 1$, $A = 1$, $C_* = 0.2$, $\rho = 0.25$, and $K = 0.66$.

Thus, to leading order, $KF_* < 1$ if $f_* < C_* - 1 + 1/K$. The vertical black line in figure 16b shows this value $C_* - 1 + 1/K$, so that case Da is to the left of this line, while case Db is to the right. As was true in case C, we see that C^∞ decreases with f_* , although much more quickly in case D, rapidly approaching $C_* = 0.2$ for these solutions. Thus for large f_* , the majority of the solid material is consumed outside of region I. Meanwhile, we see that s_0 increases with f_* , again much more quickly than in case C. By the relatively small value of $f_* \approx 4.6$, s_0 reaches the edge of the domain at $x = 1$.

10.2. Case E

In case E the leading-order region-I problem includes all the physics of the original system. The form of the matching condition as $X \rightarrow \infty$ depends on the direction of characteristic curves in the outer problem. In steady state, the form of the matching condition is determined by the model parameters, with the steady-state case Ea when $K(f_* + 1 - C_*) < 1$, and Eb when $K(f_* + 1 - C_*) > 1$. The steady-state region-EI model is given by $f = f_* + C - C_*$, with

$$-\frac{dC^0}{dX} = -C^0 \exp\left(A\left(1 - \frac{1}{T_s^0}\right)\right), \quad (10.8a)$$

$$-C^0 \frac{dT_s^0}{dX} = \frac{d^2 T_s^0}{dX^2} + M(T_g^0 - T_s^0) - \gamma C^0 \exp\left(A\left(1 - \frac{1}{T_s^0}\right)\right), \quad (10.8b)$$

$$K \frac{d}{dX}((f_* + C^0 - C_*)T_g^0) = T_s^0 C^0 \exp\left(A\left(1 - \frac{1}{T_s^0}\right)\right) - M(T_g^0 - T_s^0), \quad (10.8c)$$

with boundary conditions

$$C^0 = C_*, \quad T_s^0 = T_g^0 = \frac{\rho}{s_0^0} \quad \text{at } X = 0, \quad (10.8d)$$

and in case Ea

$$C^0 \rightarrow 1, \quad T_s^0 \rightarrow 0 \quad \text{as } X \rightarrow \infty, \quad (10.8e)$$

1643 while in case Eb

$$1644 \quad C^0 \rightarrow 1, \quad (K(f_* + 1 - C_*) - 1) \frac{dT_s^0}{dX} + \gamma \exp \left(A \left(1 - \frac{1}{T_s^0} \right) \right) \rightarrow 0 \quad \text{as } X \rightarrow \infty. \quad (10.8f)$$

1646 To reduce the required domain size for the numerical solutions, in case Ea we analyse the
1647 system as $X \rightarrow \infty$ and hence replace the far-field condition (10.8e) for T_s^0 with

$$1648 \quad \frac{dT_s^0}{dX} + (K(f_* + 1 - C_*) - 1)T_s^0 \rightarrow 0. \quad (10.9)$$

1649 Numerical solutions for both cases Ea and Eb are shown in figure 17, varying the parameters
1650 f_* and M , on the left and right of the plot, respectively. For our choice of parameters K and
1651 C_* , we are in case Ea when $f_* < 0.7$, and in case Eb when $f_* > 0.7$. We see that s_0 increases
1652 with f_* in both cases Ea and Eb, so that temperatures are lower at $X = 0$. We also see that as
1653 f_* increases, the decay rate of the temperatures becomes much slower. The solutions appear
1654 to vary continuously as we pass from case Ea to Eb, at the critical value $f_* = 0.7$. On the
1655 right of figure 17, we see that the solution s_0 decreases slightly with M , and the temperatures
1656 at $X = 0$ correspondingly increase slightly. The rate of heat transfer between the two phases
1657 increases with M , and the rate at which these temperatures decay to zero also increases. We
1658 observe similar dependence on M for both cases Ea and Eb.

1659 10.3. Case F

1660 In case F, both temperatures are equal throughout the domain. The leading-order steady-state
1661 region FI problem is

$$1662 \quad \frac{d^0 C}{dX} = C^0 \exp \left(A \left(1 - \frac{1}{T^0} \right) \right), \quad (10.10a)$$

$$1663 \quad \frac{d}{dX} \left((K(f_* + 1)(C^0 - C_*) - C^0)T^0 \right) = \frac{d^2 T^0}{dX^2} - \gamma C^0 \exp \left(A \left(1 - \frac{1}{T^0} \right) \right), \quad (10.10b)$$

1665 with

$$1666 \quad C^0 = C_*, \quad T^0 = \frac{\rho}{s_0} \quad \text{at } X = 0, \quad (10.10c)$$

1667 and in case Fa (when $K(f_* + 1 - C_*) < 1$)

$$1668 \quad C^0 \rightarrow 1, \quad T^0 \rightarrow 0 \quad \text{as } X \rightarrow \infty, \quad (10.10d)$$

1670 while in case Fb (when $K(f_* + 1 - C_*) > 1$)

$$1671 \quad C^0 \rightarrow 1, \quad (K(f_* + 1 - C_*) - 1) \frac{dT_s^0}{dX} + \gamma \exp \left(A \left(1 - \frac{1}{T_s^0} \right) \right) \rightarrow 0 \quad \text{as } X \rightarrow \infty. \quad (10.10e)$$

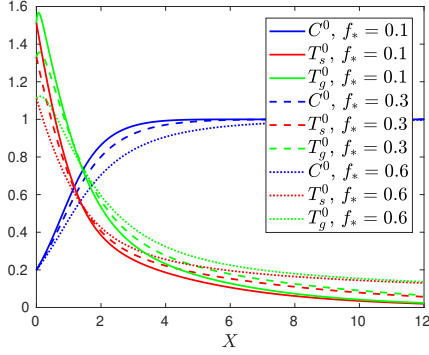
1673 To reduce the required numerical domain, in case Fa, we use the far-field condition

$$1674 \quad \frac{dT_s^0}{dX} + (K(f_* + 1 - C_*) - 1)T_s^0 \rightarrow 0. \quad (10.11)$$

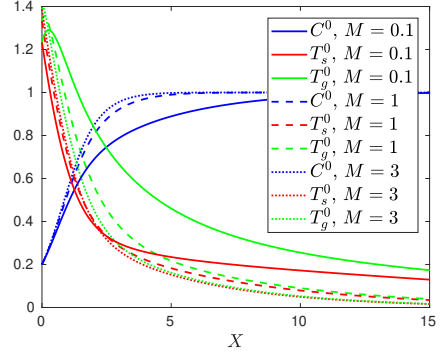
1675 Numerical solutions of (10.10) in both cases Fa and Fb are shown in figure 18 where we vary
1676 the parameter f_* , with similar qualitative results to case E.

1677 11. Comparison of composite and numerical steady-state solutions

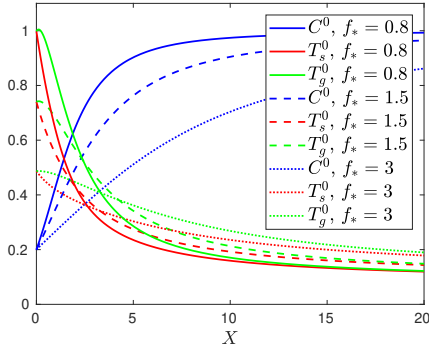
1678 Having computed the solution of the region-I problem, we can construct the composite
1679 solution for each case A to F from the analytical forms found in Sections 4–9. We also compute



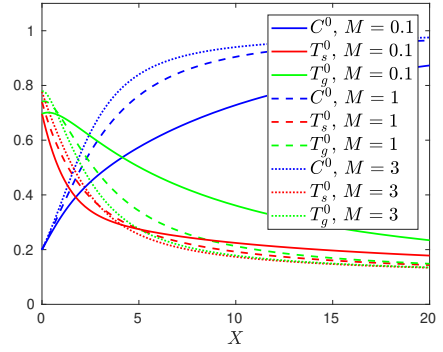
(a) Steady-states in case Ea, varying f_* .



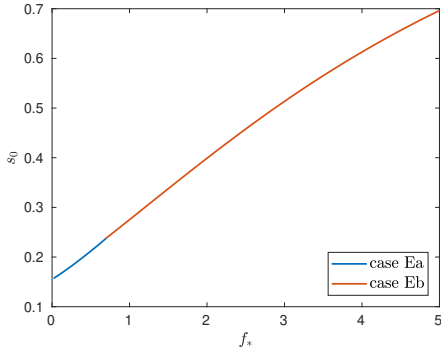
(b) Steady-states in case Ea, varying M .



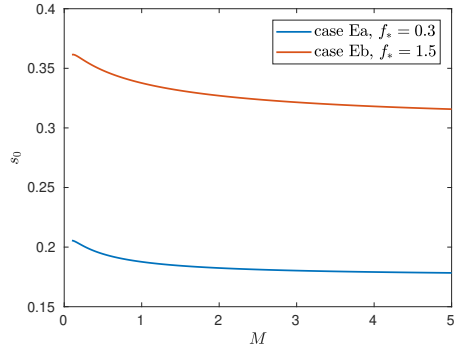
(c) Steady-states in case Eb, varying f_* .



(d) Steady-states in case Eb, varying M .



(e) Steady-state s_0 , varying f_* .



(f) Steady-state s_0 , varying M .

Figure 17: Steady-state numerical solutions of (10.8) for cases Ea and Eb, varying the parameter values f_* (left) and M (right). Unless otherwise stated, we take parameter values $\gamma = 1$, $A = 1$, $C_* = 0.2$, $\rho = 0.25$, $K = 0.66$, $M = 1$, and $f_* = 0.3$ in case Ea, but $f_* = 1.5$ in case Eb.

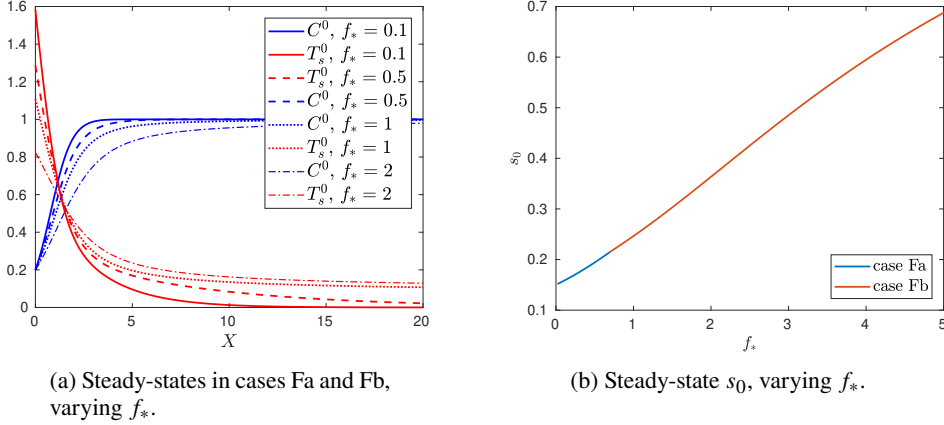


Figure 18: Steady-state numerical solutions of (10.10) for cases Fa and Fb, varying the parameter f_* . We take the other parameter values $\gamma = 1$, $A = 1$, $C_* = 0.2$, $\rho = 0.25$, $K = 0.66$.

numerical solutions of the full model (2.12) in steady state, using the same MATLAB solver `bvp4c`, having rescaled the spatial variable x in order to solve the system on a fixed domain. In this section, we compare the numerical solutions of (2.12) with the steady-state composite asymptotic solutions. Since we have restricted to steady-state solutions of the region-I model (except for the quasi-steady solutions for cases A and B), we only consider steady-state solutions in this section.

In figures 19 and 20 we compare the steady-state composite solution to the steady-state numerical solutions of the full model (2.12). For the numerical solutions of both the full model (2.12), and of the region-I problem as discussed in Section 10, we ensure the numerical error is two orders of magnitude smaller than δ , and so well below the expected error in the composite solutions. In the insets for each figure we show the same solutions but looking more closely at region I, which is too narrow to see clearly otherwise.

In all cases, we observe that the error in s_0 is larger than the width of the $O(\delta)$ region I, as expected. In particular, the error is $O(T^{\text{in}})$ in case A, $O(\eta)$ in cases B, C, and D, $O(T^{\text{in}})$ again in cases Ea and Fa, and $O(\theta_*^2)$ in cases Eb and Fb. In all cases, the maximal error is due to the switchback correction; in cases A–D, Ea and Fa this is the size of the small but non-zero temperature in region II, while in cases Eb and Fb this is the size of the error in C . Although the position of s_0 has error greater than $O(\delta)$, the function profiles in region I appear in all cases to have the correct shape.

We note that the leading-order problem (4.8) in regions AI and BI are identical, and that region I contains the majority of the variation in the solutions in these cases. In figure 19a with the convective heat transfer coefficient $\mu = 0$ we see very good agreement between the numerical and composite solutions, since the error is $O(T^{\text{in}})$ in this case. For case B, shown in figure 19b, there is a small $O(\mu) = O(\eta_B)$ amount of material consumption outside of region I, but this is not taken into account in our leading-order asymptotic structure. Thus in this case the leading-order solution s_0 is below the true value, since the material needs to be hotter in order for all the material consumption to take place in region BI.

For cases C and D, an $O(1)$ amount of material consumption occurs outside of region I. The steady-state position of the free boundary s therefore increases, since the temperatures in region I do not need to be so high, as less material consumption needs to happen in region I. This can also be understood in terms of an energy balance: since less heat is lost to the

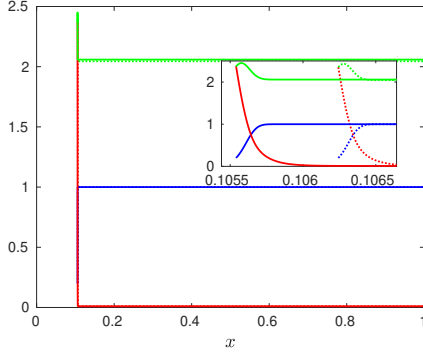
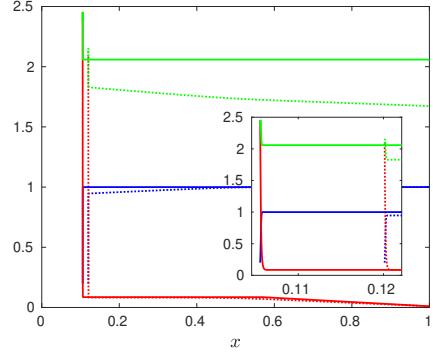
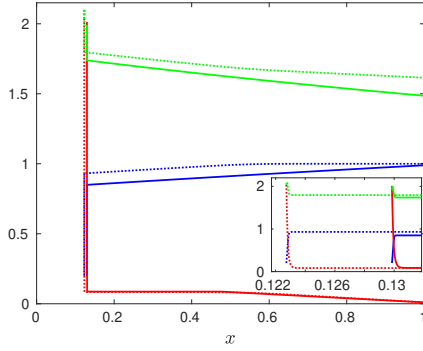
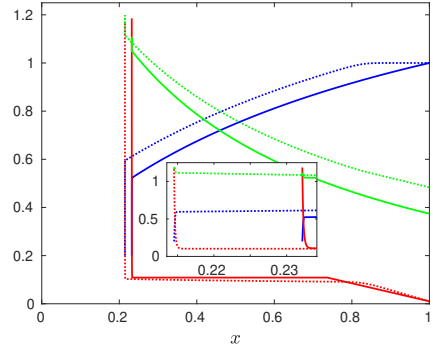
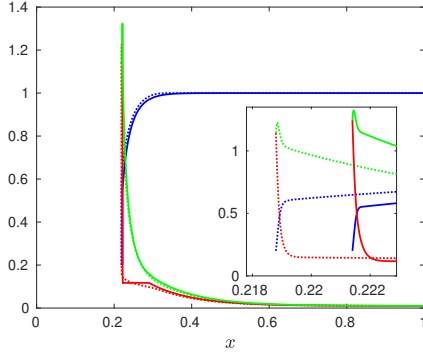
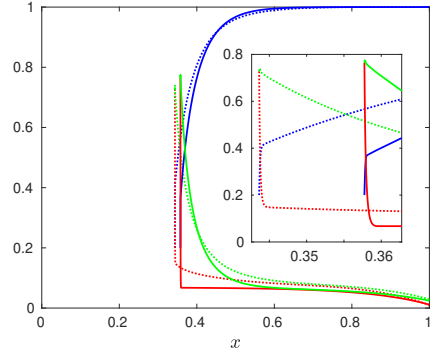
(a) Case A, $\mu = 0$.(b) Case B, $\mu = \eta_B = 0.09$.(c) Case C, $\mu = 0.1$.(d) Case C, $\mu = 1$.(e) Case Da, $\mu = 25$, $f_* = 0.3$.(f) Case Db, $\mu = 25$, $f_* = 1.2$.

Figure 19: Numerical steady-state solutions of (2.12) (dotted lines) and composite solutions as derived in Sections 4–7 (solid lines), with T_s red, T_g green, and C blue. The insets show the same solutions, near the free boundary $x = s$. In all cases we take $\delta = 10^{-4}$, $A = \gamma = 1$, $\rho = 0.25$, $K = 0.66$, $C_* = 0.2$, $T^{\text{in}} = 0.01$, and unless otherwise stated $f_* = 1$.

1711 system through hot gas flowing out through $x = 1$, the system needs less heating overall to
 1712 stay in steady state. Unlike in case B, the asymptotic composite solutions now account for
 1713 the material consumption outside of region I, and so the leading-order value s_0 is seen to be
 1714 within $O(\eta)$ of the true value in all cases. However, this value of s_0 is now an overestimate
 1715 for the true value of s (unlike in case B, where s_0 is below the true value of s). In case

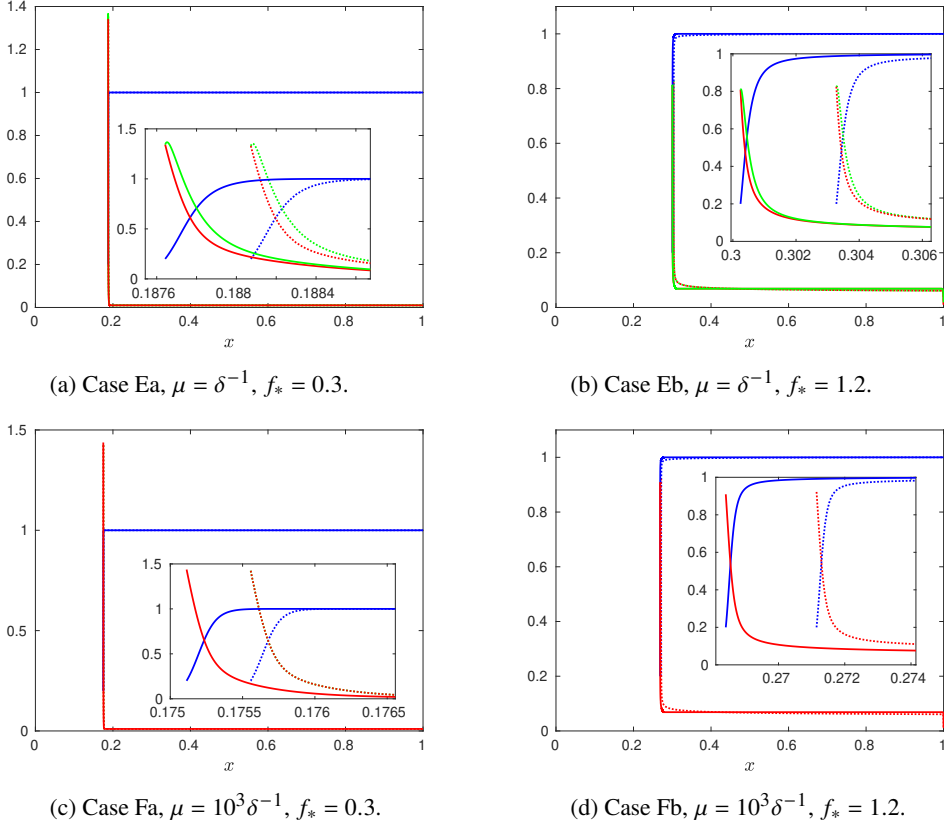


Figure 20: Numerical steady-state solutions of (2.12) (dotted lines) and composite solutions as derived in Sections 8–9 (solid lines), with T_s red, T_g green, and C blue. The insets show the same solutions, near the free boundary $x = s$. In all cases we take $\delta = 10^{-4}$, $A = \gamma = 1$, $\rho = 0.25$, $K = 0.66$, $C_* = 0.2$, and $T^{\text{in}} = 0.01$.

C this is because there is material consumption occurring throughout region CII, which is the entire domain up to $O(\eta)$. Since in reality no material consumption occurs within the $O(\eta)$ boundary layer CIV, the leading-order solution overestimates the amount of material consumption occurring in region CII, and thus overestimates s_0 . In addition, as the convective heat transfer coefficient μ becomes large, the leading-order gas temperature \hat{T}_g^0 in region CII is assumed to stay $O(1)$ throughout the domain. However, even for the relatively small $\mu = 1$, shown in figure 19d, by $x = 1$ we see T_g getting fairly small. As T_g gets close to T_s , the leading-order asymptotic solution overestimates the heat transferred from the gas to the solid, and thus overestimates the chemical reaction rate. In figure 19c, we take $\mu = 0.1 \approx \eta_B$, so that the numerical solution of the full model (2.12) is almost identical to that shown in figure 19b. The asymptotic composite solution using the structure of case C does a reasonable job of capturing the T_s profile as well as the T_g and C curves, despite the fact that the “boundary layer” CIV now fills the majority of the domain.

For Case D, all the thermal energy leaving region DI in the hot gas is used for chemical reactions in the outer domain (with a small error less than $O(\eta_D)$). Thus we see better agreement between the asymptotic composite solutions and numerical solutions of the full model than in case C, despite the error $O(\eta_D)$ being larger for case D than for case C. For cases E and F, the two temperatures are equal, or differ only in the $O(\delta)$ regions. We see

good agreement between the solution of the full problem (2.12) and our composite solutions in all cases shown in figure 20.

12. Discussion

In this paper we have formulated a model of counter-current flow modelling the flow of gas through a granular solid which allows for an endothermic chemical reaction at the gas-solid interface. We then used the method of matched asymptotic expansions to classify solution behaviors of this model to leading order in the limit of a large Péclet number δ^{-1} in the solid phase, and for a range of values of the convective heat transfer parameter μ . In particular, our analysis allows us to identify several vital distinguished limits, corresponding to the relative size of the parameters μ and δ , with different behaviours observed depending upon the distinguished limit the system is in.

Our asymptotic analyses reduce the computational complexity of the model, and give insight into the dominant physical mechanisms at play in different regions of the domain, for each distinguished limit. Some features of our analysis are common for all sizes of μ , such as the emergence of a natural temperature scaling at which the chemical reaction becomes important (η or θ_* , depending on both μ and δ), as well as a conduction boundary layer at the free boundary of the domain. Many of the solutions feature a region of the domain in which the solid temperature is almost uniform at the critical temperature; in the intermediate- μ cases B–D the heat transferred from the gas to solid in this region at temperature η is consumed entirely in the chemical reaction, while in the large- μ cases Eb and Fb there is a balance between the net heat advection and heat consumed in the reaction, at temperature θ_* .

In the case of small convective heat transfer rate (the small- μ regime), we observe that the flow of gas plays a limited role in the behaviour of solutions, with the dominant heating mechanism for the solid material due to the radiation incident on the free surface. On the other hand, for large values of the convective heat transfer coefficient μ , we found interesting counter-current driven behaviour, with the solution structures dependent upon the direction of net heat flux through the domain. For both small $\mu \leq O(\eta)$ and large $\mu \geq O(\delta^{-1})$, we found (at leading order) that all chemical reaction and material consumption occurs in a boundary layer (region I) of width $O(\delta)$ at the free boundary $x = s$, which is heated by the s -dependent solid surface temperature. For $O(1) \leq \mu \ll \delta^{-1}$, however, we found an $O(1)$ size material consumption in both region I and in (part of) the outer region of the domain.

For $\mu \leq O(\eta)$, the leading-order model is quasi-steady, and the leading-order steady-state solution in cases A and B was shown to be stable to perturbations within this quasi-steady limit. We constructed time-dependent solutions for cases A to C, but restricted our attention to the steady state in case D for sake of simplicity. For the large- μ limit comprising cases E and F, we discovered very different solution structures, depending on the direction of the flow of information, and discussed how these solution structures can vary in time. We expect similar time-varying structures in case D to those observed for cases E and F. For cases C–F, we have not investigated the stability of the steady-state solutions, since the structure of the region-I problem becomes more complicated in the time-dependent case, as the form of the boundary conditions varies in time. As a consequence, we can no longer compute numerical solutions of the region-I problem independently from the outer problem. However, since the steady-state solutions for cases C–F approach the respective steady-state solutions for cases A or B in the limit $\mu \rightarrow 0$, we expect that the steady-state solutions for cases C–F are also stable.

We have assumed throughout that the chemical reaction rate has Arrhenius dependence on the solid temperature T_s . This led to the logarithmic dependence of the critical solid temperature η on $\delta\mu$, in cases B to D, and the form of θ_* in cases Eb and Fb. It is natural

to wonder how our results might change if the dependence of the chemical reaction rate on temperature, Q , takes another functional form. Regardless of the form of the chemical reaction rate, in cases B to D we would still expect a dominant balance in the solid heat equation between the heat consumed in the chemical reaction and the heat transferred from the gas to the solid, in regions of the domain where T_s is small. Thus, while the form of the critical temperature η would depend on the functional form of Q , we might still expect similar solution structures, with regions of small, near-constant T_s , and the heat transferred from gas to solid used for the chemical reaction. Similarly, in cases E and F, we would still expect the vast majority of chemical reaction to occur in region I. However, the balance of advection and heat consumed by chemical reaction in cases Eb and Fb relied on the fact that the chemical reaction was exponentially small here. If the chemical reaction rate took a different form, we might observe different behaviour, such as the simple advection-dominated behaviour of cases Ea and Fa.

Our solutions show the important effect the endothermic reaction has on the counter-current system, with a much richer variety of behaviours observed than what is observed for non-reactive counter-current flows (Mitchell & Myers 1968). Our solutions in cases B–D capture the key features observed in simulations and experimental studies of various metallurgical processes (Agrawal & Ghoshdastidar 2017; Spang III 1972; Stadler *et al.* 2011). We have shown how the critical temperature, η , at which the chemical reaction becomes important depends on both the solid Péclet number and the heat transfer coefficient μ . We have also seen how the spatial extent of the reacting region with the solid at uniform temperature is different in the various distinguished limits, with the reaction occupying the whole domain at leading order in the optimal case C, an $O(1)$ region in case B, and a boundary layer about $x = s$ in case D. The variety of distinguished limits that we have found allow us to classify these different processes in terms of their expected behaviours. From measurements of industrial silicon-furnace temperatures (Johansen *et al.* 1998), the gas leaving a silicon furnace is likely to be significantly hotter than the solid material at the surface, but much cooler than the crater gases. From the solution structures we have found, the relevant regimes to the silicon furnace are therefore $\mu = O(\eta_B)$ and $\mu = O(1)$. Taking note of the simulated and experimental results in the work of Agrawal & Ghoshdastidar (2017), Spang III (1972), and Stadler *et al.* (2011), it seems likely that the metallurgical processes studied in these papers operate in the range $\eta \ll \mu \ll \delta^{-1}$ in order that, as one would expect, the chemical reactions are important through at least $O(1)$ regions of the domain.

Our analysis of this endothermic system is in contrast to the exothermic flame and combustion systems studied elsewhere in the literature. However, akin to the flame fronts commonly found in exothermic systems, we discovered a thin region of high temperature within which the majority of the chemical reaction occurs. However, unlike what is true for exothermic systems, our endothermic system requires an external heat source (in particular, the radiation boundary condition at $x = s$) to maintain the high temperatures necessary for reactions. For combustion, travelling-wave solutions are found, analogous to our quasi-steady-state solutions in which the solid reactant material flows into the reaction zone. However, in addition to this thin reaction zone, we have explored the structures in the outer region of the domain, essentially in the far-field of the reaction front. For exothermic flame fronts where an Arrhenius reaction rate is assumed, asymptotic treatments of the travelling-wave reaction fronts have encountered the difficulty that the chemical reaction rate is small but non-zero in the infinite domain ahead of the reaction front (where the temperature is cool but non-zero). The small but non-zero reaction occurring in the far-field of the flame front precludes these travelling-wave solutions. This is referred to as the *cold-boundary problem* by, for instance, Buckmaster & Ludford (1983). Our analysis in this paper (for endothermic reactions) is similar to how one might analyse the cooler regions outside of the reaction front

in the exothermic case, and so resolve the cold-boundary problem. In particular, one might view the slower processes outside the flame front as a switchback correction (Hinch 1991) to the leading-order travelling-wave behaviour.

Funding. This publication is based on work supported by the EPSRC Centre For Doctoral Training in Industrially Focused Mathematical Modelling (EP/L015803/1) in collaboration with Elkem ASA.

Declaration of Interests. The authors report no conflict of interest.

Data. In compliance with EPSRC's open access initiative, the data in this paper is available from <https://doi.org/10.5287/bodleian:gAa14qpBJ>

REFERENCES

- ABD, A.S., ELHAFYAN, E., SIDDIQUI, A.R., ALNOUSH, W., BLUNT, M.J. & ALYAFEI, N. 2019 A review of the phenomenon of counter-current spontaneous imbibition: Analysis and data interpretation. *Journal of Petroleum Science and Engineering* **180**, 456–470.
- AGRAWAL, A. & GHOSHDASTIDAR, P.S. 2017 Numerical simulation of heat transfer during production of rutile titanium dioxide in a rotary kiln. *International Journal of Heat and Mass Transfer* **106**, 263–279.
- ANDRESEN, B. 1995 Process model for carbothermic production of silicon metal. Master's thesis, NTH, Norway.
- BAER, M.R. & NUNZIATO, J.W. 1986 A two-phase mixture theory for the deflagration-to-detonation transition (DDT) in reactive granular materials. *International Journal of Multiphase Flow* **12** (6), 861–889.
- BEALS, R. 1981 Partial-range completeness and existence of solutions to two-way diffusion equations. *Journal of Mathematical Physics* **22** (5), 954–960.
- BILGER, R.W. 1989 Turbulent diffusion flames. *Annual Review of Fluid Mechanics* **21** (1), 101–135.
- BOOTY, M.R. & MATKOWSKY, B.J. 1991 Modes of burning in filtration combustion. *European Journal of Applied Mathematics* **2** (1), 17–41.
- BRENNEN, C.E. 2005 *Fundamentals of multiphase flow*. New York, NY: Cambridge University Press.
- BRUNNER, G. 2009 Counter-current separations. *The Journal of Supercritical Fluids* **47** (3), 574–582.
- BUCKMASTER, J.D. & LUDFORD, G.S.S. 1983 *Lectures on mathematical combustion*. Philadelphia, PA: SIAM.
- BYRNE, H. & NORBURY, J. 1994 Stable solutions for a catalytic converter. *SIAM Journal on Applied Mathematics* **54** (3), 789–813.
- BYRNE, H. & NORBURY, J. 1997 The effect of solid conversion on travelling combustion waves in porous media. *Journal of Engineering Mathematics* **32** (4), 321–342.
- CHAPIRO, G. & SENOS, L. 2018 Riemann solutions for counterflow combustion in light porous foam. *Computational and Applied Mathematics* **37** (2), 1721–1736.
- CHAPIRO, G. & DE SOUZA, A.J. 2016 Asymptotic approximation for counterflow combustion in porous media. *Applicable Analysis* **95** (1), 63–77.
- DEENDARLIANTO, HÖHNE, T., LUCAS, D. & VIEROW, K. 2012 Gas–liquid countercurrent two-phase flow in a PWR hot leg: A comprehensive research review. *Nuclear Engineering and Design* **243**, 214–233.
- EGERTON, A., GUGAN, K. & WEINBERG, F.J. 1963 The mechanism of smouldering in cigarettes. *Combustion and Flame* **7**, 63–78.
- FITT, V., OCKENDON, J.R. & SHILLOR, M. 1985 Counter-current mass transfer. *International Journal of Heat and Mass Transfer* **28** (4), 753–759.
- HAGAN, P.S. & OCKENDON, J.R. 1991 Half-range analysis of a counter-current separator. *Journal of Mathematical Analysis and Applications* **160** (2), 358–378.
- HINCH, E.J. 1991 *Perturbation Methods*. Cambridge: Cambridge University Press.
- IGNATOVA, S., HEWITSON, P., MATHEWS, B. & SUTHERLAND, I. 2011 Evaluation of dual flow counter-current chromatography and intermittent counter-current extraction. *Journal of Chromatography A* **1218** (36), 6102–6106.
- JOHANSEN, S.T., TVEIT, H., GRÅDAHL, S., VALDERHAUG, A.M. & BYBERG, J. 1998 Environmental aspects of ferro-silicon furnace operations - an investigation of waste gas dynamics. In *The 8th International Ferroalloys Congress, Pekin*.
- KAVIANY, M. 2012 *Principles of heat transfer in porous media*. New York, NY: Springer Science & Business Media.

- 1883 KIERZENKA, J. & SHAMPINE, L.F. 2001 A BVP solver based on residual control and the MATLAB PSE.
1884 *ACM Transactions on Mathematical Software* **27** (3), 299–316.
- 1885 KOOPMANS, R.J., SHRIMPTON, J.S., ROBERTS, G.T. & MUSKER, A.J. 2013 A one-dimensional multicomponent
1886 two-fluid model of a reacting packed bed including mass, momentum and energy interphase transfer.
1887 *International Journal of Multiphase Flow* **57**, 10–28.
- 1888 LUCKINS, E.K., OLIVER, J.M., PLEASE, C.P., SLOMAN, B.M. & VAN GORDER, R.A. 2021 Homogenised model
1889 for the electrical current distribution within a submerged arc furnace for silicon production. *European*
1890 *Journal of Applied Mathematics* pp. 1–36, <https://doi.org/10.1017/S0956792521000243>.
- 1891 MARIAS, F., ROUSTAN, H. & PICHAT, A. 2005 Modelling of a rotary kiln for the pyrolysis of aluminium
1892 waste. *Chemical Engineering Science* **60** (16), 4609–4622.
- 1893 MATLAB 2021 version 9.10.0 (R2021a). Natick, Massachusetts: The MathWorks Inc.
- 1894 MERZHANOV, A.G. & KHAIKIN, B.I. 1988 Theory of combustion waves in homogeneous media. *Progress in*
1895 *Energy and Combustion Science* **14** (1), 1–98.
- 1896 MITCHELL, J.W. & MYERS, G.E. 1968 An analytical model of the counter-current heat exchange phenomena.
1897 *Biophysical Journal* **8** (8), 897–911.
- 1898 MUJUMDAR, K.S. & RANADE, V.V. 2006 Simulation of rotary cement kilns using a one-dimensional model.
1899 *Chemical Engineering Research and Design* **84** (3), 165–177.
- 1900 NI, J. & BECKERMANN, C. 1991 A volume-averaged two-phase model for transport phenomena during
1901 solidification. *Metallurgical Transactions B* **22** (3), 349–361.
- 1902 NORBURY, J. & STUART, A.M. 1988 Travelling combustion waves in a porous medium. Part I—Existence.
1903 *SIAM Journal on Applied Mathematics* **48** (1), 155–169.
- 1904 NUNGE, R.J. & GILL, W.N. 1965 Analysis of heat or mass transfer in some countercurrent flows. *International*
1905 *Journal of Heat and Mass Transfer* **8** (6), 873–886.
- 1906 PLEASE, C.P., LIU, F. & McELWAIN, D.L.S. 2003 Combustion waves with exothermic/endothermic reactions.
1907 *Combustion Theory and Modelling* **7**, 129–143.
- 1908 RAVIKRISHNA, R.V. & SAHU, A.B. 2018 Advances in understanding combustion phenomena using non-
1909 premixed and partially premixed counterflow flames: A review. *International Journal of Spray and*
1910 *Combustion Dynamics* **10** (1), 38–71.
- 1911 SCHEI, A., TUSET, J.K. & TVEIT, H. 1998 *Production of High Silicon Alloys*. Trondheim, Norway: Tapir.
- 1912 SCHMIDT-NIELSEN, K., HAINSWORTH, F.R. & MURRISH, D.E. 1970 Counter-current heat exchange in the
1913 respiratory passages: effect on water and heat balance. *Respiration Physiology* **9** (2), 263–276.
- 1914 SCHULT, D.A., BAYLISS, A. & MATKOWSKY, B.J. 1998 Traveling waves in natural counterflow filtration
1915 combustion and their stability. *SIAM Journal on Applied Mathematics* **58** (3), 806–852.
- 1916 SIRIGNANO, W.A. 2021 Mixing and combustion in a laminar shear layer with imposed counterflow. *Journal*
1917 *of Fluid Mechanics* **908**, A35.
- 1918 SKALICKA-WOŹNIAK, K. & GARRARD, I. 2014 Counter-current chromatography for the separation of
1919 terpenoids: a comprehensive review with respect to the solvent systems employed. *Phytochemistry*
1920 *Reviews* **13** (2), 547–572.
- 1921 SLOMAN, B.M., PLEASE, C.P. & VAN GORDER, R.A. 2018 Asymptotic analysis of a silicon furnace model.
1922 *SIAM Journal on Applied Mathematics* **78** (2), 1174–1205.
- 1923 SLOMAN, B.M., PLEASE, C.P. & VAN GORDER, R.A. 2020 Melting and dripping of a heated material with
1924 temperature-dependent viscosity in a thin vertical tube. *Journal of Fluid Mechanics* **905**, A16.
- 1925 SPANG III, H.A. 1972 A dynamic model of a cement kiln. *Automatica* **8** (3), 309–323.
- 1926 STADLER, K.S., POLAND, J. & GALLESTEY, E. 2011 Model predictive control of a rotary cement kiln. *Control*
1927 *Engineering Practice* **19** (1), 1–9.
- 1928 SUTHERLAND, I.A. 2007 Recent progress on the industrial scale-up of counter-current chromatography.
1929 *Journal of Chromatography A* **1151** (1–2), 6–13.
- 1930 TIESZEN, S.R. 2001 On the fluid mechanics of fires. *Annual Review of Fluid Mechanics* **33** (1), 67–92.
- 1931 WINTERS, R.W. & DAVIES, R.E. 1961 The role of countercurrent mechanisms in urine concentration: a
1932 review. *Annals of Internal Medicine* **54** (4), 810–826.